# Phase Separation of a Nodulin Sec14-like protein Maintains Auxin Efflux Carrier Polarity at *Arabidopsis* Plasma Membranes

Chen Liu[1,2,3], Andriani Mentzelopoulou[2,3], Alexandra Deli[2,3], Fotini Papagavriil[2,3], Prashanth Ramachandran[4], Artemis Perraki[2,3], Lucas Claus[5,6], Sebastian Barg[7], Peter Dörmann[8], Yvon Jaillais[9], Philipp Johnen[10], Eugenia Russinova[5,6], Electra Gizeli[2,3], Gabriel Schaaf[10], Panagiotis Nikolaou Moschou[1,2,3]*

[1]Department of Plant Biology, Uppsala BioCenter, Swedish University of Agricultural Sciences and Linnean Center for Plant Biology, Uppsala, Sweden

[2]Department of Biology, University of Crete, Heraklion, Greece

[3]Institute of Molecular Biology and Biotechnology, Foundation for Research and Technology-Hellas, Heraklion, Greece

[4]Department of Organismal Biology, Physiological Botany, Linnean Centre for Plant Biology, Uppsala University, Ulls v. 24E, SE-756 51, Uppsala, Sweden

[5]Department of Plant Biotechnology and Bioinformatics, Ghent University, 9052 Ghent, Belgium

[6]Center for Plant Systems Biology, VIB, 9052 Ghent, Belgium

[7]Department of Medical Cell Biology, Uppsala University, Ulls v. 24E, SE-756 51, Uppsala, Sweden

[8]Institute of Molecular Physiology and Biotechnology of Plants, University of Bonn, Bonn, Germany

[9]Laboratoire Reproduction et Développement des Plantes, Univ Lyon, ENS de Lyon, Université Claude Bernard Lyon 1, CNRS, INRAE, F-69342, Lyon, France

[10]Department of Plant Nutrition, Institute of Crop Science and Resource Conservation, University of Bonn, Bonn, Germany

*Corresponding Author and Lead Contact:

Panagiotis.moschou@imbb.forth.gr

**KEYWORDS**

Proteolysis, Microtubules, Biomolecular condensates, Phase separation, Developmental patterning, Plasma membrane pattern, Separase, Kinesins, Cytoskeleton, Vesicle trafficking, Cell Polarity, Caspases

**Abstract**

Robust development can be modulated by local protein accumulation which is sometimes manifested as polarity patterns; yet, the mechanisms that lead to these patterns are largely unknown. Using the model plant Arabidopsis, we report that auxin-induced polar patterns can be reinforced by the phase transition of a SEC14-like lipid-binding protein at the plasma membrane. Using imaging, genetics, and *in vitro* reconstitutions, we show that the SEC14-like phase transition is promoted outside the stem cell root niche through its association with the caspase-like protease separase and conserved microtubule motors in a plasma membrane interface. Separase cleaves SEC14-like to promote its transition from liquid-like clusters to solid-like filaments. Filaments self-amplify and potentiate the robustness and maintenance of plasma membrane domains through associations with polar proteins. This work uncovers that robust cell patterns involve proteolysis-mediated phase transitions at unpreceded plasma membrane interfaces.

**Synopsis**

This study provides an example of a protein that undergoes liquid-like phase separation at the plasma membrane in plants. Importantly, this protein known as SFH8 is a lipid-like transferase and can undergo proteolytic-induced solidification, which is an important event in the maintenance of polarized delivery of PINFORMED proteins.

- The complex comprising of the conserved caspase-like protease separase and the kinesin Kin7.3 (known as "KISC") associates with a SEC14-like homolog, the SFH8 protein at apicobasal polar domains
- Separase cleaves SFH8 to yield a carboxy-terminal proteoform that undergoes a liquid-to-solid transition producing filamentous assemblies at the plasma membrane
- The KISC/SFH8 constitutes a feedback loop with auxin that potentiates the interaction, fusion, and maintenance of proteins with polar domains

1    **INTRODUCTION**

2    The few known polar proteins in plants provide crucial information for robust development

3    (Houbaert et al., 2018; Marhava et al., 2019; Platre et al., 2018). Polar protein accumulation may

4    depend on diffusible signals such as that of the hormone auxin. At high auxin levels, for example,

5    the crowding of negatively charged lipids dictates plasma membrane localisations of signaling

6    proteins (Platre et al., 2018). In turn, the polar efflux auxin carriers PINFORMED (PINs) can

7    regulate auxin levels. For example, PIN2 in the root localizes at apical or basal plasma membrane

8    (PM) domains and is required for the formation of the auxin concentration gradient (Friml et al.,

9    2004). Auxin is then perceived by cells in a concentration-dependent manner as a permissive or

10   restrictive signal (Marhava et al., 2019). Auxin signaling can be modulated by the nucleo-

11   cytoplasmic partitioning of the prion-like transcription factors known as AUXIN RESPONSE

12   FACTOR (ARF). During development, ARF7 and ARF19 undergo condensation in the cytoplasm

13   which blocks their entry into the nucleus, thereby attenuating auxin signaling (Powers et al., 2019).

14          In Arabidopsis, the caspase-like protease separase (*extra spindle poles*, "ESP") interacts

15   with three centromeric protein-E-like Kinesin 7 (Kin7) homologs, the so-called "Kin7.3-clade"

16   (Kin7.1, Kin7.2, and Kin7.3). This complex (the kinesin-separase complex, "KISC") is recruited on

17   microtubules (MTs), and the most abundant protein of the complex is Kin7.3 (Moschou et al.,

18   2016). ESP is an evolutionarily conserved protein responsible for sister chromatid separation and

19   membrane fusion in both plants and animals (Bembenek et al., 2010; Liu et al., 2020). ESP binds

20   the Kin7 C-termini, inducing conformational changes that expose the MT-avid N-terminal "motor

21   domain" of the Kin-7, thereby increasing KISC binding atop MTs. KISC modulates PIN2 delivery

22   to the plasma membrane (PM). This is supported by the finding that the temperature-sensitive

23   *radially swollen 4* (*rsw4*) mutant harboring a temperature-sensitive ESP variant or the Kin7.3-

24   clade mutants have compromised PIN2 delivery and polarity at the PM (Moschou et al., 2016).

25   Yet how KISC acts upon PM polar domains remains elusive.

26          Here we discover that KISC is recruited to the PM through the hitherto uncharacterized

27   SEC14-like lipid transfer protein SFH8. Under the premise that the KISC interacted with SFH8,

28   we examined the biological consequences of this interaction. ESP trimmed SFH8 protein that led

29   to the conversion of SFH8 from a liquid to a more rigid filamentous phase at the PM. This transition

30   is associated with SFH8 polarization and interaction with PIN2. Auxin promoted SFH8 clustering,

31   and liquidity, halting SFH8 cleavage by KISC. Remarkably, our study shows how spatiotemporally

32   confined proteolysis can lead to changes in the material properties of proteins and how these

33   properties can be translated to developmental outcomes.

**RESULTS**

*KISC Associates with the Lipid-transfer protein SFH8 at the Plasma Membrane*

As KISC regulates PIN2 at the PM, we aimed at surveying potential associations between the KISC and the PM. We found that fluorescently-tagged or native ESP/Kin7.3 proteins decorated PM; in the distal meristem (as defined below) both proteins decorated basal domains in the cortex and apical domains in the epidermis (**Figure S1A-F**). As KISC proteins lack lipid-binding motifs, we postulated that KISC associates with the PM via a protein tether. To identify this tether we screened a yeast two-hybrid (Y2H) library against Kin7.3. Among the five proteins identified, we followed At2G21520, as it localized at the PM in *Nicotiana benthamiana* (**Figure S1G**; **Supplemental Info**). At2G21520 is a SEC14-like protein (BLAST: p= 1e$^{-49}$), with a C-terminal "nodulin" positively-charged patch and ascribed symbol "SFH8" (**Figure S1H; File S1**) (Vincent et al., 2005). In Y2H, although both SFH8 termini bound Kin7.3 C-terminal tail (but not the N-terminal motor domain), the SFH8 C-terminus was more avid (**Figure S1I**). We confirmed the Kin7.3-SFH8 interaction by co-immunoprecipitations or glutathione S-transferase (GST) pull-down assays (**Figure 1A-C** and **S1K** for protein purifications). Furthermore, through ratiometric bi-fluorescence complementation (rBiFc) in Arabidopsis root protoplasts, we showed that SFH8/Kin7.3 associate mainly at the PM (**Figure 1D;** see also **Figure S6D**).

In budding yeast, Sec14p localizes at the *trans*-Golgi network (TGN) where it promotes vesicle formation presumably by stimulating phosphatidylinositol-4-phosphate (PI4P) synthesis (Schaaf et al., 2008). SFH8 rescued the temperature-sensitive budding yeast *sec14-1* mutant suggesting that SFH8 is a genuine Sec14-like protein (**Figure S1J**). SFH8 showed broad phosphatidylinositol (PI) and unexpected phosphatidylserine (PS) binding (**Figure 1E**), unlike other Sec14-like proteins which cannot bind PS (Hertle et al., 2020; Sugiura et al., 2019).

Localization and functions of SFH proteins are largely unknown, while genetic evidence suggests that SFH1 is essential for root hair development (Vincent et al., 2005). We expressed SFH8-mNeon under its native promoter (pSFH8) to address SFH8 localization in 4 developmental root regions: core meristem (1; stem cell niche), meristematic zone (2; "proximal meristem"), meristematic/transition zone (3), and late transition zone ("distal meristem"; **Figure 1F**) (4). SFH8-mNeon showed signals in all root cells at the PM, decorating apical PM domains in the epidermis and basal domains in the cortex/vasculature in distal meristem cells (**Figure 1G**). SFH8 associated with the cell plate but was excluded from the leading edge, much like the KISC proteins (Moschou et al., 2016; Moschou et al., 2013); SFH8 colocalized at the PM with Kin7.3 in filamentous-like patches, and colocalization increased during development (**Figure 1H**, and below). Furthermore, SFH8 and KISC proteins attained polarity at regions 3-4 (**Figures 1G, I, J,**

2

68  **S1E,** and below). The KISC co-localization/interactions with SFH8 prompted us to examine
69  possible biological consequences of this interaction.

70  ### *SFH8 recruits KISC at the PM*

71  Next, we examined a putative mutual targeting potentiation of SFH8/KISC at the PM. We thus
72  isolated two T (transfer)-DNA insertions in SFH8, the *sfh8-1,* and *sfh8-2*; RNAseq showed that
73  *sfh8-1* harbored a truncated *sfh8* mRNA (**Figure 2A**). Both mutants had defects in root growth
74  ((**Figures 2A**) and gravitropism **(Figure S2A)** at early stages implying compromised auxin-
75  signaling, with a shorter stature, decreased branching, smaller cotyledons, and leaves, **Figure**
76  **S2B**). At the seedling stage, the *sfh8* phenotypes resembled those of the KISC mutants (i.e. *rsw4*
77  and the partial loss-of-function Kin7.3-clade mutant *kin7.1kin7.3kin7.5 ("K135"*); with the readouts
78  used *sfh8* phenotypes were evident 3 days post-germination (**Figure 2B-D**). We did not observe
79  additive phenotypes at early developmental stages in KISC/SFH8 mutant combinations, implying
80  some functional convergence between KISC/SFH8 (**Figure 2B**). Yet, *sfh8-1* had reduced silique
81  length and a more severe adult phenotype than the one reported for the KISC mutants (**Figure**
82  **S2A-C**). Due to the phenotypic similarity between *sfh8-1* and *-2*, we carried out further analyses
83  with *sfh8-1* (hereafter *"sfh8"*).

84  We ascertained the link between *sfh8* phenotype with SFH8, as various N- and C-
85  terminally SFH8 fusions (with various tags or fluorophores; showing similar localizations, see
86  below) driven by several promoters (pSFH8, pKin7.3, and the meristematic pRPS5a; **Figures 2A-**
87  **E, S2A, B, D, E, F**) could efficiently complement *sfh8*. In *sfh8*, the apical meristem was reduced
88  (~2-fold) showing lower mitotic activity (defined by "Cell Cycle Tracking" (Yin et al., 2014) and
89  occasionally perturbed cell division planes (**Figure 2F, S2D**). Although SFH8 is a Sec14-like
90  protein its deletion (or of KISC) did not affect lipid levels (**Figure S2E, File S4**), suggesting that
91  the observed phenotypes did not relate to perturbations in lipid homeostasis.

92  When expressed in the *sfh8* background, GFP-Kin7.3 showed both reduced PM
93  localization and polarity (**Figure 2G**). While SFH8-mNeon tethering at the PM did not substantially
94  depend on KISC, SFH8-mNeon in the corresponding mutants had reduced polarity (**Figure 2H**).
95  We corroborated these results through transient KISC depletion through Kin7.3 C-terminal "tail"
96  overexpression (*pXVE>pKin7.3>HA-Kin7.3tail*). This inducible Kin7.3 tail overaccumulation
97  disrupts KISC, as it titrates ESP out of the active complex (Moschou et al., 2016). Consistently,
98  Kin7.3 tail accumulation but not the full-length led to SFH8 polarity loss (**Figure 2I**). Hence,
99  KISC/SFH8 synergistically define their localization: SFH8 tethers KISC at the PM, and in turn,
100 KISC promotes SFH8 polarization.

3

### *SFH8 Forms PM Liquid-like Clusters that Restrict Association with KISC*

As KISC binds on MTs, we postulated that SFH8/KISC interact atop MT filaments next to the PM. Contrary to our expectations, the standard MT marker MAP4$^{MBD}$ (or $\beta$-tubulin) showed very partial colocalization with Kin7.3 at the PM, while amiprophos-methyl (APM) that disassembles MTs (10 nM; Moschou et al., 2016) did not alter PM localization of Kin7.3 (**Figure S3A, C**). We observed that KISC/SFH8 decorated the same filaments in *N. benthamiana*, while KISC proteins were excluded from SFH8-positive clusters structures at the PM (**Figure S3B**). In Arabidopsis roots, SFH8 filaments were short (<0.5 µm) and insensitive to APM (**Figure S3C**). Likewise, ESP and SFH8 decorated similar filaments (**Figure S3D;** root region 3). Hence, KISC/SFH8 co-assemble in MT-independent filaments.

We further followed KISC/SFH8 localization in Arabidopsis roots by total internal reflection fluorescence (TIRF)-Microscopy. TIRFM excels at looking at cell surface processes due to the shallow illumination penetration (decay constant ~100 nm), offering a high signal-to-noise ratio. We focused on lateral cell junction domains (**Figure 3A**; regions 3-4; 3 days post-germination). Our analysis showed that SFH8-mNeon segregated into two major populations: (i) immobile filaments that co-localized with Kin7.3-tagRFP (see **Figure S1F** for fusion functionality), and (ii) mobile or immobile Kin7.3-tagRFP-independent clusters (**Figure 3B**). The mobile SFH8 clusters showed restricted lateral diffusion at the PM and occasionally fused, properties reminiscent of cellular "biomolecular condensates" that sometimes form through a process known as liquid-liquid-phase separation (LLPS) (**Movies S1-3, Figure 3C, D**). Under certain conditions, proteins or other molecules can demix from the bulk phase through LLPS, thereby retaining liquid-like properties such as surface tension leading to high circularity akin to droplets (Milovanovic et al., 2018). We also observed some non-diffusing less droplet-like small clusters (**Movies S2, 3**), that could represent intermediate phases between the cluster-state (droplet-like) and the filamentous state.

Kin7.3/SFH8 interacted prominently in short filaments but not in SFH8 clusters, which showed high or low dwelling times at the PM (**Figure 3E**). The lack of KISC-SFH8 association in clusters in which SFH8 presumably should show increased avidity for KISC due to the increased concentration of SFH8 was counterintuitive. We thus set out to determine why KISC was excluded from the SFH8 clusters. We assumed that reducing the repulsion of the polybasic charge of nodulin could promote the clustered state of SFH8, further increasing the concentration of the protein. In support of our assumption, charge attenuation by mutations of the six pertinent lysines (K) to alanine (A) in the nodulin artificially increased SFH8 clustering at the PM in *N. benthamiana*, while a mutation in two K exerted a moderate effect (**Figure S3E**). In good agreement, Kin7.3

4

135    interacted and colocalized with the WT variant but not with SFH8[6KtoA] (**Figure S3F**). In
136    Arabidopsis, mNeon-*SFH8*[6KtoA] showed a lack of PM polarity and filaments (**Figure S3G, H**). This
137    result implied that hindering interaction with KISC by reducing the accessibility of the C-terminus
138    which is the preferred interaction interface with KISC, completely blocked SFH8 polarization.

139        To better understand the dynamics of SFH8 at the PM, we used fluorescence recovery
140    after photobleaching (FRAP). We assumed that SFH8 clusters have increased liquidity and
141    reduced stability at the PM, compared to filaments, as they showed features of LLPS which could
142    imply a rapid exchange of SFH8 molecules with the cytoplasm. Although FRAP is not a decisive
143    feature for testing LLPS, liquid-like clusters can display rapid internal reorganization and a
144    corresponding rapid fluorescent recovery on the order of seconds, whereas more solid-like
145    condensates such as non-dynamic filaments may show little recovery (Gutierrez-Beltran et al.,
146    2015). FRAP showed that SFH8-mNeon was highly dynamic at the PM close to the meristem,
147    unlike the distal meristem in which SFH8 lacked dynamicity (**Figure 3G**). Using super-resolution
148    dynamic imaging, we observed that at stages at which KISC showed little colocalization with
149    SFH8, SFH8 was in the clustered state while later was converted to filaments (e.g. region 2 to 4;
150    **Figure 3G**). As the shift in SFH8 FRAP rate associated well with the cluster-to-filament transition,
151    this suggested a role for KISC in this transition. In accordance, filamentous formation of SFH8-
152    mNeon was significantly reduced in the KISC mutants (**Figure 3H**; >3-fold). Altogether, these
153    findings suggest that condensed clusters of SFH8 abolish KISC-SFH8 interactions, but later
154    during development KISC mediates the conversion of SFH8 clusters to solid-like filaments.

155    ***KISC Trimming of SFH8 Promotes the Cluster-to-Filamentous Transition***

156    The SFH8 filamentous transition dependency on KISC prompted us to examine the underlying
157    mechanism. We postulated that KISC may promote structural changes on SFH8 that enable the
158    filamentous transition. Interestingly, western blots from lines expressing pRPS5a-driven SFH8
159    with a hexahistidine-triple-flag (referred to as "HF")-mScarlet tag at the C or N terminus (~106
160    kDa; complementation in **Figure S1F**) showed a decreased abundance of tagged-SFH8 with age
161    (3-7 days) and increased SFH8 full-length abundance in *K135* or *rsw4* (**Figure 4A**). We also
162    observed a presumptive ~40 kDa (or ~10 kDa excluding mScarlet) N-terminal cleavage product
163    in WT, which was almost absent in *K135* or *rsw4* (**Figure 4A**). We confirmed that SFH8 is cleaved
164    using N- and C-terminally HF-tagged SFH8 lines (**Figure 4A**; right panel). We also observed that
165    pSFH8:mNeon-SFH8 lines had fluorescent cytoplasmic puncta that accumulated gradually during
166    development, which were absent from pSFH8:SFH8-mNeon lines (**Figure 4B**). This result
167    suggested that cleaved SFH8 N-termini coalesce in puncta, and implied a link between KISC-

5

168    SFH8 interaction and their formation. Puncta were also observed in lines expressing SFH8 cDNA

169    (complementing *sfh8*, **Figure S2F**)*,* confirming that SFH8 fragments are produced by cleavage

170    and not transcriptional mechanisms (e.g. splicing).

171        To ascertain the association between SFH8 puncta and KISC, we established lines

172    expressing an N/C-tagged fluorescent SFH8 (hereafter "cleavage biosensor"; pRPS5a:mScarlet-

173    SFH8-mNeon). We assumed that if SFH8 was cleaved *in vivo* then signals of mNeon and

174    mScarlet would not colocalize. In good agreement, we observed a lack of signal colinearity

175    between mNeon and mScarlet in distal meristem regions but not earlier (region 3), coinciding with

176    KISC-SFH8 interaction (**Figure 4C**). Furthermore, SFH8 clusters showed both mNeon/mScarlet

177    signals, unlike the filaments which were only decorated by mNeon, suggesting that filaments

178    represent a cleaved SFH8 form (**Figure 4C**). This developmentally "late cleavage" is consistent

179    with the increment of cleavage with the plant age (**Figure 4A-D**), as 3 days after germination the

180    root core meristem (region 1; around QC, see also Figure 1F) in which SFH8 is uncleaved, would

181    comprise a large proportion of the root.

182        But why does the cleaved fragment of SFH8 form cellular puncta? To answer this question,

183    we aimed first at identifying the structure of this fragment, and to do that with high precision we

184    had to define the exact position at which cleavage takes place. We thus immunoprecipitated

185    SFH8-mScarlet-HF and performed SFH8 proteomic peptide coverage abundance. Our results

186    indicated a potential cleavage site right after the arginine $R^{84}$, which coincided with the reported

187    in non-plants ESP cleavage φEXXR consensus sequence $I^{80}EDVR^{84}D$ (Hellmuth and Stemmann,

188    2020; Liu et al., 2017) which is also conserved in other SFH8-like proteins (**Figure 4D, E, File**

189    **S3**). We further established an *in vitro* ESP cleavage assay in which we confirmed that

190    immunopurified ESP, mitotically activated through co-expression with cyclinD (Xu et al., 2020),

191    could cleave recombinant GST-SFH8 at $R^{84}$; we confirmed the specificity of our assay by showing

192    the cleavage of the well-known target of ESP in non-plants, the cohesin (**Figure S4A-D**) (Minina

193    et al., 2017).

194        To define the structure of the 1-84 aa SFH8 N-terminal fragment, we turned to *in silico*

195    predictions and found that it is intrinsically disordered (IDR; hereafter "SFH8$^{IDR}$"; **Figure 4F**),

196    suggesting that is unlikely to be defined by persistent secondary and/or tertiary structures. This

197    architecture is conserved throughout evolution for SFH-like proteins (**File S3**). Furthermore,

198    deletion of this IDR region led to significant polarity loss of SFH8, lack of developmental

199    robustness, and reduced *sfh8* complementation (**Figure S4E**), suggesting that the controlled

200    removal of the IDR is important for development.

201     As IDRs are enriched in proteins undergoing LLPS (Banani et al., 2017), we tested
202     whether SFH8[IDR] is associated with the liquid-like features of SFH8 at the PM. SFH8[IDR] was
203     predicted through catGranule as an inducer of LLPS, while for the corresponding region of a close
204     SFH8 homolog, the SFH6 (SFH6[IDR]) catGranule predicted reduced propensity to undergo LLPS
205     (**Figure 4F**). We further observed that during imaging, "SFH8[IDR]" puncta lacked colocalization with
206     vesicular markers (**Figure S4F, G**), and showed LLPS hallmarks such as dynamic morphology
207     with frequent splitting, fusion, and interconnections (**Movie S4, Figure S4H**). FRAP of mNeon-
208     tagged SFH8[IDR] puncta showed a rapid signal recovery ($t_{1/2}$~10 s, mobile fraction 40%) and
209     sensitivity to 1,6-hexanediol which may block LLPS (**Figure S4H, I**) (Cuevas-Velazquez et al.,
210     2021; Kroschwald et al., 2017); 1,6-hexanediol led also to the dissolution of SFH8 clusters on the
211     PM but not of filaments (**Figure S4I**).

212     Since SFH8 clusters showed droplet-like morphology, sensitivity to 1,6-hexanediol, rapid
213     FRAP implying liquidity, and fused akin to cellular condensates (**Figure 3D**), we assumed that
214     SFH8 clusters may form by LLPS. *In silico* prediction using the algorithms, PLAAC and CIDER
215     showed that SFH8 lack prion-like domains, but can adopt context-specific conformational states
216     with an absolute value of net charge per residue of 0.014 (NPCR, "Janus" conformer). This result
217     suggests that SFH8 propensity to LLPS may be sensitized by microenvironments and that SFH8
218     may be represented by an ensemble of conformers. The highly electronegative field of the PM
219     where SFH8 accumulates could lead to (un)balancing of opposite charges upon IDR removal
220     (IDR NCPR=0.071), and structural expansion due to repulsive forces, which could explain the
221     filamentous transition.

222     LLPS of SFH8 relied on the N-terminal IDR, as swapping of SFH8 IDR with that of SFH6
223     reduced clustering at the PM and puncta formation in the presence of ESP (**Figure 4G-I**). SFH8[IDR]
224     sequence composition is distinct to known prion-like proteins that undergo phase transitions in
225     the cytoplasm but shows similar amino acid distribution to the average IDR profile for Arabidopsis
226     (**Figure 4J**; (Powers et al., 2019). CIDER predicts SFH8[IDR] as a strong polyampholyte and thus
227     may act as an "entropic bristle" through random movements around its attachment point and
228     exclude the contact with other proteins, reducing the probability also of SFH8 to undergo
229     expansion and filamentous transition. Overall, our analyses suggest that SFH8 behaves like a
230     polyampholyte undergoing LLPS at the PM with the negatively charged lipids (e.g. PI) likely
231     buffering repulsive charges.

232     To experimentally determine some of the SFH8 LLPS properties, we established an *in*
233     *vitro* LLPS assay with fluorescently labeled proteins. Under phase separation conditions (see
234     **STAR METHODS**), SFH8 or the uncleavable variant SFH8[R84A] rapidly formed condensates at

235    relatively high concentrations (5 µM), with a propensity for fusion, while SFH8$^{\Delta IDR}$ formed filament-

236    like assemblies or aggregates as expected (**Figure S4J**). Interestingly, in the presence of

237    SFH8$^{\Delta IDR}$, SFH8 could also form filamentous structures suggesting that the filamentous

238    conversion of only a few SFH8 molecules can transduce this conformation to non-filamentous

239    SFH8. We thus speculate that cleavage of only a few SFH8 molecules by the low amounts of

240    ESP in a cell can be sufficient in the initial stages of SFH8 filamentous development. In full

241    consistency with the *in vivo* data, the *in vitro* filaments did not recover in FRAP experiments and

242    showed reduced circularity compared to SFH8 condensates (**Figure S4J**).

243    One point of criticism in our LLPS assays could be their physiological relevance, as we

244    tested LLPS in a bulk phase at which SFH8 could freely diffuse and explore a 3D space. We thus

245    established a system to test whether SFH8 can phase-separate atop model membranes. To this

246    end, we used SUPER templates (supported lipid bilayers with excess membrane reservoir) that

247    contain low-tension membranes surrounding a glass bead (Pucadyil and Schmid, 2010). We

248    showed that GST-SFH8 could form large circular clusters atop SUPER templates rich in PI lipids

249    (**Figure S4K**). Surprisingly, atop SUPER templates, SFH8 could show LLPS at low concentrations

250    (0.1 µM) than without SUPER templates (≥5 µM) suggesting that membrane attachment of SFH8

251    can promote its LLPS (**Figure S4K**). On the contrary, GST-tagged SFH8$^{\Delta IDR}$ did not show similar

252    behavior and was oligomerized in native gels (**Figure S4L**). Furthermore, electron negative

253    staining microscopy confirmed that SFH8$^{\Delta IDR}$ formed solid filaments (~400 nm) *in vitro,* unlike the

254    full-length SFH8 (**Figure S4M**). Hence, PIs may neutralize electrostatic repulsions via counterion-

255    mediated charge neutralization along SFH8, as suggested for other proteins (Pak et al., 2016),

256    thereby mediating LLPS and acting as multivalent scaffolds. Noteworthy, in 2D systems (e.g. PM),

257    the threshold concentration for LLPS can be an order of magnitude lower than in 3D (Banjade

258    and Rosen, 2014). We further speculate that the released N-terminal SFH8$^{IDR}$ retains features of

259    the LLPS SFH8 state even after its cleavage, implying a "structural memory" for condensates.

260    Next, we queried the biological importance of SFH8$^{IDR}$ removal. In lines expressing the

261    uncleavable variant pRPS5a:mNeon-SFH8$^{84RtoA}$ in *sfh8* background, cells lacked the cytoplasmic

262    fluorescent puncta, while SFH8$^{84RtoA}$ was apolar much like SFH8 in KISC mutants, and did not

263    convert to filaments (**Figure 4K-M**). As expected, pSFH8:mNeon-SFH8 showed higher FRAP

264    rates on the PM (due to cleavage and liquidity of clusters), unlike the corresponding C-terminally

265    tagged SFH8-mNeon; in WT mNeon-SFH8 showed higher diffusion as determined by FRAP on

266    the PM consistent with the increased cleavage and release from the PM (**Figure S4N**). Altogether,

267    these results suggest that, SFH8 clusters show LLPS properties and that upon cleavage SFH8

268    (initially in LLPS) released two proteolytic proteoforms, the C-terminal SFH8$^{\Delta IDR}$ (converted to

8

269     solid-like filaments) and the N-terminal SFH8$^{IDR}$ (cytoplasmic puncta). These transitions of SFH8

270     are important, as the uncleavable variant of SFH8 (or the non-accessible SFH8$^{84RtoA}$) did not

271     rescue the *sfh8* mutant.

### Conversion to SFH8 Filaments Promotes Fusion of Vesicles with the PM

273     Next, we aimed at further deciphering the biological significance of SFH8 phase transitions.

274     Longitudinal sections in Transmission Electron Microscopy (TEM) of *rsw4K135*, and *sfh8* root

275     region 3 revealed significantly more vesicles compared to WT that although were efficiently

276     tethered at the PM remained unfused (**Figure S5A, B**). To substantiate the previous, we followed

277     PIN2 dynamic delivery at PM polar domains in the corresponding mutants. We chose PIN2 as

278     KISC and SFH8 mutants showed phenotypic similarities at early developmental stages, and KISC

279     plays a role in PIN2 delivery (Moschou et al., 2016). Accordingly, we observed that the PIN2-GFP

280     (or α-PIN2) signal was 2-fold reduced at the PM of *sfh8*/KISC mutants (**Figure 5A, B**). At the

281     same time, PIN2 accumulated in endosome-like structures in *sfh8*, while KISC or *sfh8* mutants

282     showed reduced PIN2 polarity (**Figure 5B, C**; at regions 3-4). Endosomes were also observed

283     for PIN1 protein in *sfh8* but not to non-polar proteins (H$^+$-ATPase - AHA1 or plasma membrane

284     intrinsic protein 2a - PIP2a), speaking against a general role for SFH8 in exocytosis (**Figure S5C,**

285     **D**).

286     Next, we asked whether SFH8 can promote the delivery/stability of PIN2 at polar domains.

287     We thus used the drug brefeldin-A (BFA) to form intracellular agglomerates of PIN2 in the so-

288     called "BFA-bodies" (aggregate of TGN and Golgi). We were able to calculate the uptake of PIN2

289     to BFA-bodies from the PM, and the delivery rate from PIN2-positive BFA-bodies to the PM

290     following washout of the BFA (Paponov et al., 2019). We further combined BFA experiments with

291     FRAP to measure the PIN2 delivery rate at the PM. Both assays confirmed that in *sfh8*/KISC

292     mutants PIN2 delivery to the PM was compromised, while PIN2 endocytosis was not

293     compromised, as PIN2-positive BFA-bodies were produced in both WT and *sfh8* mutants at the

294     same rate; these effects were independent of *de novo* PIN2 synthesis as cycloheximide (CHX)

295     treatments did not affect delivery rates or dissolve the PIN2 endosomes in *sfh8* (**Figure 5D-F,**

296     **S5E, F**).

297     To address the mechanism by which SFH8 could affect PIN2 delivery we checked whether

298     SFH8 stabilized PIN2 at the PM. At root region 3, SFH8-mScarlet (and Kin7.3) but not mScarlet-

299     SFH8 showed similar polarity and colocalized with PIN2 (**Figure 5G-I**; PCC ~0.9), while in regions

300     1-2 PIN2-GFP and mScarlet-SFH8 PM puncta excluded each other as shown in a super-

301     resolution setting (**Figure 5J**; insets). This anticorrelated localization implied PIN2 removal from

302    the PM through endocytosis. Yet, SFH8 is unlikely to promote PIN2 internalization via clathrin-

303    mediated endocytosis as it ii) did not affect PIN2 endocytosis (see above BFA experiment), and

304    ii) did not interact with Clathrin Light Chain (CLC2)-GFP or affected endocytosis of the dye FM4-

305    64 or the peptide PEP1 (**Figures 5D, S5G, H**). Thus full-length PM SFH8 clusters may reduce

306    access to certain polar proteins, perhaps through the "entropic bristle" effect exerted by the IDR

307    that could establish "fusion-depletion zones" at early developmental stages, while it may exert a

308    positive effect on fusion at later stages (see below).

309          As PIN2 showed colocalization at the PM with regions where SFH8$^{\Delta IDR}$ had formed, we

310    tested whether SFH8$^{\Delta IDR}$ could associate with PIN2. Using a custom-specific antibody against

311    SFH8 (C-terminus), we observed that in *pin2* mutants SFH8 was not affected suggesting that

312    SFH8 likely recruits PIN2, and not the other way around (**Figure S6A** and **6C** for antibody

313    specificity). To test direct PIN2/SFH8 interaction we refined a quantitative proximity ligation assay

314    (PLA; (Teale et al., 2021)). PLAs use complementary oligonucleotides fused to antibodies to

315    determine the frequency with which proteins of interest find themselves nearby (**Figure 6A**). In

316    PLA, we observed positive interactions in meristems mainly of region 3 using two different

317    settings: i) in GFP-PIN2 expressing roots (PLA antibody combination α-GFP/α-SFH8), or ii) in

318    PIN2-GFP with C-terminally HF-tagged SFH8 (PLA antibody combination α-GFP/α-FLAG).

319    Significantly reduced PLA signals were observed between PIN2/SFH8 in the N-terminally tagged

320    HF-SFH8 lines, while no signals were observed for i) SFH8 and a PM aquaporin (PIP2a), ii) *sfh8*

321    (PIN2/α-SFH8), and iii) in the vasculature where PIN2 is absent (**Figures 6B-E, S6B-D**). PLA

322    showed that Kin7.3 interacted exclusively at the PM with SFH8 (**Figure S6C**; region 3 onwards).

323    We corroborated PLA results using Fösters Resonance Energy Transfer (FRET) analyses,

324    showing that high FRET efficiency for the SFH8-mScarlet/PIN2-GFP pair, indicative of interaction,

325    was evident at the root regions 3-4 (**Figure 6F, S6**). We verified also the PM interaction of

326    ESP/Kin7.3 in the same region, using as FRET readout the N/C-terminus intramolecular

327    interaction of Kin7.3 in the *rsw4* background; Kin7.3 folded over on the PM in *rsw4* background

328    as previously suggested for MT binding (**Figure S6B**; Moschou et al., 2016). Collectively, these

329    results show that SFH8 filaments associate with PIN2 at the PM.

330          Next, we asked whether the SFH8/PIN2 anti-correlation related to stereochemical

331    hindrance imposed by SFH8 clusters that restrained fusion (the aforementioned entropic bristle

332    hypothesis). We thus established an *in vitro* membrane fusion assay based on cholesterol-

333    modified DNA zippers ("lipid-DNA-zippers" (Stengel et al., 2008) (**Figure 6G**). This minimalistic

334    approach lacked other proteins, allowing to focus on direct SFH8 effects. To test SFH8-mediated

335    membrane fusion, we used assays with low content of labeled phosphatidylethanolamine (PE)-

336     texas red (peripheral labeling), and fluorescein-containing large unilamellar vesicles (LUVs; 400

337     nm). Under our super-resolution settings, we could resolve three events driven by DNA zippers:

338     membrane tethering, hemifusion (lipid mixing), and fusion which resulted in the lipid bilayer

339     unification and the intermixing of the volumes. As SFH8$^{\Delta IDR}$ converted to filaments in a few

340     minutes, and could thus precipitate in lipid co-flotation or co-sedimentation assays, to ascertain

341     affinities and exclude non-specific effects on fusion by the phase behavior of the used proteins,

342     we used Quartz Crystal Microbalance with Dissipation monitoring to monitor in real-time binding

343     on LUVs, confirming validity of our system (**Figure S6F-I**). SFH8/SFH8$^{\Delta IDR}$ showed similar

344     affinities for the LUVs, excluding differential binding in this setting as a potential driver of fusion

345     (**Figure S6F-I**). In the SFH8$^{\Delta IDR}$ samples, the average diameter of liposomes was ~1 µm, in

346     contrast to SFH8 (~0.5 µm) which was below that in the free GST samples (~0.7 µm) used as

347     controls (**Figure 6H**). Content mixing analyses showed that almost 30% of the SFH8$^{\Delta IDR}$ samples

348     had semi-fused or fused LUVs (2-fold lower for the full-length SFH8; **Figure 6H-J**), while

349     fusion/hemifusion events in SFH8 were less than those of GST. This result suggests that SDH8$^{IDR}$

350     blocks fusion, while SFH8$^{\Delta IDR}$ may reduce the energy barrier required for fusion through the

351     increase in fluidity by its filamentous structure (Carlini et al., 2020) or the reduction of the entropic

352     bristle effect. Although the exact mechanism underlying SFH8 fusogenic activity is still an open

353     question, our results suggest that SFH8$^{IDR}$ can restrain vesicles from reaching membranes.

354     ***KISC/SFH8 Define a Positive Feedback Loop on Auxin Transport***

355     We asked whether KISC/SFH8 phase transitions have a developmental impact, by examining

356     whether defects of PINs in *sfh8* are sufficient to drive changes in auxin signaling. Through the

357     ratiometric auxin input R2D2 and the DR5 auxin output sensors (R2D2 principle is detailed in

358     **Supplemental Info**), we could confirm auxin defects in *sfh8* and KISC mutants with occasional

359     ectopic auxin input or output in distal meristem regions, consistent with perturbations in auxin

360     signaling robustness (**Figure 7A, B**). qRT-PCR showed reduced expression robustness of

361     selected auxin-related genes at root meristems of *sfh8* and *K135* (**Figure S7A**). Using imaging,

362     we confirmed that the least robust gene out of the ones tested, *yucca2* showed surprising

363     expression variation in the *sfh8* mutant among root cells (**Figure S7B**). Yet, gene expression

364     patterns of auxin-related genes were rather moderately affected in *sfh8* or KISC mutants

365     suggesting that auxin signaling buffers to some extent perturbations of polar auxin transport in a

366     cell-autonomous manner. Overall, the auxin signaling changes are consistent with a model in

367     which SFH8/KISC-mediated defects in PINs affect the robustness of auxin signaling.

368    We further postulated that reciprocally auxin could affect SFH8/KISC localization, as at
369    cells with auxin levels SFH8 was in the clustered state (e.g. region 1). PM-resident mNeon-SFH8
370    signal increased in the presence of exogenous auxin (IAA; 15 min 100nM; **Figure 7C**). On the
371    contrary, under the same conditions, GFP-Kin7.3 showed a slight decrease at the PM, and
372    reduced overall colocalization with SFH8-mScarlet clusters in TIRFM (**Figure 7D, E**).
373    Furthermore, IAA (or NAA) increased clusters of SFH8 and their size, while it did not increase
374    SFH8 filament occurrence, and diffusion at the PM (**Figure 7F, G**). Yet, when diffusing SFH8
375    condensates were nearby pre-established KISC filaments, they showed a "hop" diffusion
376    consistent with sterical entrapment on MTs. Consistently, prolonged IAA treatment led to SFH8
377    cleavage reduction (**Figure 7H**). Thus, auxin could induce SFH8 clustering at the PM and perhaps
378    entrap SFH8 in lipid patches where SFH8 undergoes LLPS.

379    **DISCUSSION**

380    Through the discovery of the KISC-SFH8 link, we identify a developmental module incorporating
381    protein material properties switches. Collectively, this mechanism comprises an array of events
382    summing from i) auxin-controlled SFH8 LLPS at the two-dimensional space of the PM, ii)
383    reduction of SFH8 clustering when auxin drops, and consequent interaction with KISC/SFH8 and
384    iii) proteolytic SFH8 cleavage accompanied by structural modifications enabling its functional
385    switching that reinforces maintenance but not initial polarity, e.g. of PIN2. This reinforcement
386    contributes to the robustness of auxin signaling, although we believe that this pathway has
387    extended functions. Interestingly, the phase transition of SFH8 is induced by limited proteolysis
388    executed by the highly conserved protease ESP, thereby expanding the repertoire of ESP
389    functions. This developmental module also uncovers a novel way to regulate protein phase
390    transition by showing that limited proteolysis is a post-translational modification involved in LLPS.

391    PS patches form at the PM when auxin levels are high, thereby, stabilizing ROP6 to
392    amplify signaling outputs (Platre et al., 2019) or reinforce polar domains in leaves (Pan et al.,
393    2020). In contrast to the ROP6, SFH8 recruits KISC at low auxin levels, while it is incompetent to
394    interact with KISC when it is in auxin-induced clusters. Because SFH8 interacts with PS and
395    shows reduced clustering in the distal meristem, we suggest that SFH8 condensation could be
396    promoted by PS or PIs patches. These lipids could buffer the highly positive localized charge of
397    SFH8, especially at the nodulin domain thereby enabling the condensation required for LLPS.

398    It has long been understood that molecular condensation is crucial for out of equilibrium
399    polarity establishment in biological systems. At first glance, our work seems counterintuitive as it
400    starts challenging these models by showing that LLPS may simply be a mechanism for reducing

12

401 polarized secretion, in contrast for example to what has been observed in synapses where protein
402 condensation can increase localized secretion (Milovanovic et al., 2018). On the contrary, SFH8
403 becomes functionally important for polarity at a less "condensed" state upon ESP-mediated
404 removal of the N-terminal IDR at the PM. This event preludes further structural reconfigurations
405 and material properties shifts (from LLPS to solid filaments) that promote a functionality switch of
406 SFH8: from fusion-blocker to fusion enhancer. Likewise, Dynamin-related proteins (DRPs)
407 oligomerize into high order macro-molecular structures for membrane remodeling
408 (Ramachandran, 2018), while coronaviruses (e.g. SARS-CoV-2) opt host proteases for structural
409 reconfiguration that prime fusogenic activity of SPIKE that results in the viral- host cell fusion
410 (Earnest et al., 2015; Tang et al., 2020). Upon IDR removal, SFH8$^{\Delta IDR}$ is stabilized likely due to
411 reduced intramolecular stereochemical repulsion and charge attenuation enabling filamentous
412 state conversion and fusion at polar domains. Overall, this mechanism establishes an example of
413 LLPS at the PMs in plants with importance for PM micropatterning that transcends to polarized
414 patterns.

415 Furthermore, the dimensionality reduction caused by the PM binding of SFH8 promotes
416 condensation, which would be otherwise impossible at low SFH8 levels. Cluster formation through
417 LLPS could have a direct effect on PM properties. The microscale "entropic bristle"-like properties
418 of the SFH8$^{IDR}$ when forming mesoscale condensates in the cytoplasm implies that when bound
419 to the PM SFH8$^{IDR}$ can restrict the accessibility of certain proteins to the PM at defined domains.
420 We could reconcile this proposition *in vitro* using specialized fusion assays. Thereby, the removal
421 of this IDR by ESP could locally promote vesicular fusion by removing steric hindrance effects or
422 by promoting structural reconfigurations. Alternatively, SFH8 clusters may engulf diffraction-
423 limited vesicles and promote their fusion upon IDR removal. Because SFH8 is a SEC14-like
424 protein, it may render lipids vulnerable to enzymatic modifications (Kf de Campos and Schaaf,
425 2017), regulating local lipid environments at a micro- or nanoscale.

426 Addressing further how KISC/SFH8 properties are involved in the maintenance of polar
427 domains will be an important priority for our future research. Intriguingly, the IDR region at the N-
428 terminus is conserved throughout evolution (**File S2**), suggesting that similar mechanisms may
429 apply in other eukaryotes. Thus, our work provides insights relevant to the burgeoning field of
430 biomolecular condensates interfacing with membranes.

13

431   **METHODS**

432   ***Arabidopsis backgrounds and ecotypes***

433   All the plant lines used in this study were in the *Arabidopsis thaliana* Columbia-0 (Col-0) ecotype

434   except the ones as indicated individually, and a detailed description can be found in Materials

435   Table. Primers used for genotyping, qRT-PCR, and cloning can be found in **Table S1**. The

436   following mutants and transgenic lines used in this study were described previously: *rsw4* mutant

437   (Wiedemeier et al., 2002), *K135* (Moschou et al., 2016), pro35S:mCherry-MAP4$^{MBD}$ (Moschou et

438   al., 2016), p35S:smRS-GFP-TUB6, pro35S:smRS-GFP-TUA6 (Nottingham *Arabidopsis* Stock

439   Center-NASC; N6550), p35S:GFP-TUB9 (NASC; M84706), pPIN1:PIN1-GFP(Benková et al.,

440   2003), pPIN2:PIN2-EGFP (Xu and Scheres, 2005); pPIN3:PIN3-EGFP, pPIN4:PIN4-EGFP and

441   pPIN7:PIN7-EGFP (Blilou et al., 2005),  DR5v2-ntdTomato / DR5-n3GFP (R2D2) (Liao et

442   al,2015),  Cytrap: pHTR2:CDT1a(C3)-RFP/pCYCB1:CYCB1-GFP (Yin et al., 2014).

443   proSNX1:SNX1-mRFP (Jaillais et al., 2006), pTIP1:TIP1-GFP (Ma et al., 2004), p35S:GFP-PIP2a

444   (Cutler et al., 2000), p35S:GFP-AHA1 (Hashimoto-Sugimoto et al.,2013), WAVE22, WAVE27

445   (Geldner et al., 2009). DR5rev:erTagRFP/pTCS:nGFP (Siligato et al., 2016),  In Wassilewskija

446   background: pCLC2:CLC2-EGFP (Konopka et al., 2008). The following lines were ordered from

447   GABI or NASC: *sfh8-1*: GABI_55IF03, *sfh8-2*: SALK_006862.

448       *Arabidopsis* plants were transformed according to (Clough and Bent, 1998) using

449   *Agrobacterium tumefaciens* strain GV3101. In all experiments, plants from T1 (co-localization

450   experiments), T2, or T3 (for physiology experiments) generations were used. The *Arabidopsis*

451   fluorescence marker lines were crossed with *sfh8-1* and corresponding SFH8 transgenic lines to

452   avoid the gene expression levels differences caused by positional effects; F1 (co-localization

453   experiments) and F2 were used in experiments.

454   ***Plant growth conditions***

455   *Arabidopsis* seedlings were sterilized and germinated on ½ strength Murashige and Skoog (MS)

456   agar media under long-day conditions (16h-light/8h-dark) and were harvested, treated, or

457   examined as indicated in the context of each experiment. In all experiments involving the use of

458   mutants or pharmacological treatments, media was supplemented with 1% (w/v) sucrose.

459   Arabidopsis plants/lines for crosses, phenotyping of the above-ground part, and seed harvesting

460   were grown on soil in plant chamber at 22°C/19 °C, 14/10 h light/dark cycle, and light intensity

461   150 μE m$^{-2}$ s$^{-1}$. *N. benthamiana* plants were grown in Aralab or Percival cabinets at 22°C (or 28-

462  30ºC for restrictive temperature treatments in the case of *rsw4*), 16/8 h light/dark cycle, and light

463  intensity 150 µE m$^{-2}$ s$^{-1}$.

### *Plant Material, phenotypic analysis, and drug treatments*

465  For quantification of phenotypes, seedlings were sterilized and grown vertically. Customized

466  Smart Plate Imaging Robot (SPIRO) imaging was done with 15 min intervals of fully automated

467  imaging acquisition (https://www.alyonaminina.org/spiro), in a growth cabinet (Aralab). For a

468  given genotype, differential contrast interference (DIC) images were captured on a Leica DM2500,

469  Leica DM6B, or Leica DM6000. Arabidopsis Col-0 was used as the wild-type control. To define

470  root length, images were captured of the plates using a Leica DM6000 with a motorized stage

471  and computationally compiled together. Root length or size was determined using Image J/Fiji

472  (National Institute of Health). For 1,6-hexanediol treatments, 10% (v/v) aqueous solution was

473  used. XVE-driven expression was activated by transferring seedlings on plates containing various

474  estradiol (in ethanol; light-tight tube aliquots) concentrations, which we determined experimentally

475  in trial experiments (2-100 µM).

### *Evolutionary relationships of taxa and sequences analyses*

477  The evolutionary history of SFH8 was inferred using the Neighbor-Joining method (Saitou and

478  Nei, 1987). The optimal tree is shown. The percentage of replicate trees in which the associated

479  taxa clustered together in the bootstrap test (1000 replicates) is shown next to the branches

480  (Felsenstein, 1985). The evolutionary distances were computed using the Poisson correction

481  method (Zuckerkandl and Pauling, 1965) and are in the units of the number of amino acid

482  substitutions per site. This analysis involved 201 amino acid sequences. All positions with less

483  than 70% site coverage were eliminated, i.e., fewer than 30% alignment gaps, missing data, and

484  ambiguous bases were allowed at any position (partial deletion option). There were a total of 611

485  positions in the final dataset. Evolutionary analyses were conducted in MEGA X (Kumar et al.,

486  2018).

### *Transient N. benthamiana assays*

488  For transient assays, *Agrobacterium tumefaciens* strain GV3101 was used. Infiltrations were done

489  as described previously (Arora et al., 2020). During treatments, plants were kept in defined growth

490  conditions in an Aralab growth chamber.

### *Root gravitropism assays*

To observe root gravitropism, plants were grown vertically on plates (½ strength MS agar media under long-day conditions (16h-light/8h-dark) for 12 DAG. The root tip angle change was measured using Fiji.

### *Cloning and Plasmids*

Primer sequences used for amplicons are listed in **Table S1**. Clonings were done either by Gateway, restriction enzyme digestion, or In-fusion (Takara). The following constructs were produced in: i) pENTR vectors were generated via BP reaction with pDONR/Zeo (Invitrogen) and PCR products: SFH genes (amplicons from RT-PCR using cDNA from 1-week-old seedlings), truncations of SFH8 (amplicons from pDONR/Zeo-SFH8 was used as a template), mutations of SFH8 by mutagenesis PCR using pDONR/Zeo-SFH8. The Kin7.3 and truncations were previously described (Moschou et al., 2016); ii) In pGWB601: pSFH8:mNeon-gSFH8 (g, for genomic), pRPS5a::mNeon-gSFH8, pKin7.3:mNeon-gSFH8, pSFH8:gSFH8-mNeon, pRPS5a:gSFH8-mNeon, pKin7.3:gSFH8-mNeon, pRPS5a::HF-mScarlet-gSFH8-mNeon, pRPS5a:HF-gSFH8, pRPS5a:gSFH8-HF, pKin7.3:CFP-cKin7.3-mNeon. The pGWB601 empty vector was used as a backbone, cut open by XhoI and SacI, then the vectors assembled by four or five- fragments using In-fusion cloning (amplicons from *Arabidopsis* genomic DNA, template for mNeon, mScarlet, and proKin7.3-CFP-cKin7.3); iii) pGBKT7/pGADT7-gateway-compatible (Maier et al., 2008) for Y2H: LR reaction with the pENTR vectors of Kin7.3 and truncations, SFH8, SFH8 truncations, and mutations; iv) ratiometric bimolecular fluorescence complementation (rBiFC)-gateway-compatible system (Grefen and Blatt, 2012): Kin7.3 (pDONR/P3P2-Kin7.3) and SFH8 (pDONR/P1P4-SFH8); v) pRPS5a gateway compatible dual tagged vectors: modified pGWB517 and 560 empty vectors were used as a backbone, cut open by HindIII and XbaI, and then the vectors assembled by two fragments In-fusion cloning (amplicons from Arabidopsis genomic DNA-1.6kb promoter of RPS5a and template for FLAG and sGFP). The Kin7.3 (pDONR/Zeo-Kin7.3) and SFH8 (pDONR/Zeo-SFH8) were used to generate the FRET pair and the biosensor, respectively; vi) pGAT4 and pDEST15 gateway compatible vectors for His- and GST-protein expression in *Escherichia coli*: full-length or truncations of Kin7.3 and SFH8 pDONR/Zeo vectors were used; vii) inducible constructs under the promoter of Kin7.3 (XVE): vector was cut with PmeI and MluI and then the vectors assembled by two fragment In-fusion cloning (amplicons from *Arabidopsis* genomic DNA-1.7kb promoter of Kin7.3 and part of LexA); inserts from pENTR-GFP-ESP and pENTR-HA-Kin7.3 tail were introduced by LR reaction from the corresponding pDONR/Zeo vectors; viii) The pDR gateway compatible vector for yeast temperature-sensitive complementation: LR reaction with

3

524 pDONR/Zeo-SFH8 and the indicated truncations (in pDONR/Zeo). The SYN4 cloning has been

525 described in Miniana et al., 2017.

### Yeast Two-Hybrid Screen

527 The genotype of the strain Y2HGold is *MATa, trp1-901, leu2-3, 112, ura3-52, his3-200, gal4Δ,*

528 *gal80Δ, LYS2::GAL1UAS-Gal1TATA-His3, GAL2UAS-Gal2TATA-Ade2, URA3::MEL1UAS-*

529 *Mel1TATA-AUR1-C MEL1*. The genotype of the strain Y187 is *MATα, ura3-52, his3-200, ade2-*

530 *101, trp1-901, leu2-3, 112, gal4Δ, gal80Δ, URA3::GAL1UAS-GAL1TATA-lacZ*. Transformed

531 yeast cells were incubated at 30°C until OD600=0.8 in a minimal medium (SD) lacking the amino

532 acid tryptophan. To confirm the expression of the baits, total protein (10 µg) was extracted using

533 alkaline lysis and resolved by SDS-PAGE. Fusion proteins were detected with α-Myc monoclonal

534 antibodies (Roche, Stockholm, Sweden). The following constructs were used: pBKGT7-AtESP

535 domain A (DomA; Moschou et al., 2016); pBKGT7-AtESP Domain C (DomC; Moschou et al.,

536 2016); pBKGT7-AtMau2 (Minina et al., 2017); pBKGT7-cKin7.3; pBKGT7-cKin7.3-motor;

537 pBKGT7-cKin7.3-tail (Moschou et al., 2016); The absence of self-activation was verified by a

538 transformation of the baits alone to select on minimal medium (SD) lacking the amino acids

539 leucine, histidine, and adenine. The baits were transformed into the strain Y2HGold and mated

540 with the Universal *Arabidopsis* cDNA Library (Clontech) in Y187. For pairwise Y2H assays, the

541 Gateway-compatible pGADT7 vector (Maier et al., 2008) and the yeast Y187 were used, including

542 the following constructs: pGADKT7-SCC2 (Minina et al., 2017); pGADKT7-cKin7.3-tail;

543 pGADKT7-cSFH8; pGADKT7-cSFH8-SEC14 domain (SD); pGADKT7-cSFH8-Nodulin;

544 pGADKT7-cSFH8-Nodulin[2KtoA]; pGADKT7-cSFH8-Nodulin[6Kto A] (or other indicated variants).

### Protein Expression and Purification

546 The pGAT4/PDEST15 constructs were transformed in BL21 (DE3) Rosetta or BL21 (DE3)

547 Rosetta II *Escherichia coli* cells. Bacterial cultures were grown in 800 mL of LB supplemented

548 with 100 mg L$^{-1}$ of ampicillin and 25 mg L$^{-1}$ of chloramphenicol. Protein expression was induced

549 at OD$_{600}$=0.5 with 0.05 to 1 mM IPTG (Isopropyl ß-D-1-thiogalactopyranoside). After 3 h the cells

550 were harvested by centrifugation at 2,500g for 20 min at room temperature and frozen overnight

551 at -80°C. Preparation of his-tagged recombinant proteins was performed according to

552 manufacturer instructions (Qiagen). Preparation of GST-tagged recombinant proteins was

553 performed according to manufacturer instructions, using Sepharose beads (GE Healthcare Life

554 Sciences), while the pH of purification was 8.3 (otherwise the SFH8 proteins precipitated).

555 Expression levels of proteins were estimated by CBB stainings in PAGE or by Western blots. The

556 proteins were dialyzed overnight in assay buffers (2 L).

### GST Pull-Down Assay

558 The GST pull-downs were performed by binding 10 µg of GST fusion proteins to glutathione

559 Sepharose beads (GE Healthcare Life Sciences) and incubating them with 10 µg of his-tagged

560 proteins in a binding buffer containing 25 mM Tris-HCl (pH 8.0), 150 mM NaCl, and 0.5% Nonidet

561 P-40. After an incubation of 1 h at 4°C, beads were washed three times with the wash buffer

562 containing 25 mM Tris-HCl (pH 8.0), 150-300 mM NaCl, and 0.5% (v/v) Nonidet P-40. Proteins

563 were then eluted from the washed beads with glutathione and analyzed by SDS-PAGE. Purified

564 proteins were dialyzed against 75 mM PIPES (piperazine-N, N′-bis; pH 6.8), 1 mM EGTA

565 (ethylene glycol-bis(β-aminoethyl ether)-N,N,N′,N′-tetraacetic acid), 1 mM $MgCl_2$, and 10% (v/v)

566 glycerol, 1 mM DTT (dithiothreitol), and 70 mM KCl. Expression levels of proteins were estimated

567 by western blot. As a negative control, GST protein was used in all assays.

### Protein Immunopurification

569 *Agrobacterium* strain GV3101 carrying constructs expressing various forms of Kin7.3, SYN4,

570 SFH8, ESP or TAP-GFP were infiltrated into *N. benthamiana* leaves. Three-four days later, leaves

571 were grounded in liquid nitrogen and resuspended in ten volumes of buffer A (50 mM Tris-HCl

572 [pH 7.5], 5% [v/v] glycerol, 10% [v/v] Ficoll, 0.1% [v/v] Triton X-100, 300 mM NaCl, 5 mM MgCl2,

573 1 mM EDTA, 1 mM EGTA, plant-specific protease inhibitor cocktail [Sigma], phosphatase

574 inhibitors [Roche], and 1 mM PMSF) and centrifuged at 14,000 x g for 20 min at 4 °C. The

575 supernatant was filtered through four layers of Miracloth (Calbiochem). For TAP-ESP capture,

576 samples were mixed with immunoglobulin G beads and incubated at 4°C for 1 h with gentle

577 rotation. Beads were precipitated by centrifugation at 300 g, washed three times with buffer A,

578 and treated for 4 hr with PreScission protease (GE Healthcare). The TAP-ESP beads were used

579 directly or the supernatant was incubated for 30 min with nickel beads and h-AtESP was eluted

580 with 250 mM imidazole containing buffer A. Protein was dialyzed against 0.1M PIPES (pH 6.8),

581 5mM EGTA, 2mM $MgCl_2$, and 20% (v/v) glycerol buffer. Protein levels were estimated by Western

582 blot.

### SFH8 in vitro cleavage assay

584 GFP-ESP was extracted from infiltrated *N. benthamiana* leaves as above using GFP-TRAP

585 (CromoTek). GFP-ESP protein lysates were mixed with GST beads carrying GST-SFH8 or the

586 corresponding mutants. The samples were left agitating at 37°C for 1-2 h, resolved by SDS-
587 PAGE, and detected by Western blot.

### Preparation of liposomes

589 1,2-dioleoyl-sn-glycerol-3-phosphocholine (DOPC), 1,2-dioleoyl-sn-glycerol-3-phospho-L-serine
590 (DOPS), 1,2-dioleoyl-sn-glycerol-3-phospho-(1'-myo-inositol-4',5'-bisphosphate) (PI(4,5)P2) and
591 1,2-dioleoyl-sn-glycerol-3-[(N-(5-amino-1-carboxypentyl)iminodiacetic acid) succinyl] (DGS-
592 NTA(Ni)) lipids were purchased from Avanti Polar Lipids (Alabaster, Al, USA). Dipalmitoyl
593 phosphatidylinositol 3-phosphate (PI3P) lipids were from Echelon Biosciences Incorporated
594 (EBI). Lyophilized lipids were dissolved in 1:1 (v/v) chloroform:methanol mixed in glass flasks in
595 the desired amount. The organic solvent was first evaporated under a gentle stream of nitrogen
596 while gently turning the flask to form a thin lipid film onto the wall of the flask. The lipid film was
597 further dried with nitrogen for at least 30 min. Lipid films were hydrated in a buffer containing
598 10mM Tris-Cl, pH 7.5 (Merck), 150mM NaCl at a final concentration of 2mg/ml. After vortexing for
599 30 minutes, the resulting multilamellar vesicle solutions were extruded 25 times through a
600 polycarbonate membrane with 50 or 200 nm nominal pore diameter (LiposoFast, Avestin) leading
601 to a stock solution of unilamellar vesicles which were stored at 4°C and used for 5 d at maximum.

### Protein labeling for LLPS

603 The dyes used for labeling were Alexa Fluor™ 647 C2 Maleimide and Alexa Fluor™ 555 C2
604 Maleimide (ThermoFischer Scientific). The dyes were dissolved in water-free DMSO (dimethyl
605 sulfoxide) at a concentration of 1mM. After the protein isolation with GST-affinity chromatography,
606 the proteins were dialyzed against 20mM Tris-HCl pH 7.5, 150mM NaCl. Proteins were partially
607 labeled in solution in a ratio of 1 mol protein to 0.1 mol (1:10 molar ratio labeled/unlabeled) of dye
608 for 15 min on ice. The labeled proteins were kept at 4°C and used within the next 3 d.

### Preparation of surfaces for suspended liposomes

610 Before the experiments, Au-coated AT-cut crystals (QSX-301 Biolin Scientific, Q-Sense, Sweden)
611 were immersed in 2% (v/v) Hellmanex solution and rinsed with double distilled water. The gold
612 sensors were further dried using nitrogen flow and cleaned using UV-ozone cleaner (E511,
613 Ossila, Sheffield, UK) for 30min. The QCM-D experiments were performed using the Q-Sense E4
614 (Biolin, Q-Sense, Sweden) instrument and AT-cut quartz disks (5MHz). All the experiments were
615 performed in a buffer solution under a constant flow rate of 50 µL/min at 25 °C. Briefly, the gold
616 surface was equilibrated with buffer; followed by neutravidin adsorption (200µL, 0.2mg/mL protein

617    solution). 5'-biotinylated, 3'-cholesterol modified DNA was then used (200µL, 0.075pmol/µL) as a

618    binding anchor to liposomes of different lipid compositions as previously described (Milioni et al.,

619    2020). All liposome solutions were used at a concentration of 0.2mg/ml and a final volume of

620    700µL. Finally, protein solutions of various concentrations were added at a volume of 500µL.

### *Supported Lipid bilayer with DGS-NTA(Ni)*

622    Supported lipid bilayers containing 1% (v/v) DGS-NTA(Ni) were formed on $SiO_2$ coated sensors

623    (Q-Sense QSX 303) upon the addition of 0.05 mg/mL lipid solution. Final frequency and

624    dissipation changes were Δf=-170 Hz and ΔD = 0.13 x $10^{-6}$. These values are typical of the

625    formation of a homogeneous supported lipid bilayer.

### *Liposome-protein binding assays*

627    For the liposome-protein pull-down assays, we used 25 µl of Small Unilamellar Vesicles (SUVs,

628    2 mg/ml) combined with approximately 500ng of the protein of interest. Before binding we

629    centrifuged the proteins at 16,000 × g, at 4°C, for 5 min, to avoid precipitates (Julkowska et al.,

630    2013). Twenty-five µl of protein mix with 25 µL liposome suspension were combined and

631    incubated on an orbital shaker platform for 30-45 min at room temperature. The binding buffer

632    consisted of 150 mM KCl, 25 mM Tris–HCl pH 7.5, 1 mM DTT, 0.5 mM EDTA. The samples were

633    centrifuged at 16,000g for 30 min at room temperature, we harvested the supernatant (we added

634    16.7 µL of 4× Laemmli sample buffer to a supernatant fraction) and resuspended the liposome

635    pellet in 300-500 µl 1× binding buffer. The centrifugation was repeated in the same conditions

636    and we resuspended the liposome-protein pellet in 33 µL 4x Laemmli buffer. All samples were

637    incubated at 95°C for 5 min and loaded 10 µL on SDS-PAGE for Western blot.

### *Liposome DNA-mediated fusion assay and SUPER template setting*

639    To establish DNA-zippers, we adjusted concentrations of oligomers-cholesterol and used various

640    temperatures (4-25°C) to achieve DNA-zipper-driven fusion at a percentage lower than ~10%

641    (noise). Eventually, all liposomes irrespective of the conditions used, given enough time fused to

642    a percentage of ~50%. The liposomes used were LUVs of 400 nm diameter, with the following

643    composition: DOPC 71.5%, DOPS 27.5%, PE-Texas Red conjugated 0.5% and $PI(4,5)P_2$ 0.5%

644    (PS was included for SUPER template experiment to provide required membrane flexibility). We

645    also used LUVs without PE-Texas Red lipid. Instead, they carried the fluorophore fluorescein (cf,

646    100 mM fluorescein in Tris-Cl pH 7.5). For the fusion of the two different liposomes populations,

647    we incubated each with a DNA primer for 45 min at room temperature. The sequence of the

648     single-stranded DNA molecules can be found in **Table S1**. For every liposome, we used 100 DNA

649     molecules (Peruzzi et al., 2019). SUPER templates were prepared, as described previously

650     (Pucadyil and Schmid, 2010). Silica beads (monodispersed 4.9 μm in diameter; Corpuscular Inc.,

651     Cold Spring, NY) were added to a premixed solution of liposomes in LLPS buffer in a total volume

652     of 100 μL in a 1.5 mL clear polypropylene centrifuge tube. Glass coverslips (Fisher Scientific,

653     Pittsburgh, PA) were cleaned with piranha solution (concentration $H_2SO_4$/30% $H_2O_2$ 4:1, v/v) for

654     1 h at room temperature and washed extensively with boiling water. The coverslips were allowed

655     to attain room temperature, stored under water, and air-dried before use. To coat the coverslips

656     with PEG-silane, piranha-cleaned coverslips were first dried in an oven at 200°C for 3 h and then

657     treated at room temperature for 30 min with PEG-silane (2%, v/v; Gelest Inc., Morrisville, PA) in

658     acetone. The coverslips were later washed extensively with water and air-dried before use. The

659     samples were observed with confocal LIGHTNING SP8 module (high speed and resolution of 120

660     nm) using an observation chamber and an Apochromat 63x objective (N.A.=1.4). images were

661     deconvoluted by Leica built-in software.

### *Phase separation assays*

663     The slides and coverslips used for confocal microscopy were treated overnight with 1-2 mg/mL

664     PLL-PEG, after cleaning with 2% (v/v) Hellmanex for approximately 2 h, at room temperature.

665     The LLPS buffer used was the following: 10 mM HEPES (4-(2-hydroxyethyl)-1-piperazine ethane

666     sulfonic acid), 150 mM NaCl, 0.1 mM EDTA, 2 mM DTT, pH 7.4 with and without 10% (w/v)

667     polyethylene glycol (PEG 3000) as a crowding agent. The amount of the added labeled protein

668     was 1-2 μM for 3 h at room temperature. Some of our samples contained Large Unilamellar

669     Vesicles (LUVs) consisting of DOPC 0.5%: DOPS 99%: DOPE-Texas Red 0.5%. Phase

670     separation was imaged via confocal microscopy.

### *Whole-mount proximity ligation assay (PLA) and Immunocytochemistry*

672     Four to five-day-old seedlings were fixed and permeabilized as described (Moschou et al., 2016).

673     SFH8    antibody    was    raised    against    the    unique    peptide    sequence    517-

674     GNAIELGSNGEGVKEECRPPSPVPDLTET-545   in   rabbits   using   standard   immunogenic

675     procedures. Primary antibody combination 1:200 for α-GFP mouse [Sigma-Aldrich, SAB2702197]

676     and 1:100 for α-SFH8 rabbit, 1:100 for α-mNeon mouse [Chromotek, 32F6 ] and 1:100 for α-SFH8

677     rabbit or 1:200 for α-FLAG mouse [Sigma-Aldrich, F1804] and 1:200 for α-GFP rabbit [Millipore,

678     AB10145]) were used for overnight incubation at 4°C. Roots were then washed with MT-stabilizing

679     buffer (MTSB: 50 mM PIPES, 5 mM EGTA, 2 mM $MgSO_4$, 0,1% (v/v) Triton X-100) and incubated

8

680 at 37°C for 3 h either with α-mouse plus and α-rabbit minus for PLA assay (Sigma-Aldrich,

681 Duolink). PLA samples were then washed with MTSB and incubated for 3 h at 37°C with ligase

682 solution as described (Pasternak et al, 2018). Roots were then washed 2x with buffer A (Sigma-

683 Aldrich, Duolink) and treated for 4 h at 37°C in a polymerase solution containing fluorescent

684 nucleotides as described (Sigma-Aldrich, Duolink). Samples were then washed 2x with buffer B

685 (Sigma-Aldrich, Duolink), with 1% (v/v) buffer B for another 5 min, and then the specimens were

686 mounted in Vectashield (Vector Laboratories) medium.

687  Immunocytochemistry was done as described previously (Moschou et al., 2016). The

688 primary antibodies used were rabbit α-SFH8 (diluted 1:500), rat α-tubulin YL1/2 (1:200; Santa

689 Cruz Biotechnology), mouse α-FLAG (1:250), and sheep α-PIN2 (1:500). Specimens were

690 washed three times for 90 min in PBST and incubated overnight with donkey α-sheep conjugated

691 Alexa fluor 488, goat α-mouse tetramethylrhodamine isothiocyanate (TRITC), α-rat TRITC, and

692 α-rabbit fluorescein isothiocyanate-conjugated (FITC) secondary antibodies diluted 1:200-250.

693 After washing 3x in PBST, specimens were mounted in Vectashield (Vector Laboratories)

694 medium.

695 ***rBiFC and protoplast transformation***

696 The rBiFC assay was done in Arabidopsis root protoplasts via PEG transformation as described

697 previously (Jeong et al., 2021). After 16h transformation, protoplasts were observed with a Zeiss

698 LSM780 laser scanning confocal microscope using 40×/1.2 W C-Apochromat in multi-track

699 channel mode. Excitation wavelengths and emission filters were 514 nm/band-pass 530-550 nm

700 for YFP, and 561 nm/band-pass 600-630 nm for RFP. Images were processed by Fiji.

701 ***Quantification of Fluorescent Intensity, FRAP and FRET***

702 To create the most comparable lines to measure the fluorescence intensity of reporters in multiple

703 mutant backgrounds, we crossed homozygous mutant bearing the marker with either a WT plant

704 (outcross to yield progeny heterozygous for the recessive mutant alleles and the reporter) or

705 crossed to a mutant only plant (backcross to yield progeny homozygous for the recessive mutant

706 alleles and heterozygous for the reporter). Fluorescence was measured as a mean integrated

707 density in regions of interest (ROIs) with the subtraction of the background (a proximal region that

708 was unbleached and had less signal intensity than the signal of the ROI region). FRAP mode of

709 Zeiss 780 ZEN software was set up for the acquisition of 3 pre-bleach images, one bleach scan,

710 and 96 post-bleach scans (or more). Bleaching was performed using 488, 514, and 561 nm laser

711 lines at 100% transmittance and 20-40 iterations depending on the region and the axial resolution

712    (iterations increased in deeper tissues to compensate for the increased light scattering). In FRAP

713    the width of the bleached ROI was set at 2-10 μm. Pre- and post-bleach scans were at minimum

714    possible laser power (0.8 % transmittance) for the 458 nm or 514 nm (4.7%) and 5% for 561 nm;

715    512 x 512 8-bit pixel format; pinhole of 181 μm (>2 Airy units), and zoom factor of 2.0. The

716    background values were subtracted from the fluorescence recovery values, and the resulting

717    values were normalized by the first post-bleach time point and divided by the maximum point set

718    maximum intensity as 1. The objective used was a plan-apochromat 20x with NA=0.8 M27 (Zeiss).

719        GFP-AHA1, PIP2a-GFP, PIN2-GFP, mNeon-SFH8, and SFH8-mNeon fluorescence were

720    detected using a water- or oil-corrected 40x objective. During analyses, FRAP mode of Zeiss

721    Lsm780 ZEN software was set up for the acquisition of one pre bleach image, one bleach scan,

722    and 40 or more post bleach scans. The following settings were used for photobleaching: 10 to 40

723    iterations; 10 to 60 s per frame; 100% transmittance with the 458- to 514-nm laser lines of an

724    argon laser. Pre- and post bleach scans were at minimum possible laser power (1.4 to 20%

725    transmittance) for the 488 nm and 0% for all other laser lines; 512x512 pixel format; and zoom

726    factor of 5.1. The fluorescence intensity recovery values were determined, then the background

727    values were subtracted from the fluorescence recovery values, and the resulting values were

728    normalized against the first post bleach time point.

729        For FRET, either acceptor photobleaching (AB) or sensitized emission (SE) modules of

730    the SP8 Leica confocal microscope were used, using standard modules and internal calibration.

731    The acceptor photobleaching experiments were done as described previously (Moschou et al.,

732    2016), using the aforementioned parameters for FRAP. Fluorescence was detected using a

733    water- or oil-corrected 40x objective. For SE-FRET, The correction factors β, α, γ and δ were

734    calculated with the donor- and acceptor-only reference samples, as described for TMK1-AHA1

735    interaction (Lin et al., 2021).

### *TIRFM Imaging and Tracking Analyses*

737    TIRF microscopy images were acquired using MetaMorph software on an Olympus IX-81

738    microscope. The system was maintained at 37°C during imaging. A DV2 image splitter (MAG

739    Biosystems) was used to separate GFP and RFP emission signals. Time-lapse movies were

740    obtained with, 100 ms intervals. For MSD analysis, 30-s-long movies with 100 ms intervals and

741    200 ms exposure were used. Particle tracking was limited to the amount of time that PM remained

742    a single focal plane; the median track length was 2,000 frames, corresponding to 3.5 s of imaging.

743    The tracking of particles was performed with the Mosaic suite of FIJI or NanoTrackJ/TrackMate,

744    using the following typical parameters: radius 3 of fluorescence intensity, a link range of 1, cutoff

745    of 0.1%, and a maximum displacement of 8 px, assuming Brownian dynamics.

746    ***LC-MS/MS Lipids and Proteins Analyses and Overlay Assays of Lipids***

747    Lipid overlay assay PI strips were blocked in PBST (0.1% Tween 20 [vol/vol]) supplemented with

748    3% (w/v) fatty acid-free BSA (Sigma-Aldrich) overnight at 4°C and then incubated with 0.5 µg/ml

749    GST fusion proteins for 1 h at room temperature. After washes with PBST-BSA, the membranes

750    were incubated with rabbit α-GST for 1 h at room temperature, followed by IRDye 800 goat anti-

751    rabbit secondary antibody for 1 h.

752    Lipids were extracted from roots after inactivating the tissue with boiling water, or from

753    microsomes according to (Gasulla et al., 2013). Lipid classes were purified by solid-phase

754    extraction, and phospholipids, glycolipids, diacylglycerol, triacylglycerol, and total fatty acids were

755    measured by quadrupole time of flight mass spectrometry (Q-TOF MS/MS) or gas

756    chromatography–flame ionization detection (GC-FID), respectively, as previously described

757    (Wewer et al., 2014).

758    For proteomic analyses of FLAG-tagged SFH8 immunoprecipitates, samples were

759    analyzed by LC-MS using Nano LC-MS/MS (Dionex Ultimate 3000 578 RLSCnano System)

760    interfaced with Eclipse Tribrid mass spectrometer (ThermoFisher 579 Scientific). Samples were

761    loaded onto a fused silica trap column Acclaim PepMap 100, 580 75 µm x 2 cm (ThermoFisher

762    Scientific). After washing for 5 min at 5 µL/min with 0.1% (v/v) trifluoroacetic acid (TFA), the trap

763    column was brought in-line with an analytical 582 column (Nanoease MZ peptide BEH C18, 130

764    A, 1.7 µm, 75 µm x 250 mm, Waters) for 583 LC-MS/MS. Peptides were fractionated at 300 nL/min

765    using a segmented linear gradient 584 4-15% B in 30min (where A: 0.2% formic acid, and B:

766    0.16% formic acid, 80% 585 acetonitrile), 15-25% B in 40min, 25-50%B in 44 min, and 50-90% B

767    in 11 min. Solution B then returned at 4% for 5 min for the next run. The scan sequence began

768    with an MS1 spectrum (Orbitrap analysis, resolution 120,000, scan range from M/Z 350–1600,

769    automatic gain control (AGC) target 1E6, maximum injection time 100 ms). The top S (3 589 sec)

770    and dynamic exclusion of 60 sec were used for the selection of Parent ions for MS/MS. Parent

771    masses were isolated in the quadrupole with an isolation window of 1.4 591 m/z, automatic gain

772    control (AGC) target 1E5, and fragmented with higher-energy collisional dissociation with a

773    normalized collision energy of 30%. The fragments were scanned in Orbitrap with a resolution of

774    30,000. The MS/MS scan range was determined by the charge state of the parent ion but the

775    lower limit was set at 100 amu.

11

### *TAMRA-PEP1 and FM4-64 Internalization Assays*

The peptide PEP1 (ATKVKAKQRGKEKVSSGRPGQHN) was labeled with 5′-carboxytetramethylrhodamine at the N-terminus (TAMRA-PEP1) with an HPLC purity of 95.24% and molecular weight of 2905.24 (EZBiolab). The peptide was dissolved in water to obtain 1 mM peptide stocks. Further dilutions were done with ½ MS medium. Five-day-old seedlings were dipped into 1 mL ½ MS medium containing 100 nM TAMRA-PEP1 for 10 s, washed five times, and kept in 24-well plates with ½ MS medium for 40 min. Epidermal cells at the meristematic zone were imaged with a Zeiss LSM710 inverted laser scanning confocal equipped with 40×/1.2 W C-Apochromat M27 objective at a zoom factor of 3.5. TAMRA-PEP1 was excited at 559 nm, and fluorescence emission was captured between 570-670 nm, GFP was excited at 488 nm, and fluorescence emission was captured between 500-540 nm. Image quantification was done using Fiji software. To this end, the PM of individual cells was selected with the brush tool with a size of 10 pixels as well as the intracellular space with the polygon selection tool. The average intensity of the top 100 highest pixels for both the plasma membrane and the intracellular space was used to obtain a ratio between intracellular and plasma membrane fluorescence. Five epidermal cells from five plants were quantified.

The FM4-64 experiments were as described in Moschou et al., 2013. In brief pulse labeling with FM4-64 (2 μM FM464, Molecular Probes; made from a 2mM stock in DMSO) was done for 5 min (time 0) and then analyzed for 18 min at room temperature in Zeiss Lsm 780 with excitation at 488 nm and fluorescence emission captured between 540-670 nm. After the pulse with FM4-64, the roots were washed two times in an ice-cold MS medium. Quantifications were done as described for the TAMRA-PEP1 experiments above.

### *RNA Extraction, RNAseq, and Quantitative RT-PCR Analysis*

Total RNA from the seedlings was extracted using the RNeasy Plant Mini Kit with DNaseI digestion (QIAGEN). Reverse transcription was carried out with 500 ng of total RNA using the iScript cDNA synthesis kit (Bio-Rad) according to the manufacturer's protocol. Quantitative PCR with gene-specific primers was performed with the SsoAdvanced SYBR Green Supermix (Bio-Rad) on a CFX96 Real-Time PCR detection system (BioRad). Signals were normalized to the reference genes ACTIN2 using the DCT method and relative expression of a target gene was calculated from the ratio of test samples to Col-0. For each genotype, three biological replicates were assayed in three qPCR replicates. qRT-PCR primers were designed using QuantPrime (www. quantprime.de)(Arvidsson et al., 2008). Primer sequences used for qRT-PCR can be found in **Table S1**.

12

809     *Super-resolution Imaging, Transmission Electron Microscopy, and Negative Staining*

810     Confocal SP8 Leica confocal microscope LIGHTNING module was used for super-resolution on

811     the fly imaging. Confocal images were obtained when indicated at maximum scanning speed (40

812     frames per second) using a 63x water immersion objective with a theoretical x/y-axial resolution

813     of 120 nm upon deconvolution. Post-acquisition, images were deconvoluted using the

814     LIGHTNING algorithm and water correction was set in the algorithm as the mounting medium.

815     Imaging was done at room temperature in an inverted microscope setting. Root samples were

816     fixed in a mixture of 1.25% (v/v) glutaraldehyde and 1.25% (v/v) paraformaldehyde in 50 mM

817     cacodylate buffer, pH 7.2, for 1 h. After washing in cacodylate buffer, samples were postfixed

818     overnight in 1% osmium tetroxide (prepared in cacodylate buffer), dehydrated in a graded ethanol

819     series, and embedded in London Resin White. Ultrathin sections were examined with a

820     transmission electron microscope at 80 kV without post staining. Negative staining was essentially

821     done as described for lipoproteins in (Rames et al., 2014).

822     **QUANTIFICATION AND STATISTICAL ANALYSIS**

823     Statistical analysis was performed in R studio (R-project.org) or GraphPad Prism (version 9.2.0).

824     Each data set was tested whether it followed a normal distribution (Gaussian) by the Shapiro-

825     Wilk, D' Agostino-Pearson, Anderson-Darling, and Kolmogorov-Smirnov normality tests.

826     Lognormal versus Gaussian distributions were also evaluated (not used though herein). For tests

827     involving pairwise comparisons, Student's t-test or Wilcoxon tests (or as indicated) were mainly

828     used to define whether differences were statistically significant. The significance threshold was

829     set at $p < 0.05$ (significance claim-level alpha) and the exact values are shown in graphs (very low

830     values are indicated as <0.0001). For tests involving multiple comparisons, 1-way ANOVA or the

831     Kruskal-Wallis test (nonparametric analog of ANOVA) was used followed by Dunnet's or Dunn's

832     multiple comparison test to define whether differences were statistically significant (or as

833     indicated). Graphs were generated by using Microsoft Excel, R, or GraphPad Prism 9.2.0. Details

834     of the statistical tests applied, including the choice of statistical method, and the exact number of

835     "n" is indicated in the corresponding figure legend or directly on the graph. In violin plots, upper

836     and lower dotted lines represent the first and third quantiles, respectively, horizontal lines mark

837     the mean, and edges mark the highest and lowest values. Plots were depicted truncated or

838     untruncated for aesthetic reasons.

839     Image analyses and intensity measurements were done using FIJI v. 1.49 software

840     (rsb.info.nih.gov/ij). The intensity of the fluorescence signal was measured as the Integrated

841     Density in a region of interest. The dwell time rate of tagged proteins in FRAP experiments was

13

842 calculated by the single exponential fit equations as described by (Chang et al., 2005). Co-
843 localization was analyzed using Pearson statistics (Spearman or Manders analyses produced
844 similar results)(French et al., 2008). Images were prepared by Adobe Photoshop v. 2021 (Adobe).
845 Statistical analyses were performed with JMP v. 9 or 11 (www.jmp.com), GraphPad, or R. Curve
846 fitting was done as we have described in detail for PCs (Deli et al., 2022). Time series movies
847 were compressed, corrected, and exported as .avi extension files. The unspecific fluorescence
848 decay was corrected using FIJI v. 1.49 software and default options using the bleaching correction
849 tool. Videos were digitally enhanced with FIJI implemented filters, correcting noise using the
850 Gaussian blur option and pixel width set to 1.0. Mean intensities in FRAP have been normalized
851 (1 corresponds to pre-bleach signal intensity in arbitrary units).

857 **AUTHOR CONTRIBUTIONS**

858 P.N.M, conceptualization, project administration, supervision, formal analysis, writing-original
859 draft, funding acquisition, complex identification; C.L., A.M., A.D., F.P., A.P., P.R., L.C.,
860 investigation, formal analysis, data curation; S.B., P.D., Y.J., E.R., E.G., and G.S., methodology;
861 A.D., F.P., and E.G., methodology and establishment of liposome assays, curation; C.L., P.N.M,
862 and A.M., established advanced imaging approaches, visualization. All authors reviewed, edited,
863 and approved the paper.

864 **DECLARATION OF INTERESTS**
865 The authors declare no competing interests.

866 **SUPPLEMENTAL MATERIALS**
867 Supplemental Figures 1-7 (legends below figures)
868 Supplemental Movies 1-4:
869     1. TIRFM of a diffusive cluster following a directional track or non-directional track (part a
870        and b)
871     2. Non-diffusive clusters with low dwelling times

14

872     3. Immobile patches of SFH8 atop short filaments resembling the "beads on a string"
873       localization
874     4. SFH8$^{IDR}$ puncta showing dynamic morphology with frequent splitting, fusion, and
875       interconnections resembling liquid-liquid phase-separated (LLPS) condensates

876  Supplemental Files 1-3

877     1. SFH-like proteins alignments
878     2. IDR region conservation in various SFH-like proteins
879     3. Overall steady-state lipid PM and total composition of various mutants used in this study

880  Supplemental Table 1: oligos used in the study
881  Supplemental Information
882     See below


883  **REFERENCES**

884  Arora, D., Abel, N.B., Liu, C., Van Damme, P., Yperman, K., Eeckhout, D., Vu, L.D., Wang, J.,
885  Tornkvist, A., Impens, F., *et al.* (2020). Establishment of Proximity-Dependent Biotinylation
886  Approaches in Different Plant Model Systems. Plant Cell *32*, 3388-3407.
887  Arvidsson, S., Kwasniewski, M., Riaño-Pachón, D.M., and Mueller-Roeber, B. (2008).
888  QuantPrime – a flexible tool for reliable high-throughput primer design for quantitative PCR. BMC
889  Bioinformatics *9*, 465.
890  Banani, S.F., Lee, H.O., Hyman, A.A., and Rosen, M.K. (2017). Biomolecular condensates:
891  organizers of cellular biochemistry. Nat Rev Mol Cell Biol *18*, 285-298.
892  Bembenek, J.N., White, J.G., and Zheng, Y. (2010). A role for separase in the regulation of RAB-
893  11-positive vesicles at the cleavage furrow and midbody. Curr Biol *20*, 259-264.
894  Bequette, C.J., Hind, S.R., Pulliam, S., Higgins, R., and Stratmann, J.W. (2018). MAP kinases
895  associate with high molecular weight multiprotein complexes. J Exp Bot *69*, 643-654.
896  Carlini, L., Brittingham, G.P., Holt, L.J., and Kapoor, T.M. (2020). Microtubules Enhance
897  Mesoscale Effective Diffusivity in the Crowded Metaphase Cytoplasm. Dev Cell *54*, 574-582
898  e574.
899  Chang, H.Y., Smertenko, A.P., Igarashi, H., Dixon, D.P., and Hussey, P.J. (2005). Dynamic
900  interaction of NtMAP65-1a with microtubules in vivo. J Cell Sci *118*, 3195-3201.
901  Clough, S.J., and Bent, A.F. (1998). Floral dip: a simplified method for Agrobacterium -mediated
902  transformation of Arabidopsis thaliana. The Plant Journal *16*, 735-743.
903  Cuevas-Velazquez, C.L., Vellosillo, T., Guadalupe, K., Schmidt, H.B., Yu, F., Moses, D., Brophy,
904  J.A., Cosio-Acosta, D., Das, A., Wang, L., *et al.* (2021). Intrinsically disordered protein biosensor
905  tracks the physical-chemical effects of osmotic stress on cells. bioRxiv, 2021.2002.2017.431712.
906  Deli, A., Tympa, L.E., and Moschou, P.N. (2022). Analyses of Protein Turnover at the Cell Plate
907  by Fluorescence Recovery After Photobleaching During Cytokinesis. Methods Mol Biol *2382*, 233-
908  243.
909  Earnest, J.T., Hantak, M.P., Park, J.-E., and Gallagher, T. (2015). Coronavirus and influenza virus
910  proteolytic priming takes place in tetraspanin-enriched membrane microdomains. J Virol *89*, 6093-
911  6104.
912  Felsenstein, J. (1985). Confidence-Limits on Phylogenies - an Approach Using the Bootstrap.
913  Evolution *39*, 783-791.
914  French, A.P., Mills, S., Swarup, R., Bennett, M.J., and Pridmore, T.P. (2008). Colocalization of
915  fluorescent markers in confocal microscope images of plant cells. Nat Protoc *3*, 619-628.
916  Friml, J., Yang, X., Michniewicz, M., Weijers, D., Quint, A., Tietz, O., Benjamins, R., Ouwerkerk,
917  P.B., Ljung, K., Sandberg, G., *et al.* (2004). A PINOID-dependent binary switch in apical-basal
918  PIN polar targeting directs auxin efflux. Science *306*, 862-865.

919  Gasulla, F., vom Dorp, K., Dombrink, I., Zähringer, U., Gisch, N., Dörmann, P., and Bartels, D.
920  (2013). The role of lipid metabolism in the acquisition of desiccation tolerance in Craterostigma
921  plantagineum: a comparative approach. The Plant Journal *75*, 726-741.
922  Geldner, N., Denervaud-Tendon, V., Hyman, D.L., Mayer, U., Stierhof, Y.D., and Chory, J. (2009).
923  Rapid, combinatorial analysis of membrane compartments in intact plants with a multicolor marker
924  set. Plant J *59*, 169-178.
925  Grefen, C., and Blatt, M.R. (2012). A 2in1 cloning system enables ratiometric bimolecular
926  fluorescence complementation (rBiFC). BioTechniques *53*, 311-314.
927  Gutierrez-Beltran, E., Bozhkov, P.V., and Moschou, P.N. (2015). Tudor Staphylococcal Nuclease
928  plays two antagonistic roles in RNA metabolism under stress. Plant Signal Behav *10*, e1071005.
929  Hellmuth, S., and Stemmann, O. (2020). Separase-triggered apoptosis enforces minimal length
930  of mitosis. Nature.
931  Hertle, A.P., García-Cerdán, J.G., Armbruster, U., Shih, R., Lee, J.J., Wong, W., and Niyogi, K.K.
932  (2020). A Sec14 domain protein is required for photoautotrophic growth and chloroplast vesicle
933  formation in <em>Arabidopsis thaliana</em>. Proceedings of the National Academy of Sciences
934  *117*, 9101-9111.
935  Houbaert, A., Zhang, C., Tiwari, M., Wang, K., de Marcos Serrano, A., Savatin, D.V., Urs, M.J.,
936  Zhiponova, M.K., Gudesblat, G.E., Vanhoutte, I.*, et al.* (2018). POLAR-guided signalling complex
937  assembly and localization drive asymmetric cell division. Nature *563*, 574-578.
938  Hu, G., Katuwawala, A., Wang, K., Wu, Z., Ghadermarzi, S., Gao, J., and Kurgan, L. (2021).
939  flDPnn: Accurate intrinsic disorder prediction with putative propensities of disorder functions. Nat
940  Commun *12*, 4438.
941  Jaillais, Y., Fobis-Loisy, I., Miege, C., Rollin, C., and Gaude, T. (2006). AtSNX1 defines an
942  endosome for auxin-carrier trafficking in Arabidopsis. Nature *443*, 106-109.
943  Jarsch, I.K., Konrad, S.S.A., Stratil, T.F., Urbanus, S.L., Szymanski, W., Braun, P., Braun, K.-H.,
944  and Ott, T. (2014). Plasma Membranes Are Subcompartmentalized into a Plethora of Coexisting
945  and Diverse Microdomains in <em>Arabidopsis</em> and <em>Nicotiana benthamiana</em>.
946  The Plant Cell Online.
947  Jeong, Y.Y., Lee, H.-Y., Kim, S.W., Noh, Y.-S., and Seo, P.J. (2021). Optimization of protoplast
948  regeneration in the model plant Arabidopsis thaliana. Plant Methods *17*, 21.
949  Julkowska, M.M., Rankenberg, J.M., and Testerink, C. (2013). Liposome-Binding Assays to
950  Assess Specificity and Affinity of Phospholipid–Protein Interactions. In Plant Lipid Signaling
951  Protocols, T. Munnik, and I. Heilmann, eds. (Totowa, NJ: Humana Press), pp. 261-271.
952  Kf de Campos, M., and Schaaf, G. (2017). The regulation of cell polarity by lipid transfer proteins
953  of the SEC14 family. Current opinion in plant biology *40*, 158-168.
954  Konopka, C.A., Backues, S.K., and Bednarek, S.Y. (2008). Dynamics of Arabidopsis dynamin-
955  related protein 1C and a clathrin light chain at the plasma membrane. Plant Cell *20*, 1363-1380.
956  Kroschwald, S., Maharana, S., and Simon, A. (2017). Hexanediol: a chemical probe to investigate
957  the material properties of membrane-less compartments. Matters, 2297-8240.
958  Kumar, S., Stecher, G., Li, M., Knyaz, C., and Tamura, K. (2018). MEGA X: Molecular
959  Evolutionary Genetics Analysis across Computing Platforms. Mol Biol Evol *35*, 1547-1549.
960  Liao, C.-Y., Smet, W., Brunoud, G., Yoshida, S., Vernoux, T., and Weijers, D. (2015). Reporters
961  for sensitive and quantitative measurement of auxin response. Nature methods *12*, 207-210.
962  Lin, W., Zhou, X., Tang, W., Takahashi, K., Pan, X., Dai, J., Ren, H., Zhu, X., Pan, S., Zheng, H.*,
963  et al.* (2021). TMK-based cell-surface auxin signalling activates cell-wall acidification. Nature *599*,
964  278-282.
965  Liu, C., and Moschou, P.N. (2018). Cutting in the middleman: hidden substrates at the interface
966  between proteases and plant development. New Phytol *218*, 916-922.
967  Liu, C., Stael, S., Gevaert, K., Van Breusegem, F., Bozhkov, P.V., and Moschou, P.N. (2017).
968  The Proteolytic Landscape of an Arabidopsis Separase-Deficient Mutant Reveals Novel
969  Substrates Associated With Plant Development. bioRxiv, 140962.

970 Liu, C., Tornkvist, A., Charova, S., Stael, S., and Moschou, P.N. (2020). Proteolytic Proteoforms:
971 Elusive Components of Hormonal Pathways? Trends Plant Sci *25*, 325-328.
972 Ma, S., Quist, T.M., Ulanov, A., Joly, R., and Bohnert, H.J. (2004). Loss of TIP1;1 aquaporin in
973 Arabidopsis leads to cell and plant death. Plant J *40*, 845-859.
974 Maier, R., Brandner, C., Hintner, H., Bauer, J., and Onder, K. (2008). Construction of a reading
975 frame-independent yeast two-hybrid vector system for site-specific recombinational cloning and
976 protein interaction screening. BioTechniques *45*, 235-244.
977 Marhava, P., Aliaga Fandino, A.C., Koh, S.W.H., Jelinkova, A., Kolb, M., Janacek, D.P., Breda,
978 A.S., Cattaneo, P., Hammes, U.Z., Petrasek, J.*, et al.* (2019). Plasma Membrane Domain
979 Patterning and Self-Reinforcing Polarity in Arabidopsis. Dev Cell.
980 Mateos-Gil, P., Tsortos, A., Vélez, M., and Gizeli, E. (2016). Monitoring structural changes in
981 intrinsically disordered proteins using QCM-D: application to the bacterial cell division protein
982 ZipA. Chem Commun (Camb) *52*, 6541-6544.
983 Milioni, D., Mateos-Gil, P., Papadakis, G., Tsortos, A., Sarlidou, O., and Gizeli, E. (2020). Acoustic
984 Methodology for Selecting Highly Dissipative Probes for Ultrasensitive DNA Detection. Anal Chem
985 *92*, 8186-8193.
986 Milovanovic, D., Wu, Y., Bian, X., and De Camilli, P. (2018). A liquid phase of synapsin and lipid
987 vesicles. Science *361*, 604-607.
988 Minina, E.A., Reza, S.H., Gutierrez-Beltran, E., Elander, P.H., Bozhkov, P.V., and Moschou, P.N.
989 (2017). The Arabidopsis homolog of Scc4/MAU2 is essential for embryogenesis. J Cell Sci *130*,
990 1051-1063.
991 Moschou, P.N., Gutierrez-Beltran, E., Bozhkov, P.V., and Smertenko, A. (2016). Separase
992 Promotes Microtubule Polymerization by Activating CENP-E-Related Kinesin Kin7. Dev Cell *37*,
993 350-361.
994 Moschou, P.N., Smertenko, A.P., Minina, E.A., Fukada, K., Savenkov, E.I., Robert, S., Hussey,
995 P.J., and Bozhkov, P.V. (2013). The caspase-related protease separase (extra spindle poles)
996 regulates cell polarity and cytokinesis in Arabidopsis. Plant Cell *25*, 2171-2186.
997 Pak, C.W., Kosno, M., Holehouse, A.S., Padrick, S.B., Mittal, A., Ali, R., Yunus, A.A., Liu, D.R.,
998 Pappu, R.V., and Rosen, M.K. (2016). Sequence Determinants of Intracellular Phase Separation
999 by Complex Coacervation of a Disordered Protein. Mol Cell *63*, 72-85.
1000 Pan, X., Fang, L., Liu, J., Senay-Aras, B., Lin, W., Zheng, S., Zhang, T., Guo, J., Manor, U., Van
1001 Norman, J.*, et al.* (2020). Auxin-induced signaling protein nanoclustering contributes to cell
1002 polarity formation. Nat Commun *11*, 3914.
1003 Paponov, I.A., Friz, T., Budnyk, V., Teale, W., Wüst, F., Paponov, M., Al-Babili, S., and Palme, K.
1004 (2019). Natural Auxin Does Not Inhibit Brefeldin A Induced PIN1 and PIN2 Internalization in Root
1005 Cells. Frontiers in plant science *10*.
1006 Peruzzi, J.A., Jacobs, M.L., Vu, T.Q., Wang, K.S., and Kamat, N.P. (2019). Barcoding Biological
1007 Reactions with DNA-Functionalized Vesicles. Angew Chem Int Ed Engl *58*, 18683-18690.
1008 Platre, M.P., Bayle, V., Armengot, L., Bareille, J., Marques-Bueno, M.D.M., Creff, A., Maneta-
1009 Peyret, L., Fiche, J.B., Nollmann, M., Miege, C.*, et al.* (2019). Developmental control of plant Rho
1010 GTPase nano-organization by the lipid phosphatidylserine. Science *364*, 57-62.
1011 Platre, M.P., Noack, L.C., Doumane, M., Bayle, V., Simon, M.L.A., Maneta-Peyret, L., Fouillen,
1012 L., Stanislas, T., Armengot, L., Pejchar, P.*, et al.* (2018). A Combinatorial Lipid Code Shapes the
1013 Electrostatic Landscape of Plant Endomembranes. Developmental Cell *45*, 465-480.e411.
1014 Powers, S.K., Holehouse, A.S., Korasick, D.A., Schreiber, K.H., Clark, N.M., Jing, H., Emenecker,
1015 R., Han, S., Tycksen, E., Hwang, I.*, et al.* (2019). Nucleo-cytoplasmic Partitioning of ARF Proteins
1016 Controls Auxin Responses in <em>Arabidopsis thaliana</em>. Mol Cell *76*, 177-190.e175.
1017 Pucadyil, T.J., and Schmid, S.L. (2010). Supported bilayers with excess membrane reservoir: a
1018 template for reconstituting membrane budding and fission. Biophys J *99*, 517-525.
1019 Ramachandran, R. (2018). Mitochondrial dynamics: The dynamin superfamily and execution by
1020 collusion. Semin Cell Dev Biol *76*, 201-212.

Rames, M., Yu, Y., and Ren, G. (2014). Optimized negative staining: a high-throughput protocol for examining small and asymmetric protein structure by electron microscopy. Journal of visualized experiments : JoVE, e51087-e51087.

Saitou, N., and Nei, M. (1987). The neighbor-joining method: a new method for reconstructing phylogenetic trees. Mol Biol Evol *4*, 406-425.

Schaaf, G., Ortlund, E.A., Tyeryar, K.R., Mousley, C.J., Ile, K.E., Garrett, T.A., Ren, J., Woolls, M.J., Raetz, C.R., Redinbo, M.R.*, et al.* (2008). Functional anatomy of phospholipid binding and regulation of phosphoinositide homeostasis by proteins of the sec14 superfamily. Mol Cell *29*, 191-206.

Schweighofer, A., Kazanaviciute, V., Scheikl, E., Teige, M., Doczi, R., Hirt, H., Schwanninger, M., Kant, M., Schuurink, R., Mauch, F.*, et al.* (2007). The PP2C-type phosphatase AP2C1, which negatively regulates MPK4 and MPK6, modulates innate immunity, jasmonic acid, and ethylene levels in Arabidopsis. Plant Cell *19*, 2213-2224.

Shin, J., Jeong, G., Park, J.-Y., Kim, H., and Lee, I. (2018). MUN (MERISTEM UNSTRUCTURED), encoding a SPC24 homolog of NDC80 kinetochore complex, affects development through cell division in Arabidopsis thaliana. The Plant Journal *93*, 977-991.

Steinborn, K., Maulbetsch, C., Priester, B., Trautmann, S., Pacher, T., Geiges, B., Kuttner, F., Lepiniec, L., Stierhof, Y.D., Schwarz, H.*, et al.* (2002). The Arabidopsis PILZ group genes encode tubulin-folding cofactor orthologs required for cell division but not cell growth. Gene Dev *16*, 959-971.

Stengel, G., Simonsson, L., Campbell, R.A., and Höök, F. (2008). Determinants for membrane fusion induced by cholesterol-modified DNA zippers. J Phys Chem B *112*, 8264-8274.

Sugiura, T., Takahashi, C., Chuma, Y., Fukuda, M., Yamada, M., Yoshida, U., Nakao, H., Ikeda, K., Khan, D., Nile, A.H.*, et al.* (2019). Biophysical Parameters of the Sec14 Phospholipid Exchange Cycle. Biophys J *116*, 92-103.

Suzuki, A., Badger, B.L., Haase, J., Ohashi, T., Erickson, H.P., Salmon, E.D., and Bloom, K. (2016). How the kinetochore couples microtubule force and centromere stretch to move chromosomes. Nat Cell Biol *18*, 382-392.

Takahashi, Y., Soyano, T., Kosetsu, K., Sasabe, M., and Machida, Y. (2010). HINKEL kinesin, ANP MAPKKKs and MKK6/ANQ MAPKK, which phosphorylates and activates MPK4 MAPK, constitute a pathway that is required for cytokinesis in Arabidopsis thaliana. Plant Cell Physiol *51*, 1766-1776.

Tang, T., Bidon, M., Jaimes, J.A., Whittaker, G.R., and Daniel, S. (2020). Coronavirus membrane fusion mechanism offers a potential target for antiviral development. Antivir Res *178*, 104792.

Teale, W.D., Pasternak, T., Dal Bosco, C., Dovzhenko, A., Kratzat, K., Bildl, W., Schworer, M., Falk, T., Ruperti, B., Schaefer, J.V.*, et al.* (2021). Flavonol-mediated stabilization of PIN efflux complexes regulates polar auxin transport. Embo J *40*, e104416.

Vernon, R.M., and Forman-Kay, J.D. (2019). First-generation predictors of biological protein phase separation. Curr Opin Struct Biol *58*, 88-96.

Vincent, P., Chua, M., Nogue, F., Fairbrother, A., Mekeel, H., Xu, Y., Allen, N., Bibikova, T.N., Gilroy, S., and Bankaitis, V.A. (2005). A Sec14p-nodulin domain phosphatidylinositol transfer protein polarizes membrane growth of Arabidopsis thaliana root hairs. J Cell Biol *168*, 801-812.

Wewer, V., Brands, M., and Dörmann, P. (2014). Fatty acid synthesis and lipid metabolism in the obligate biotrophic fungus Rhizophagus irregularis during mycorrhization of Lotus japonicus. The Plant Journal *79*, 398-412.

Wiedemeier, A.M.D., Judy-March, J.E., Hocart, C.H., Wasteneys, G.O., Williamson, R.E., and Baskin, T.I. (2002). Mutant alleles of Arabidopsis RADIALLY SWOLLEN 4 and 7 reduce growth anisotropy without altering the transverse orientation of cortical microtubules or cellulose microfibrils. Development *129*, 4821-4830.

Xiong, B. (2011). Spc25: How the kinetochore protein plays during oocyte meiosis. Cell Cycle *10*, 1031-1030.

1072    Xu, J., Lee, Y.J., and Liu, B. (2020). Establishment of a mitotic model system by transient
1073    expression of the D-type cyclin in differentiated leaf cells of tobacco (Nicotiana benthamiana).
1074    New Phytol *226*, 1213-1220.
1075    Xu, J., and Scheres, B. (2005). Dissection of Arabidopsis ADP-RIBOSYLATION FACTOR 1
1076    function in epidermal cell polarity. Plant Cell *17*, 525-536.
1077    Yin, K., Ueda, M., Takagi, H., Kajihara, T., Sugamata Aki, S., Nobusawa, T., Umeda-Hara, C.,
1078    and Umeda, M. (2014). A dual-color marker system for in vivo visualization of cell cycle
1079    progression in Arabidopsis.  *80*, 541-552.
1080    Zuckerkandl, E., and Pauling, L. (1965). Evolutionary Divergence and Convergence in Proteins.
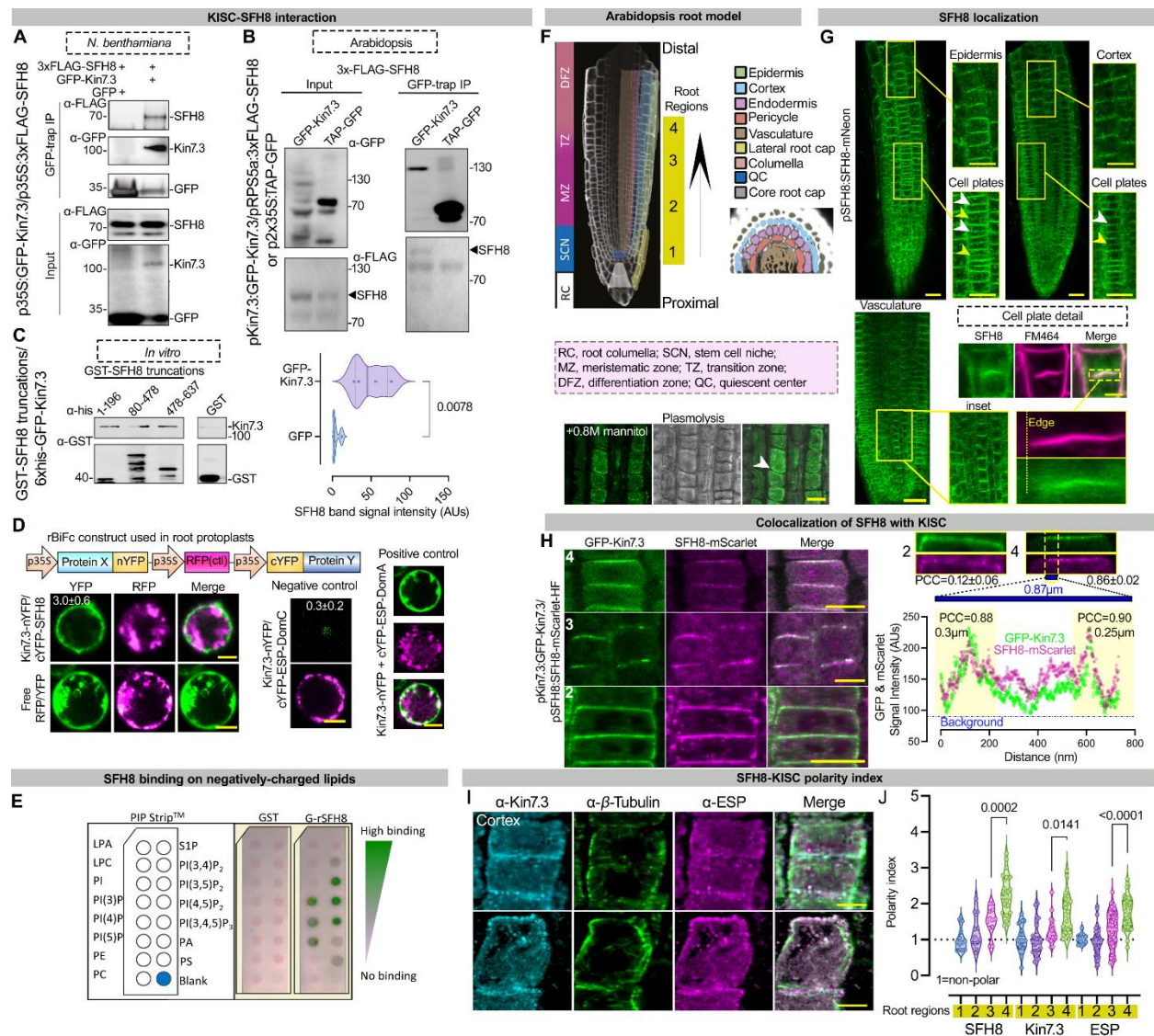1081    In Evolving Genes and Proteins, V. Bryson, and H.J. Vogel, eds. (Academic Press), pp. 97-166.
1082

**Figure 1. KISC and the lipid-binding protein SFH8 associate at the PM.**

**A.** Kin7.3/SFH8 co-immunoprecipitation from *N. benthamiana*. Free-GFP was also present in the GFP-Kin7.3 samples, due to non-specific cleavage. WBs were replicated three times.

**B.** Kin7.3/SFH8 co-immunoprecipitation from Arabidopsis (5 days after germination (DAG)); quantification of the interaction (chart; n=4, 2-tailed *t*-test).

**C.** GST pull-down assays of SFH8 truncated forms with 6xhis-GFP-Kin7.3 (**S1K:** protein purification). WBs were replicated three times.

**D.** rBiFC assays showing Kin7.3/SFH8 interaction at the PM in Arabidopsis root protoplasts. Controls: Kin7.3-nYFP with ESP-DomA or -DomC (Moschou et al., 2016). Mean YFP/RFP signal ratios±SD (n=20) indicated on images. Scale bars, 6 μm.

**E.** GST-SFH8 lipid binding specificity on protein-lipid blot overlay. A representative blot is shown replicated twice.

**F.** Root micrograph showing the "4 root regions" examined herein. Vertical arrow: proximodistal axis.

**G.** SFH8-mNeon tissue-specific expression and subcellular localization. Numbers denote root regions according to the root model in **F**. White and yellow arrowheads: mature and expanding

1100  cell plates, respectively. Plasmolysis experiment: confirmation of SFH8 signal exclusion from the
1101  cell wall (white arrowhead; root region 2). Scale bars, 20 µm (5 µm for cell plate detail
1102  counterstained with FM4-64). Note the lack of SFH8 signal from the leading edge (denoted by the
1103  vertical yellow line.
1104  **H.**  Kin7.3/SFH8 localization at regions 2-4. Scale bars, 10 µm. Right top: high-resolution signal
1105  of Kin7.3/SFH8 at the PM (regions 2 and 4). For region 4, plot profile of signal intensity across a
1106  straight line of 0.87 µm (lower). The colocalization analyses using Pearson Correlation Coefficient
1107  (PCC) is also shown at the indicated regions of interest (ROIs; rectangular of ~0.3 µm). The
1108  overall PCC values for regions 2 and 4 are also shown (ROIs: whole image). AUs, arbitrary units
1109  (five independent experiments from 3 adjacent cells±SD; n=15).
1110  **I.**  Example of α-ESP/α-Kin7.3 colocalization and polarization (counterstained with α-$\beta$-tubulin;
1111  region 3). Scale bars, 5 µm.
1112  **J.**  Quantification of SFH8 (data derived from **G**), Kin7.3, and ESP polarity in the 4 regions (values
1113  >1 represent polarized proteins and calculations are described in **Figure S1A**; five independent
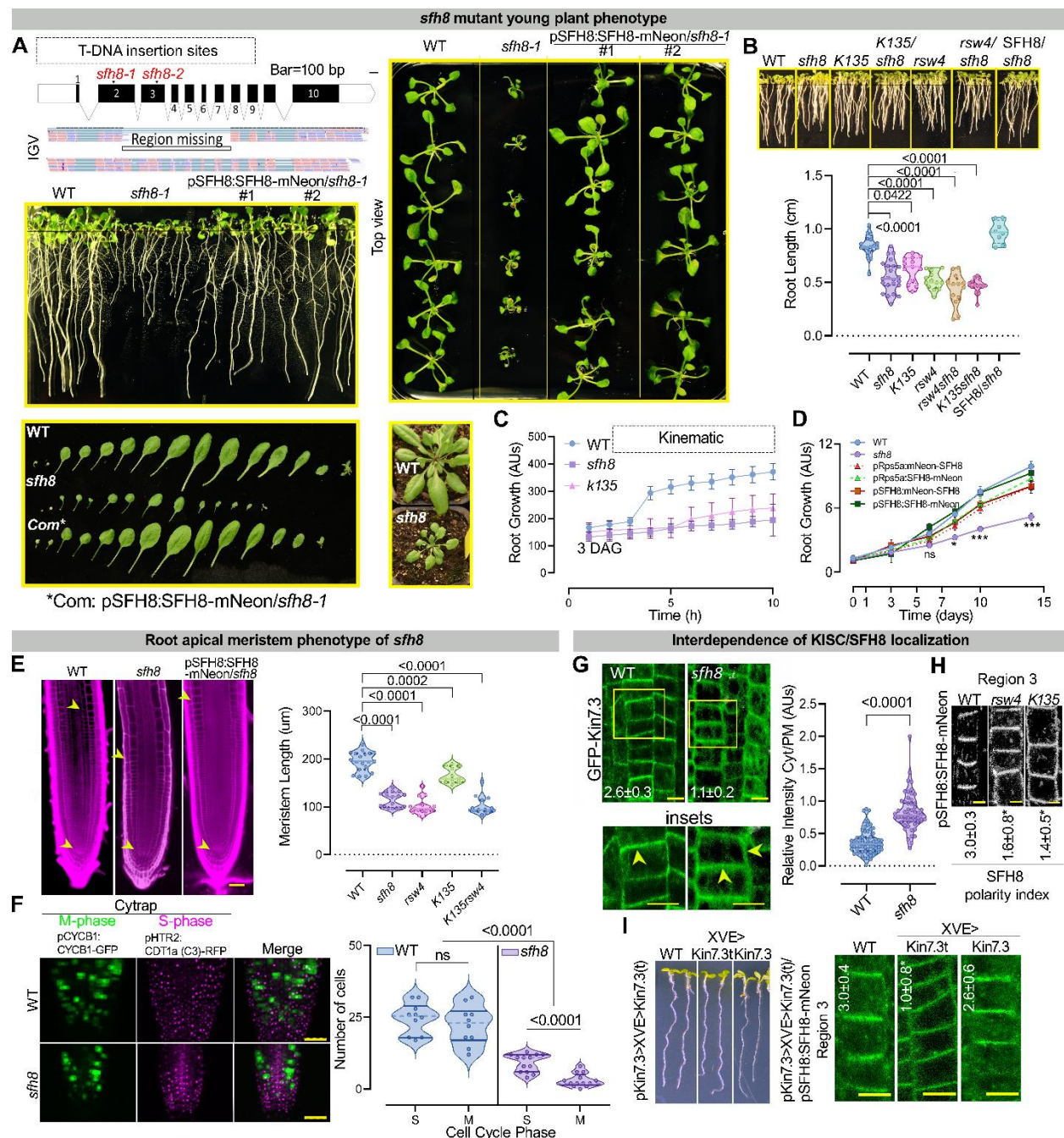1114  experiments; n≥25, Dunnett).
1115

21

**Figure 2. SFH8 modulates early development cooperatively with KISC.**

**A.** T-DNA insertion sites for *sfh8-1* and *-2*, RNAseq IGV representation of deleted exons in *sfh8-1*, and phenotypes of young WT, *sfh8-1,* and complementation lines (10 DAG on plates or one-month-old).

**B.-D.** Root length of various mutants (7 DAG) (**B**), and kinematic root growth quantification using "SPIRO" (see **STAR METHODS**; 3 DAG=time 0; at least five measurements (n≥25; 1-sided Dunnett); **C**), or in a time-frame of days (**D**). Asterisks indicate statistical significance (*, 0.05; ***, <0.001; ns, no significant: WT vs. *sfh8*).

**E.** Root meristem micrographs (5 DAG; propidium iodide staining); quantifications of WT, *sfh8*, or KISC mutants meristem sizes (n=19; ordinary ANOVA). Scale bars, 50 µm.

1

1127   **F.** Micrograph of the "Cycle Tracking in Plants" marker (CyTRAP) in WT and *sfh8* (7 DAG);
1128   quantification of S and M phase (three independent experiments, n=5 in each; paired *t*-test). Scale
1129   bars, 50 μm.
1130   **G.** GFP-Kin7.3 PM localization in WT or *sfh8* (5 DAG, region 3). The polarity index of Kin7.3 is
1131   also shown on the images (three pooled experiments from region 3±SD; n=40; differences were
1132   significant at p<0.0001, Dunnett). Scale bars, 5 μm; quantification of cytoplasmic to PM signal
1133   (right; a single representative experiment replicated multiple times; n=25; 2-tailed *t*-test).
1134   Arrowheads in the insets show apical or lateral localization of Kin7.3.
1135   **H.** SFH8-mNeon localization in WT, *rsw4*, and *K135* (5 DAG, region 3). Images are representative
1136   of an experiment replicated multiple times for polarity. The polarity index of SFH8 is also shown
1137   (three pooled experiments from region 3±SD; n=40; "*": p<0.0001 to WT, Dunnett). Scale bars, 5
1138   μm.
1139   **I.** Perturbed gravitropism and growth of lines over-expressing transiently Kin7.3 tail ("t"; 24 h, 2
1140   μM estradiol). Scale bars, 8 μm. Right: SFH8 polarity loss in Kin7.3t lines (region 3, epidermal
1141   cells). Images are representative of an experiment replicated multiple times for polarity. Scale
1142   bars, 10 μm. SFH8 polarity index is also shown on the images (three pooled experiments from
1143   region 3±SD; n=40; "*": p<0.0001 to WT, Dunnett).
1144
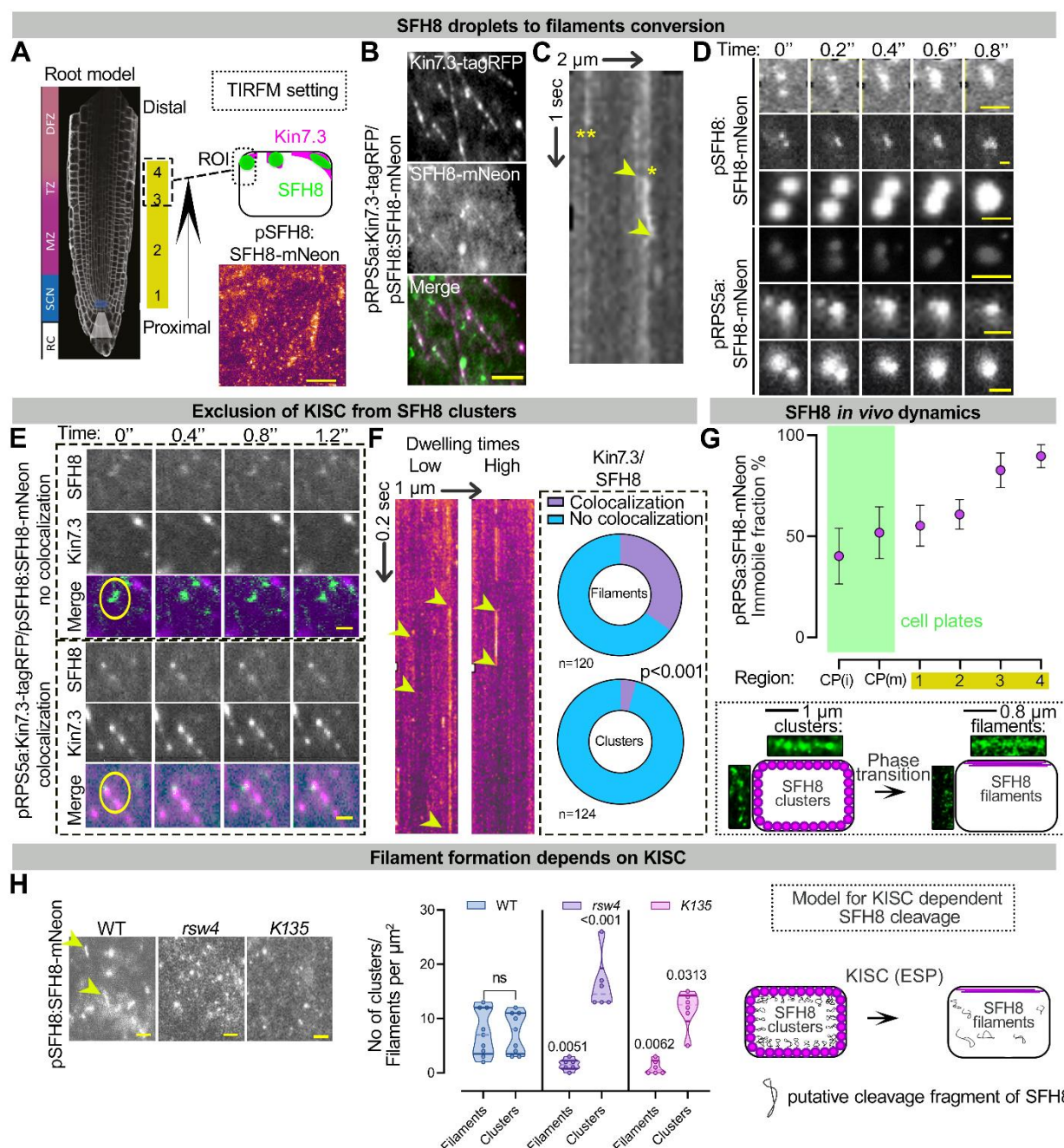
**Figure 3. SFH8 polarization depends on a droplet-to-filamentous transition.**

**A.** Model showing the region used for imaging in TIRFM, and an SFH8 localization overview (5 DAG, region 3). Scale bar, 2 µm.

**B.** Dual-channel TIRFM of SFH8-mNeon/Kin7.3-RFP. Scale bar, 0.3 µm.

**C.** Kymograph showing diffusing (*) and non-diffusing (**) clusters. Arrowheads indicate the offset of the diffusing cluster (~200 nm).

**D.** Examples of SFH8-mNeon clusters fusing on the PM. Scale bar, 0.3 µm.

**E.** Dual-channel TIRFM of SFH8-mNeon/Kin7.3-RFP co-expressing line showing SFH8 clusters and filaments. Note the lateral diffusion of SFH8 clusters and the lack of filaments motility (circles). Scale bars, 0.3 µm.

1

1156 **F.** Kymographs show diffusing clusters with low and high dwelling times at the PM. Right: charts
1157 show Kin7.3/SFH8 colocalization percentage in clusters or filaments (three pooled experiments;
1158 5 fields of view, n, as indicated; Wilcoxon).
1159 **G.** SFH8-mNeon immobilization along the proximodistal meristem root axis determined by FRAP.
1160 Data are means ± SD from a single representative experiment with 10 roots at each point (n=10).
1161 CPi, immature cell plate; CPm, mature cell plate. Bottom: clusters and filaments in two root
1162 regions determined by super-resolution (120 nm, 40 frame per second) midsection confocal
1163 microscopy (regions 1 and 4, left and right, respectively) and a model showing the SFH8 clusters-
1164 to-filaments conversion.
1165 **H.** SFH8-mNeon localization in WT, *K135,* and *rsw4* root cells (5 DAG, region 3, TIRFM;
1166 arrowheads indicate filaments). Scale bar, 0.5 µm; quantification of SFH8-mNeon clusters and
1167 filaments in WT, *K135,* and *rsw4* (right; n=28, 5 fields of view; Wilcoxon) and a model showing
1168 the dependency of SFH8 clusters-to-filaments conversion on KISC.
1169

**SFH8 is cleaved in vivo**

**A** pRPS5a:HF-mScarlet-SFH8

**B** pSFH8: mNeon-SFH8 / SFH8-mNeon

**C** "Cleavage biosensor" pRPS5a:HF-mScarlet-SFH8-mNeon

**SFH8 cleavage at the N-terminal IDR**

**D** φEXXRX / IDR / CRAL-TRIO / Nodulin / Polybasic patch (6K) / SFH8IDR / SFH8ΔIDR

**E** Relative MS/MS Quantity — VSSVSIEDVR 7.89e-09 / VSSVSIEDVRDVEELQ 2.62e-09

Cleavage position P1' / P1
-- ADQYAPIVIEDVRDEEEE SFH6
KSDGRVSSVSIEDVRDVEEL SFH8
KSDVRVSSVSIEDVRDVEEL SFH9

**F** PONDR score / Propensity score

**N-terminal IDR promotes phase separation of SFH8**

**G** IDR swap — SFH8 / SFH6 / SFH6IDRSFH8

**H** PM Cluster (-ESP) — SFH8 / SFH6 / SFH6IDRSFH8

**I** mScarlet-SFH8-mNeon / mScarlet-SFH8R84A-mNeon

**J** PLD condensators — ARF19-PLD / TDP43 / FUS / SFH6 / SFH8 / SFH9 / SFH61-69 / SFH8502-538 / SFH820-71 / SFH919-58 — %total aa

**SFH8 cleavage and polarity**

**K** pSFH8:mNeon-SFH8 — WT / K135 / rsw4 — Polarity indexes 2.8±0.3 / 1.2±0.6 / 1.1±0.3 ***

**L** sfh8 / pRPS5a:mNeon-SFH8R84A — WT / sfh8 / pRPS5a:mNeon-SFH8 / #1 #2 #3

**M** Midplane confocal — pRPS5a:mNeon-SFH8 / pRPS5a:mNeon-SFH8R84A — TIRFM SFH8 / SFH8R84A

65.00±3.45 / 15.38±1.62 — Filaments / Clusters — WT n=25 / R84A n=111 p<0.001
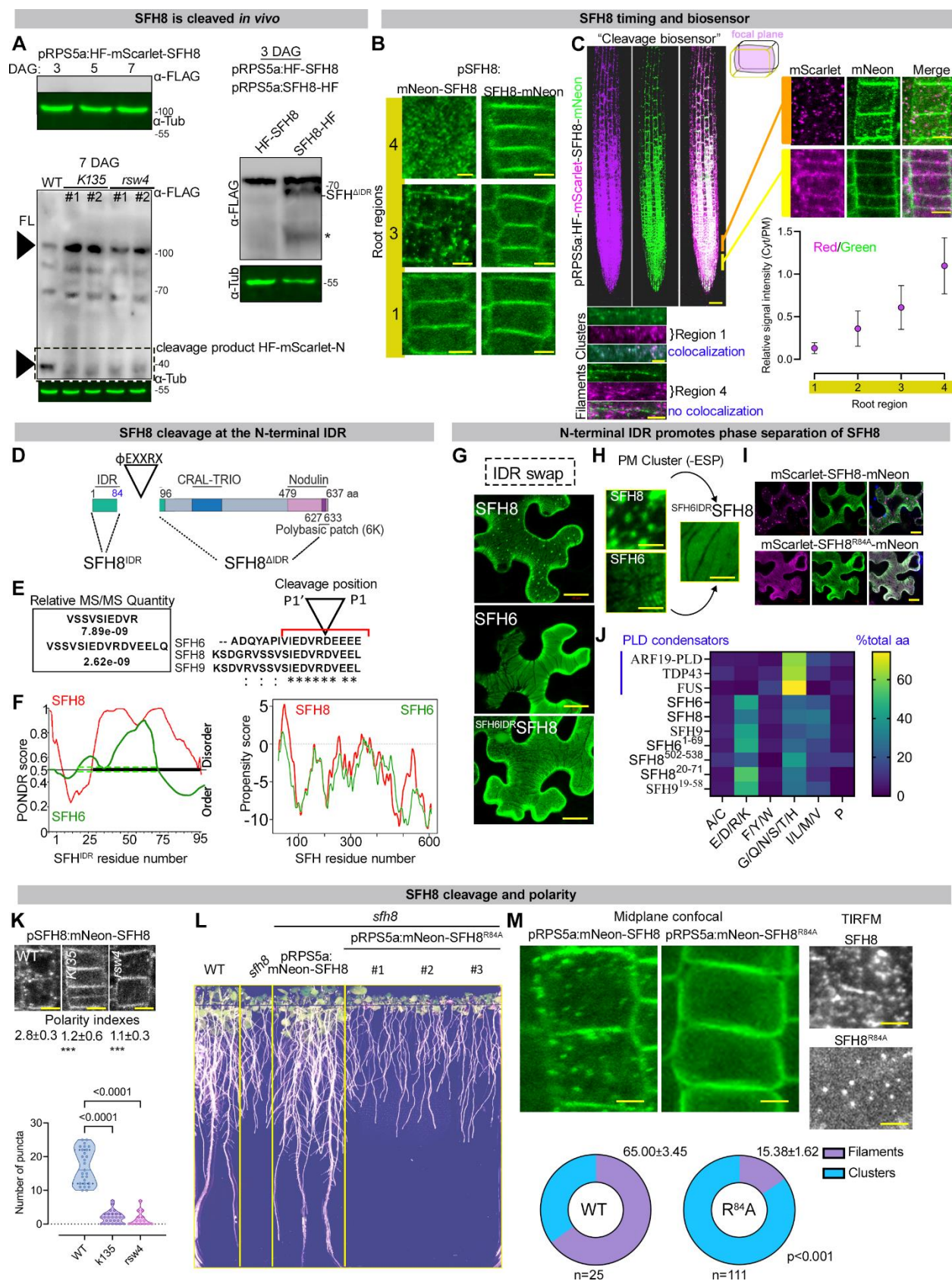
1170

1

**Figure 4. ESP cleaves SFH8 to promote SFH8 droplet-to-filamentous transition.**

**A.** WB showing the reduction of SFH8 full-length levels from 3 to 7 DAG (upper left). Lower left: cleavage and release of an N-terminal fragment (black arrowhead at ~40 kDa; FL, full-length) in WT, *K135,* or *rsw4* (24 h at the restrictive temperature 28°C, two lines; lower). Right: WB showing the remaining C-terminal SFH8 fragment (asterisk, an additional truncated product of low abundance). WBs are representative of experiments replicated multiple times.

**B.** Micrographs of the SFH8 N- or C-terminally tagged with mNeon (3 regions, epidermis; 4th region slightly below the transition zone in this case). Scale bars, 4 μm.

**C.** SFH8 cleavage biosensor expression (scale bar, 50 μm), details (right, mid-plane focus, scale bars, 4 μm), and relative signal intensity of cytoplasmic versus PM signal (chart). Data are means ± SD (n=10). Bottom: super-resolution imaging (120 nm) of cluster-to-filament conversion (regions 2 to 4). Note the absence of mScarlet signal from filaments.

**D.** SFH8 protein architecture (IDR, intrinsically disordered region, CRAL-TRIO, and NOD: nodulin motif; see also **Figure S1H** for annotations).

**E.** SFH8 IDR peptides identified in pRPS5a:SFH8-mScarlet-HF pull-down experiments coupled with LC-MS/MS. The cleavage motif of ESP on SFH proteins, φEXXR is conserved (presented here for three SFH protein paralogs, SFH6/8/9; upper left).

**F.** *In silico* predictions of IDRs by PONDR, and phase separation propensity determined by catGRANULE (Vernon and Forman-Kay, 2019) for SFH8 and SFH6. Note the shorter IDR length and lower LLPS propensity score for SFH6.

**G.** IDR defines the phase separation properties of SFH8. Reduced puncta formation in a chimeric protein of SFH6$^{IDR}$ and the C-terminal SFH8 in *N. benthamiana* leaves, in the presence of ESP/CyclinD; see also **Figure S4**). Scale bars, 20 μm.

**H.** Similar experiment as in **G**, in the absence of ESP. Note the increased clustering of SFH8 and the lack of clusters in an $^{SFH6IDR}$SFH8 chimera. Scale bars, 2 μm.

**I.** Lack of SFH8$^{R84A}$ mutant cleavage in *N. benthamiana* leaves in the presence of ESP/CyclinD. Scale bars, 20 μm.

**J.** Comparative analysis of the SFH8 IDR composition. Each amino acid is assigned to one of six groups on the x-axis, and the fraction of grouped amino acids is shown. For comparison, model "condensators" are shown (ARF19 to FUS). SFH8 IDR is similar to the average IDR signature of disordered proteins in Arabidopsis (Powers et al., 2019). The lengths of the IDRs were determined by the flDPnn (Hu et al., 2021).

**K.** Dependency of KISC for SFH8 polarity and cleavage. Reduced puncta formation and increased mNeon-SFH8 PM signal in the *K135* or *sfh8* (7 DAG, region 3). Scale bars, 5 μm. Lower: puncta quantification (single representative experiment; n=27 cells from region 3; ANOVA). Polarity indexes of SFH8-mNeon are also shown ("***": p<0.0001 to WT, Dunnett).

**L.** Reduction of *sfh8* complementation by mNeon-SFH8$^{R84A}$. Three-individual lines are shown.

**M.** Localization of SFH8$^{R84A}$. Scale bars, 2 μm. Right: persistence of PM SFH8 condensates in *SFH8$^{R84A}$/sfh8* lines (TIRFM; scale bar, 0.2 μm). Bottom: quantification of mNeon-SFH8 or mNeon-SFH8$^{R84A}$ clusters and filaments (four independent experiments; n as indicated, 2-tailed *t*-test).

2

**Figure 5. SFH8 can affect the delivery of polar proteins like PIN2.**

**A.** PIN2-GFP signal intensity (color-coded) in WT and *sfh8* and quantification (right) of PIN2-GFP on PM of WT, *sfh8*, *K135*, and *rsw4* (7 DAG, region 3; two independent experiments; n=164-203, multiple comparisons Dunnett). Scale bars, 50 µm.

3

**B.** PIN2 localization in WT and *sfh8* (color-coded; counterstaining with a-*β*-tubulin to show focal plane; magenta; 5 DAG, region 3). Arrowheads indicate PIN2 accumulation maximum, and in the *sfh8* slight polarity offset. Note the high number of PIN2-positive endosome-like structures in the *sfh8*. The *sfh8* signal intensity was adjusted to normalize signal intensity between *sfh8* and WT. Scale bars, 10 μm. Right: quantification of endosomes above the confocal diffraction limit (~200 nm) in WT and *sfh8* under normal conditions (four independent experiments; n=123, ordinary ANOVA).

**C.** α-PIN2 localization (midsection epidermis and cortex; 7 DAG, region 3) in WT,*sfh8,* and *sfh8* with SFH8$^{R84A}$, or HF-SFH8 ("F"). Yellow arrowheads denote PIN2 polarity. Right: PIN2 polarity index and cells with proper polarity in WT, *sfh8* (expressing also SFH8$^{R84A}$ or HF-SFH8), *K135,* and *rsw4* (for the index: means±SD; four independent experiments; n=10, 1-way ANOVA, "*", p<0.0001; for the number of cells: four independent experiments; n=118, Kruskal-Wallis). Scale bars, 5 μm.

**D.** PIN2-GFP localization in WT and *sfh8* (epidermis and cortex; 7 DAG, region 3) treated with 50 μm BFA (±CHX) for 1 h (left) and after BFA washout for 30 min. CHX was added to a final concentration of 30 μM (1 h pre-treatment and retained throughout the experiment). Right: BFA bodies quantification in WT and *sfh8* (three independent pooled experiments; n=15, 5 fields of view; paired 2-tailed *t*-test between WT/SFH8 in the presence of BFA). Scale bars, 5 μm.

**E.** FRAP micrographs from polarized PIN2 (region 3) in WT and *sfh8*. Note the offset of PIN2 polarity (yellow arrowheads) in *sfh8*. The rectangular denotes the bleached region of interest (ROI). Scale bars, 3 μm.

**F.** FRAP PIN2 signal recovery (normalized integrated density). Data are means ± SD of three independent pooled experiments (n=15). The red faded band parallel to the Y-axis indicates laser iterations time. Numbers next to the genotype, denote recovery half-time±SD (n=15, paired 2-tailed *t*-test).

**G.** Representative images of co-localization of N- or C-terminally- tagged SFH8-mScarlet and HF-Kin7.3-RFP with PIN2-GFP in regions 1-4. Scale bars, 5 μm.

**H.** PCC colocalization quantifications between PIN2 and SFH8 or Kin7.3 (apicobasal or lateral domains, for Kin7.3; three independent pooled experiments; n=36, nested 1-way ANOVA, p<0.05, *; p<0.001, **; p<0.0001, ***, compared to region 1).

**I.** Polarity index for SFH8, Kin7.3, and PIN2 in 3 root regions (see also **Figure 1**; three independent pooled experiments; n=36, nested 1-way ANOVA).

**J.** High speed (40 frames per second) and super-resolution (120 nm) confocal images with insets showing details of HF-mScarlet-SFH8 cluster/PIN2 exclusion. Note that the two proteins colocalized in non-clustered PM domains (see also **Figure 6** and corresponding text). PCC values represent colocalization analyses between filamentous patches of Kin7.3 or SFH8 with PIN2, while clusters of SFH8 (region 2: to observe the signal at the PM) showed anti-correlation (denoted also by the arrowhead). PCC±SD values are from three independent pooled experiments (n=120).
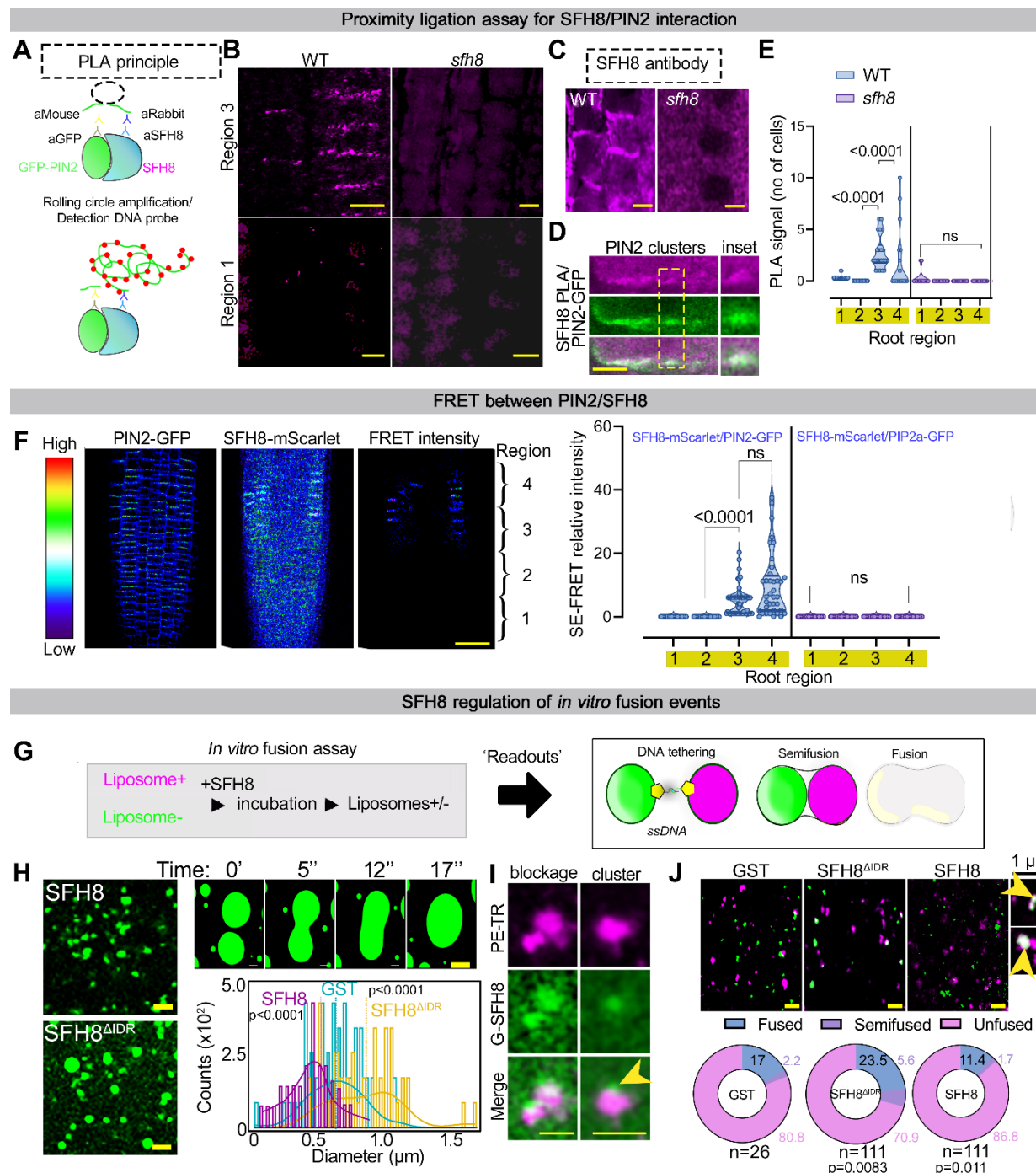
1258

**Figure 6. Removal of the SFH8 IDR promotes interaction with PIN2 and membrane fusion.**

**A.** Proximity ligation (PLA) principle.

**B.** PLA-positive signal (resembling puncta) produced by α-SFH8/α-GFP in pPIN2:PIN2-GFP in WT or *sfh8*. Scale bars, 5 μm.

**C.** Micrographs showing α-SFH8 signal in WT ("*sfh8*" is a negative control). Scale bars, 5 μm.

**D.** Details of PLA-positive PIN2/SFH8 signal puncta at the PM. Scale bar, 1 μm.

**E.** Quantification of PLA-positive cells in 4 regions (five independent experiments; n=20, nested 1-way ANOVA).

1

**F.** Sensitized emission (SE)-FRET efficiency between PIN2-GFP (pPIN2) and SFH8-mScarlet (pRPS5a). Scale bar, 50 µm. Right: signal quantification of SE-FRET between the indicated combinations (five independent experiments; n=50, paired 2-tailed $t$-test).

**G.** Pipeline of the DNA-zippers approach to test membrane fusion.

**H.** DNA-zipper assay with GST-SFH8$^{\Delta IDR}$ or -SFH8 (full length; lumen labeled with fluorescein only). The enlarged micrographs (top) show a time series of the tethering/fusion of two liposomes that converted to GUVs due to SFH8$^{\Delta IDR}$. Quantifications of fusions are also shown (three pooled independent experiments, with n=225; means indicated with vertical lines; Wilcoxon). Scale bars, 2 µm.

**I.** Fusion blockage by fluorescently-labeled SFH8 clusters on liposomes (stained with PE-texas red (magenta). Arrowhead denotes an SFH8 cluster formed atop the labeled liposome (images after deconvolution in a super-resolution setting with 120 nm resolution). Scale bars, 2 µm.

**J.** Liposome content mixing with lumen stained with fluorescein (green), and lipids stained with PE-texas red (magenta). Scale bars, 2 µm. Insets show a hemifusion event (upper), and a combination of hemifusion with a tethered LUV (lower inset). The arrows show content mixing (pseudocolored white). Lower: distribution (%) of LUVs among different treatments (three pooled independent experiments; n as indicated, Dunnett for "fusion").
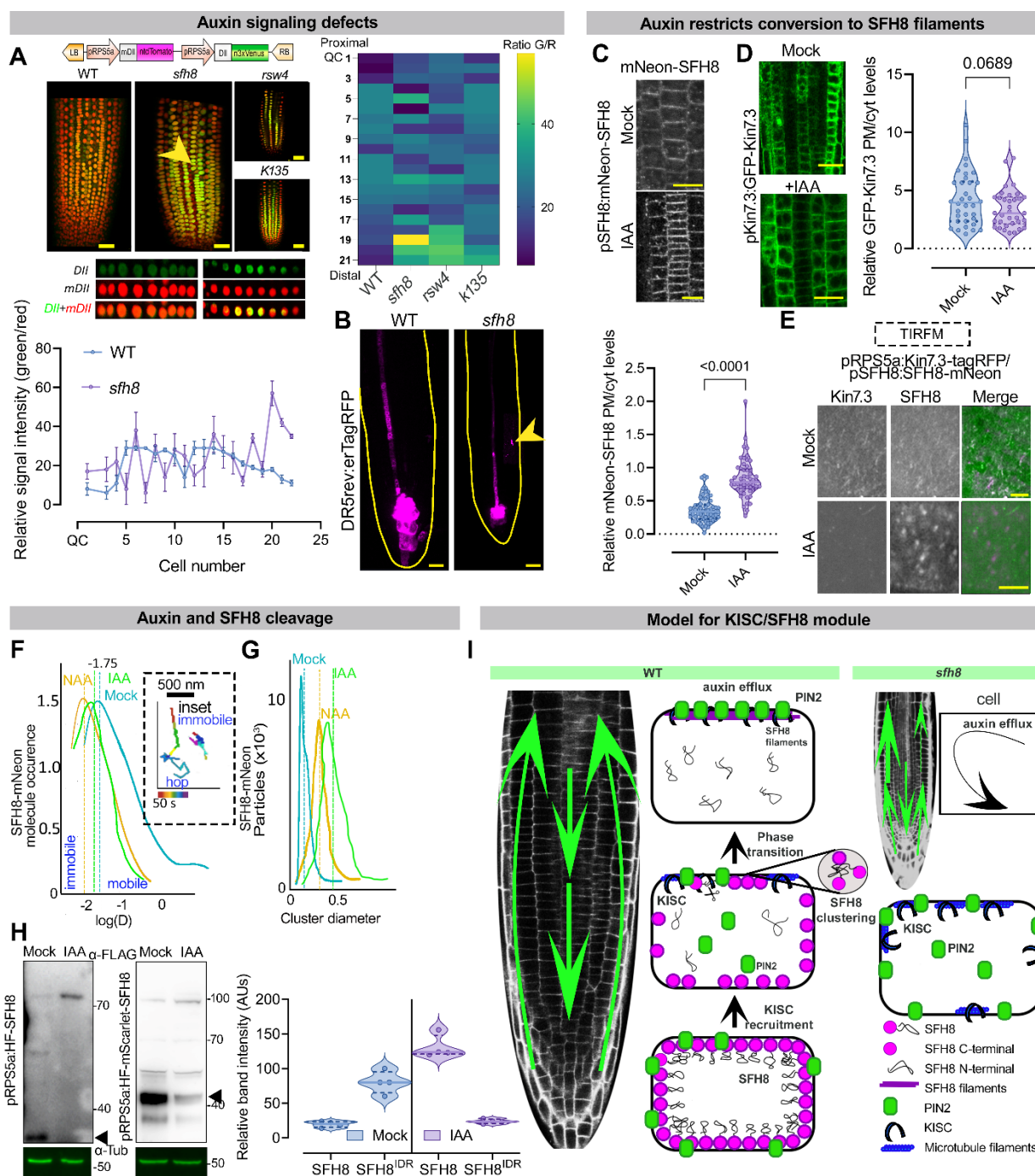
**Figure 7. SFH8/KISC comprises a feedback loop with auxin.**

**A.** R2D2 auxin input sensor (cartoon: transcriptional units *DII-Venus* ("DII") and *mDII-Tm* ("mDII")) in WT, *sfh8*, and KISC mutants. The arrowhead denotes a region with perturbed auxin input. Scale bars, 20 μm. Bottom: "DII" and "mDII" auxin input perturbations in *sfh8* (right). The chart shows DII/mDII ratio quantification (QC to 21st cell towards the shoot; left), and the heat map shows DII/mDII ratio in WT, *sfh8*, *K135*, and *rsw4* (QC(1)-21st cell). Data are mean ± SD from three different roots (n=21 cells per root).

**B.** Auxin output sensor DR5 in WT and *sfh8*. Arrowhead denotes an auxin ectopic maximum in *sfh8*. Yellow outlines denote the roots. Scale bars, 20 μm.

3

1295    **C.** and **D.** mNeon-SFH8 localization ± 100 nM IAA (15 mins, 5 DAG epidermal cells; scale bars,
1296    10 µm); quantification of PM/cytoplasmic signal (bottom)(**C**). GFP-Kin7.3 localisation ± 100 nM
1297    IAA (15 mins); quantification of PM/cytoplasmic signal (right; four pooled independent
1298    experiments; n=64, Kolmogorov-Smirnov)(**D**). Scale bars, 20 µm.
1299    **E.** TIRFM of Kin7.3/SFH8 ±IAA (1.5 h, region 3). Images are representative of an experiment
1300    replicated three times. Scale bars, 0.2 µm.
1301    **F.** and **G**. Diffusion and mobility distribution of SFH8 clusters in the presence or absence of auxin
1302    (NAA or IAA) from TIRFM (time interval 100 msec). The percentage of immobile and mobile
1303    molecules in each graph represents clusters with a trajectory below and above the log(D) of -
1304    1.75, respectively (D, diffusion coefficient). Smaller inset graph: individual trajectories of mobile
1305    clusters in ± auxin (left and right, respectively; 500 frames, n=120). Quantification of SFH8 cluster
1306    size (±100 nM NAA/IAA 5 min, n=120) (**G**).
1307    **H.** Reduction of FLAG-SFH8 or HF-mScarlet-SFH8 cleavage by IAA (1.5 h). Arrowheads denote
1308    cleaved SFH8$^{IDR}$ (HF-IDR or HF-mScarlet-IDR). WBs were replicated three times. Right:
1309    quantification of SFH8/SFH8$^{IDR}$ bands (HF-mScarlet-SFH8 experiments; n=4, 2-tailed t-test
1310    showed difference at $p<0.05$ between SFH8/SFH8$^{IDR}$)
1311    **I.** Model for SFH8 function and IDR-dependent fusion blockage by SFH8$^{IDR}$.
1312

4

**A** Definition of polar domains

**B** Polar localization of KISC

**C**

**D**

**E**

**F** Functionality of Kin7.3 fusions

**G** Kin7.3 interaction with SFH8

**H** SFH8 domain architecture & phylogeny

**I** SFH8/Kin7.3 interaction interfaces

**J** SFH8 complementation of sec14-1ts S. cerevisiae

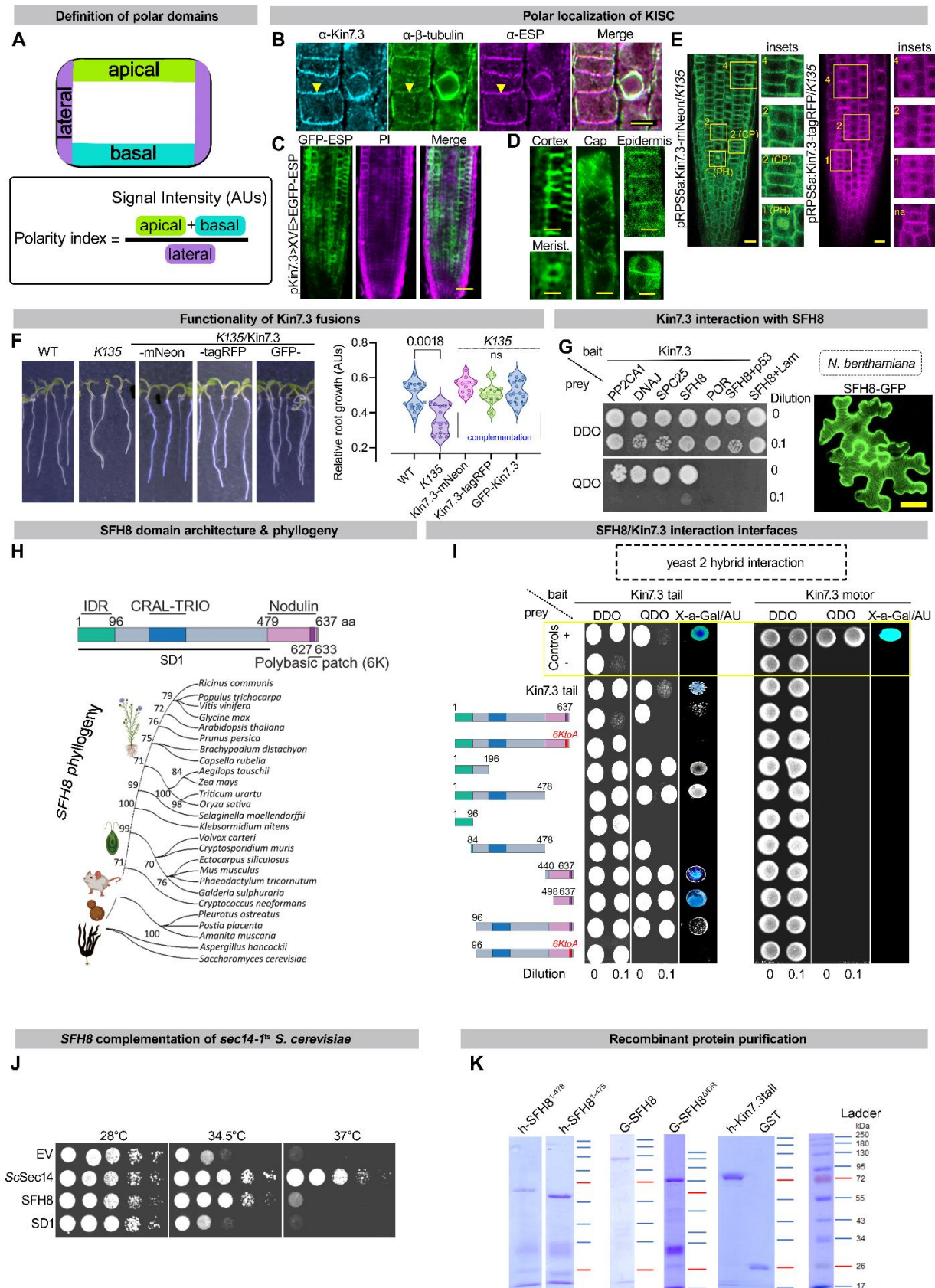**K** Recombinant protein purification

1313

1

**Figure S1. KISC/SFH8 Polarity localization in live-cell imaging.**

**A.** Apical/basal/lateral polarization nomenclature and polarity index determination.

**B.** Representative confocal micrographs of α-ESP/α-Kin7.3 localizations at similar polar domains (counterstained with α-*β*-tubulin; region 4, experiment replicated multiple times). Scale bars, 5 μm.

**C.** Representative confocal micrograph of the ESP estradiol inducible line (20 μM estradiol, 16 h), driven by the Kin7.3 promoter (*pKin7.3>XVE>GFP-ESP*). ESP showed polarization only at the distal meristematic region, while in the proximal meristem region ESP was apolar; Images were obtained in low resolution (512x512 with minimal exposure and no averaging), due to photobleaching and low expression levels of ESP (experiment replicated multiple times with variable expression). Scale bar, 50 μm.

**D.** Digitally zoomed-in enhanced micrographs (deconvoluted) from root tip cells of the *pKin7.3>XVE>GFP-ESP.* Merist., proximal meristematic cell (note the diffused cytoplasmic signal). Cap, lateral root cap. A cell plate decorated by ESP is also shown (bottom right). Note the MT-binding of ESP in the lateral root cap cell at which MTs are highly bundled (as also described in Moschou et al., 2013; 2016). Scale bars, 5 μm.

**E.** Representative confocal micrographs of 5 DAG seedlings expressing *pKin7.3:Kin7.3-mNeon* in the *K135* background at the indicated regions. Right: representative confocal micrographs of epidermal cells of root tip 5 DAG from seedlings expressing pRPS5a:Kin7.3-tagRFP/*K135* (complementation line). CP, cell plate; PH, phragmoplast. Scale bars, 20 μm.

**F.** Complementation of *K135* root phenotype by various Kin7.3 fusions: pKin7.3:GFP-Kin7.3, pRPS5a:Kin7.3-tagRFP, and pRPS5a:Kin7.3-mNeon; quantification of root length (right). Data are means ± SD of five independent experiments each containing five measurements (2-tailed *t*-test).

**G.** Y2H between binding domain (BD)-Kin7.3 and four putative interactors (PP2CA1, DNAJ, SPC25, and PORcino; see also **Supplemental Information** for a description of the Kin7.3 interactors which were not followed herein). AD, activation domain; DDO, double dropout (control); QDO, quadruple dropout (selection). Negative controls: p53 and lamin (Lam). Y2H was replicated four times. Right: representative confocal micrograph (maximum intensity projection) showing p35S:SFH8-GFP localization in *N. benthamiana* leaves. Scale bar, 20 μm. The micrograph is from a single representative experiment replicated multiple times.

**H.** Proposed model of SFH8 architecture (up). Numbers indicate aa truncations used throughout the paper; SD1 corresponds to amino acid residues 1-478. IDR, intrinsically disordered region (1-96 aa; see also **Figure 4D**). The CRAL-TRIO domain binds small lipophilic molecules and is named after the cellular retinaldehyde-binding protein and TRIO guanine exchange factor; phylogenetic analysis of At2G21520 full-length sequence (lower). Numbers indicate bootstrap values with a confidence cutoff of 70 (**STAR METHODS**).

**I.** Y2H between Kin7.3 tail or Kin7.3 motor fused to the binding domain (BD) and different SFH8 truncations fused to the activation domain (AD). DDO, double dropout (growth control); QDO, quadruple dropout (selection medium for interaction). In QDO, the second column (dilution 1:100) corresponds to QDO supplemented with X-a-Gal that is metabolized by yeast cells to produce blue color when interactions between AD-BD fusions are strong (supplemented with aureobasidin, "AU" to further enhance selection). As a positive control, the cohesin loader complex components Mau2/Scc2 were used (Minina et al., 2017) (denoted with the plus symbol). The experiment was replicated four times. The spots from X-a-Gal/AU are from different plates.

**J.** Yeast temperature-sensitive *sec14-1^{ts}* loss-of-function mutant complementation by full-length SFH8 or SD1 (see **H**). Note that at 37°C the complementation was moderate, likely due to the instability of the protein at elevated temperatures (37°C is much beyond the physiological Arabidopsis growth temperature). Dilution series:0-10$^{-4}$. The experiment was replicated three times.

1364    **K.**   Representative denaturing SDS-PAGE gels counterstained with coomassie Brillant blue
1365    (CBB) and fixed showing various proteins used in the assays described in this paper. h, 6xhis-
1366    tag; G, GST tag. The images are representative, while variations in protein integrity were evident
1367    among different purifications for SFH8 (e.g. see **Figure S4**; overall, SFH8 is a very unstable
1368    protein).

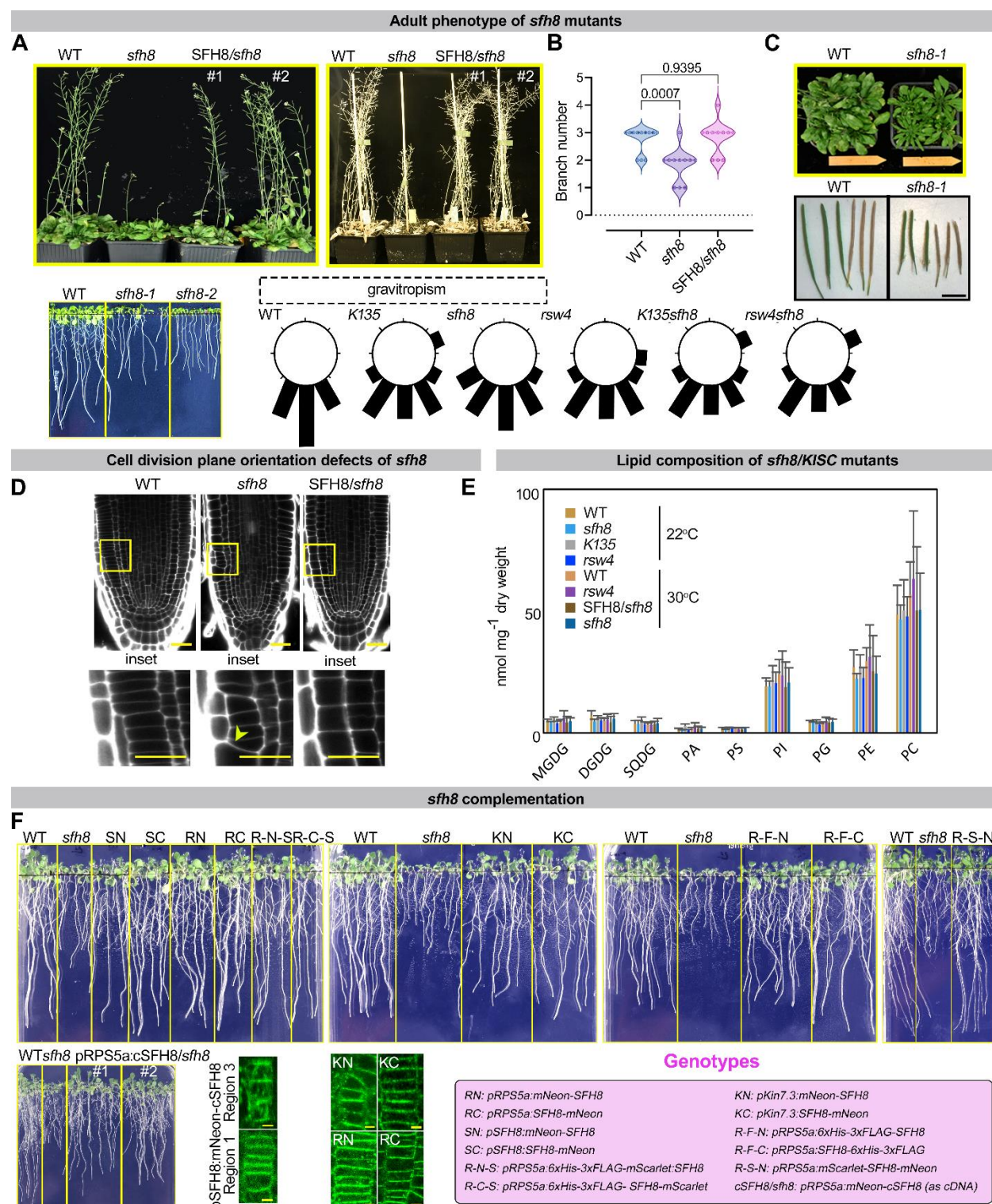**Figure S2. Isolation and characterization of *sfh8* mutants and phenotypic analyses of KISC/*sfh8*.**

**A.** Adult plant phenotype (upper, 21 DAG, 4 plants per pot) and representative photos of WT, *sfh8-1,* and *sfh8-2*, and pSFH8:SFH8-mNeon/*sfh8* lines at 10 DAG (lower left, "SFH8/sfh8"). Note also the reduced expansion of cotyledons (see also **Figure 2**). Hereafter, *sfh8-1* is denoted as

1

1375 "*sfh8*", and due to phenotypical resemblance with *sfh8-2* allele is used throughout the paper.
1376 Bottom: circular plots showing moderate gravity perception defects of KISC, and *sfh8* mutants
1377 grown vertically on plates at 7 DAG. Data are from a single representative experiment replicated
1378 multiple times.
1379 **B.** SFH8 mutation affects auxin-related phenotypes. Quantification of branch number (three
1380 independent experiments; n=12, ordinary 1-way ANOVA).
1381 **C.** Representative images of adult WT and *sfh8* plants in short-day (10h light /14h dark) condition
1382 (upper), and silique lengths (lower). Length bar, 0.8 cm.
1383 **D.** 5 DAG-old meristems from WT, *sfh8,* and SFH8/*sfh8* (sizes were 210±12 for WT, 122±22 for
1384 SFH8, and 213±17 for SFH8/*sfh8*; mean meristem size±SD (n=10; stained with propidium iodide).
1385 Scale bars, 20 µm. The arrowhead in the inset denotes slight cell division plane orientation
1386 perturbations in *sfh8*. In general, 1-3 perturbations per root were observed. Similar phenotypes
1387 were observed for *rsw4* but not *K135* which is a hypomorphic mutant (Moschou et al., 2016). Inset
1388 scale bars, 20 µm.
1389 **E.** LC-MS/MS lipid species quantitative analysis in WT, *sfh8*, *K135,* and SFH8/sfh8
1390 complementation line *(*pSFH8:mNeon-SFH8/sfh8*)* and *rsw4* mutant (treated for 24h at 28°C).
1391 MGDG, monogalactosyldiacylglycerol; DGDG, digalactosyldiacylglycerol; SQDG, sulfoquinovosyl
1392 diacylglycerol; PA, phosphatidic acid; PS, phosphatidyl-serine; PI, phosphatidyl-inositols; PG,
1393 phosphatidylglycerol; PE, phosphatidylethanolamine; PC, phosphatidylcholine. Data are
1394 means±SD of five independent experiments (n=5, significance was tested with various tests; see
1395 also **File S3** for datasets).
1396 **F.** Representative images of seedlings 10 DAG expressing various fusions of SFH8 in the *sfh8*
1397 mutant background. The representative confocal micrographs show localization of mNeon-
1398 cSFH8/*sfh8* ("c" for "complementary DNA"), or KN/KC, RN/RC (5 DAG, region 3 epidermal cells).
1399 Scale bar, 3.5 µm.
1400

**SFH8/KISC form filaments**

**A** — Mock, APM; FM4-64, GFP-Kin7.3, Merge; PCC=0.32±0.14; GFP-Kin7.3, tagRFP-MAP4^MBD, Merge

**B** — *N. benthamiana* localizations; CFP-Kin7.3, mScarlet-SFH8, GFP-ESP, Merge; PM plane

**C** — Mock, APM; Kin7.3, MAP4^MBD, Merge; -APM, +APM, >SFH8-mNeon; α-β-Tub, MAP4^MBD, Merge; Length (μm); p=0.0005; mCherry-MAP4, SFH8-mNeon, GFP-Kin7.3

**D** — Arabidopsis roots; pKin7.3>pXVE>GFP-ESP/pRPS5a:SFH8-mScarlet; Region 4, Region 3, Region 1

**Artificial SFH8 clusters exclude Kin7.3**

**E** — *N. benthamiana* localizations; RFP-SFH8; WT, 2KtoA, 6KtoA; Insets 1, 2, 3; GFP-Kin7.3, RFP-SFH8, Merge; WT, 2KtoA, 6KtoA; insets; details; 1 μm; PM plane

**F** — yeast 2 hybrid interaction; bait/prey; Kin7.3 tail DDO, Kin7.3 tail QDO; SFH8 WT, 2KtoA, 6KtoA; Dilution 0, 0.1

**SFH8 6KtoA variant**

**G** — WT, *sfh8*, pRPS5a:SFH8-mNeon/sfh8; SFH8^6ktoA #1 #2 #3 #4; SFH8 #1 #2

**H** — Relative root growth (AUs); <0.0001; 0.0828; 0.2476; 0.0235; 0.0330; 6ktoA; WT, sfh8, SFH8^6ktoA/sfh8 #1, SFH8^6ktoA/sfh8 #2, SFH8^6ktoA/sfh8 #3, SFH8^6ktoA/sfh8 #4
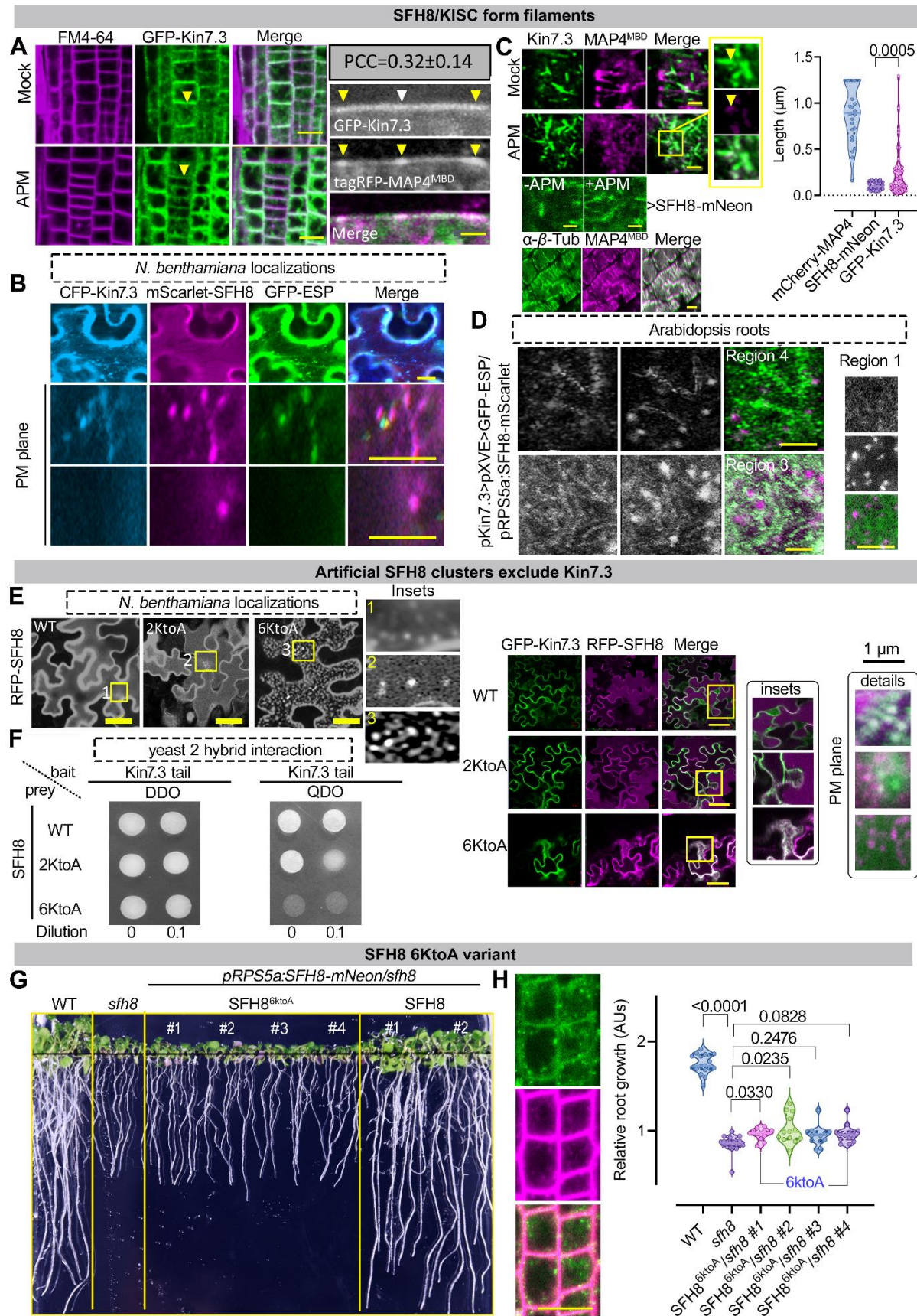
1401

1

**Figure S3. SFH8 clusters exclude the KISC.**

**A.** Kin7.3 partially colocalized with MTs and is excluded from PM MT-bundles. Representative confocal images of pKin7.3:GFP-Kin7.3/p35S:MAP4$^{MBD}$ expressing lines (5 DAG, region 3 epidermal cells) counter-stained with FM4-64, ±APM (10 nM, 1 h; left). Scale bars, 12 µm. Right: representative confocal images of GFP-Kin7.3 at cell contours (5 DAG, region 3 epidermal cells), and cell contour localization of pKin7.3:GFP-Kin7.3/p35S:MAP4$^{MBD}$. The grey box at the top right shows the Pearson Correlation Coefficient (PCC) at the indicated with the arrowheads regions, which in the case of MAP4$^{MBD}$ denote PM-attached MT bundles. Scale bar, 1 µm.

**B.** KISC is restricted from SFH8 clusters but colocalizes with SFH8 filaments. Representative confocal micrograph of *N. benthamiana* leaves transiently co-expressing (4 days post-infiltration) p35S:CFP-Kin7.3 (cyan)/p35S:mScarlet-SFH8/p35S:GFP-ESP. The experiment was replicated multiple times. Scale bars, 10 µm.

**C.** KISC filaments do not show significant signal colinearity with MTs. Representative confocal micrograph showing the partial colocalization of GFP-Kin7.3 filaments with MAP4$^{MBD}$ in region 3 (defined in **Figure 1**) ±APM (10 nM, 1 h). Note that Kin7.3 filaments associated with bundled-MT remnants (reminiscent of clusters; insets, APM treatment). Lower: SFH8 filaments and their resistance upon APM treatment (10 nM, 1 h; region 3); colocalization between MAP4$^{MBD}$/α-tubulin signals. Note that MAP4 protein induces significant MT bundling. Scale bars, 0.1 µm (for filaments) or 3.4 µm for colocalization (MAP4/tubulin). Right: quantification of Kin7.3/SFH8 filaments' length at the PM (six pooled independent experiments; n=40, Wilcoxon). Note the high density of SFH8 length counts around the mean, suggesting that SFH8 filaments are mostly short compared to MT filaments (note the MT length distribution) with little variability. Kin7.3 showed more dispersion, as shown by the violin plot (and the micrograph on the left), indicative of Kin7.3 association with MT filaments/bundles, as well. Scale bars, 1 µm.

**D.** ESP is also restricted from SFH8 clusters in Arabidopsis roots. Representative confocal micrographs of the line co-expressing pKin7.3>XVE>GFP-ESP/pRPS5a:mScarlet-SFH8, after estradiol induction (20 µM, 16-24 h; 5 DAG, region 2 epidermal cells, PM surface at the apicobasal junction). Images were obtained at maximum scanning speed (40 frames per second) using the LIGHTNING super-resolution module of the SP8 Leica confocal microscope (63x W with an x/y-axial resolution of 120 nm upon deconvolution). Post-acquisition, images were deconvoluted using the LIGHTNING algorithm and water correction was set in the algorithm as the mounting medium. Similar settings were used in other images as well. Scale bar, 10 µm.

**E.** The nodulin motif modulates SFH8 clustering propensity most likely through the attenuation of repulsion from lysine (K) residues. Upper: representative confocal micrographs showing the propensity to form clusters of N-terminally RFP-tagged SFH8 variants (SFH8$^{6KtoA}$ and SFH8$^{2KtoA}$, under the p35S) in *N. benthamiana* transient expression system. Insets (right) show details of clusters. The experiment was replicated two times. Scale bars, 20 µm. Right: representative confocal micrographs showing colocalization analyses of RFP-SFH8, -SFH8$^{2KtoA}$, and -SFH8$^{6KtoA}$ with GFP-Kin7.3 (p35S:GFP-Kin7.3) in *N. benthamiana* transient expression system (3 days post-infiltration). Note that in cells expressing SFH8$^{6KtoA}$, GFP-Kin7.3 retained a cytoplasmic localization (insets and details on the right), and also the lack of GFP-Kin7.3 colocalization with RFP-SFH8$^{6KtoA}$ clusters. Scale bars, 50 µm. The experiment was replicated 2 times.

**F.** Kin7.3 tail fails to interact efficiently with SFH8$^{6KtoA}$. Y2H between SFH8, SFH8$^{2KtoA}$, or SFH8$^{6KtoA}$ with Kin7.3 tail. Kin7.3 tail was fused to the binding domain (BD) and the SFH8 variants to the activation domain (AD). DDO, double dropout (growth control); QDO, quadruple dropout (selection medium for interaction). Two dilution series are shown (0 and 0.1). The experiment was replicated three times.

**G.** Note the partial complementation of the *sfh8* mutant background by the SFH8$^{6KtoA}$ mutant variant. Images showing partial complementation of *sfh8* by pRPS5a:mNeon-SFH8$^{6KtoA}$ in 4 individually transformed lines (10 DAG). Two complementation lines with SFH8 are also shown.

2

**H.** Representative confocal micrographs showing the reduced levels of SFH8$^{6KtoA}$ and lack of polarity of mNeon-SFH8$^{6KtoA}$ (green; *pRPS5a:mNeon-SFH8$^{6KtoA}$*/*sfh8*; epidermal cells 5 DAG, region 3) counterstained with the dye FM4-64 (magenta; PM and endosomes staining) from line #2 shown in **G**. Scale bar, 25 μm. Right: quantification of root growth from WT, *sfh8*, and four lines (presented in **G**) expressing *pRPS5a:mNeon-SFH8$^{6KtoA}$* in the *sfh8* background (two independent experiments; n=30, ordinary 1-way ANOVA). Note that the cytoplasmic puncta observed correspond to cellular aggregates of SFH8$^{6KtoA}$ as they show different properties and sizes; in many cases, these puncta were found attached on the PM and were not motile (see **Figure S4**).
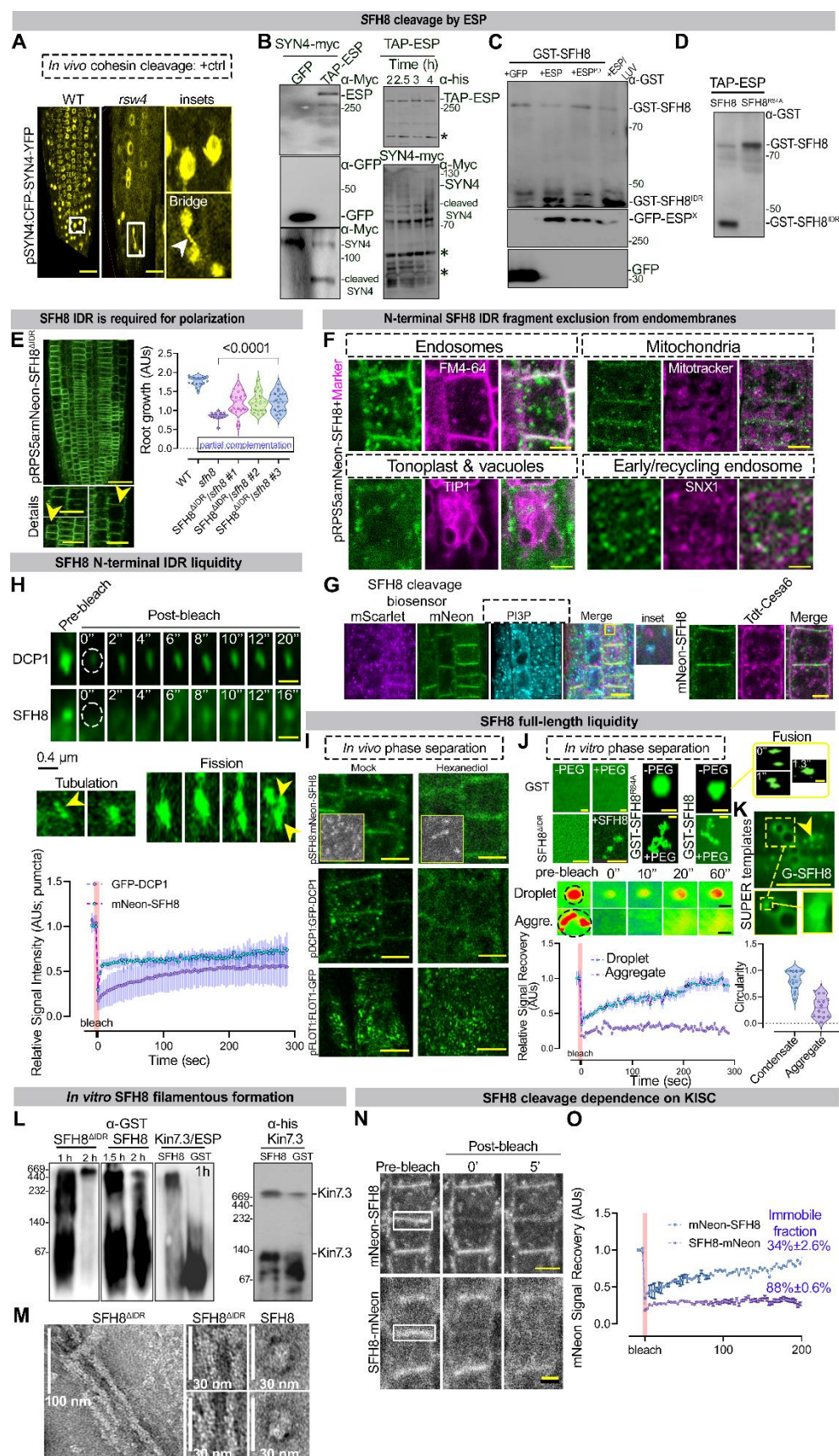
1462 **Figure S4. KISC produces SFH8$^{IDR}$ which does not colocalize with membrane markers, and**
1463 **phase separates.**

1464 **A.** The mitotic cohesin subunit SYN4 is cleaved by ESP *in vivo* in root cells. Representative
1465 images of root cells expressing *pSYN4:CFP-SYN4-YFP* in WT or *rsw4* (at the restrictive
1466 temperature 28°C for 72 h, 5 -7 DAG). Insets show chromosomal bridges in *rsw4* due to the
1467 presumptive lack of the mitotic SYN4 kleisin subunit cleavage by ESP (epidermal cells); the white
1468 arrowhead denotes a chromosomal bridge. The experiment was replicated multiple times (with 1-
1469 3 bridges evident per root). Scale bars, 40 µm. Under our experimental settings, CFP did not yield
1470 a robust signal.

1471 **B.** SYN4 is cleaved by ESP *in vitro* confirming that purified ESP is active. Right: *in vitro* cleavage
1472 of SYN4 on beads (p35S:SYN4-myc) purified from *N. benthamiana*, in the presence of
1473 immunopurified from *N. benthamiana* aTAP-ESP immobilized on beads (aTAP carries c-myc and
1474 hexahistidine tags), mitotically pre-activated by cyclinD (see main text and **STAR METHODS** for
1475 details on purification). Incubation of the cleavage assay was done for 1 h at 37°C. The experiment
1476 was replicated three times. Right: increasing incubation time (2-4 h) led to the formation of
1477 additional cleavage fragments and smearing of SYN4-myc, suggesting that ESP may cleave
1478 SYN4 at multiple sites with differential preference. Asterisks indicate non-specific bands. The
1479 experiments were replicated twice.

1480 **C.** Proteolytically inactive ESP fails to cleave SFH8, and cleavage is supported in the presence
1481 of membranes. *In vitro* GST-SFH8 cleavage by immunopurified from *N. benthamiana* GFP-tagged
1482 variants of ESP, ESP$^{PD}$ (protease dead (Liu and Moschou, 2018), and ESP in the presence of
1483 large unilamellar vesicles (LUVs; made from PC and containing 10 mol %PC and PS; see **STAR**
1484 **METHODS**). The cleaved GST-SFH8$^{IDR}$ is shown (band below 50 kDa). The beads carrying GFP
1485 or GFP-tagged ESP variants in the ±LUVs were co-incubated with GST-SFH8 at 37°C for 1 h. As
1486 the SFH8$^{\Delta IDR}$ was converted to filaments (see below) and due to the observed compromised full-
1487 length SFH8 transfer from the SDS-PAGE to the membrane, the immunoreactive signal increment
1488 of the SFH8$^{\Delta IDR}$/SFH8 (α-GST) ratio upon cleavage was not proportional to the SFH8$^{IDR}$
1489 production. The experiment was replicated four times. Note that the band around 50 kDa was
1490 detected in all samples and thus could correspond to a non-specific cleavage product in the GFP-
1491 trap setting.

1492 **D.** Confirmation of ESP cleavage site on SFH8. GST-SFH8$^{R84A}$ is not cleaved by aTAP-ESP
1493 (similar experimental setting as in **B**). An additional product is due to non-specific cleavage during
1494 purification (above the specific cleavage product around 50kDa). The experiment was replicated
1495 three times.

1496 **E.** The IDR region of SFH8 is biologically important. Representative confocal micrographs from
1497 meristematic epidermal root cells expressing pRPS5a:mNeon-SFH8$^{\Delta IDR}$ in the *sfh8* mutant
1498 background, showing details of localization with lack of filaments, polarization, and cytoplasmic
1499 puncta formation. Note also the reduced robustness of PM localization, uneven SFH8 levels, and
1500 perturbations of growth realized as reduced growth anisotropy (details; middle right cell denoted
1501 by arrowhead). The Scale bar on the top, 40 µm and all others, 20 µm. Right: quantification of
1502 root length of three lines expressing *pRPS5a:mNeon-SFH8$^{\Delta IDR}$* in the *sfh8* background (two
1503 independent pooled experiments; n=18; ordinary 1-way ANOVA).

1504 **F.** SFH8 likely does not colocalize with diffraction non-limited endomembranes and vesicles.
1505 Representative confocal micrographs from *pRPS5a:mNeon-SFH8* expressing lines
1506 counterstained with FM4-64 (endosomes and plasma membrane) or mitotracker (mitochondria)
1507 dyes; lines co-expressing pRPS5a:mNeon-SFH8 with p35S:TIP-RFP (tonoplast intrinsic protein),
1508 or p35S:SNX1-RFP (sorting nexin 1; *trans*-Golgi network). In some cases, the duration of tracking
1509 was limited to the amount of time that particles remained in a single focal plane, as the required
1510 acquisition rate did not permit the collection of z-stacks (voxels); the median track length was 35

1511 frames, corresponding to 20'' of imaging. PCC analyses failed to show colocalization of SFH8
1512 cytoplasmic puncta with any of the markers/dyes used (negative values). Scale bars, 2 µm.
1513 **G.** SFH8 although it can bind to PtdIns(3)P (see also **Figure 1E**) it does not colocalize with
1514 relevant PtdIns(3)P-positive structures *in vivo*. Representative confocal micrograph of lines co-
1515 expressing mScarlet-SFH8-mNeon (green; pRPS5a:6xhis-3xFLAG(HF)-mScarlet-SFH8-mNeon;
1516 see also **Figure 4C**) with PtdIns(3)P (tagged with CFP and expressed under pUBI10). The inset
1517 on the right is digital magnification, showing a lack of colocalization between PtdIns(3)P and
1518 mScarlet-SFH8$^{IDR}$. Right: mNeon-SFH8 does not associate with cellulose synthase complex-
1519 puncta. Representative confocal micrograph of lines coexpressing pRPS5a:mNeon-SFH8 with
1520 Tdt-CESA6 (CELLULOSE SYNTHASE 6 isomer under the p35S). Note the lack of colocalization
1521 between the two proteins. Scale bar, 4 µm. The experiments were replicated three times for
1522 various developmental stages (2-7 DAG), and root tissues (regions 1-4).
1523 **H.** SFH8 cytoplasmic puncta show features of LLPS proteins. Upper: representative confocal
1524 micrographs showing the FRAP signal recovery (normalized integrated density) as a fraction of
1525 time in lines expressing p35S:GFP-DCP1 or pSFH8:mNeon-SFH8. The regions of interest were
1526 set on mobile cytoplasmic puncta (at the midsection of the cell; 7 DAG, region 3-4). Note that the
1527 duration of tracking was limited to the amount of time that the observed particles remained in a
1528 single focal plane, as the required acquisition rate did not permit the collection of z-stacks (voxels).
1529 Middle: confocal time-lapse imaging (2 sec time interval) showing that mobile puncta can freely
1530 flow and deform around surfaces of other structures, as well as undergo tubulation, fusion, or
1531 fission. Arrowheads denote the coalescing puncta. Lower: FRAP signal recovery (normalized
1532 integrated density) as a fraction of time. The red faded band parallel to the Y-axis indicates laser
1533 iterations time. Data are means ± SD of three independent experiments with one replicate each
1534 (n=3). Scale bars, 0.4 µm.
1535 **I.** SFH8 puncta and clusters show features of LLPS proteins. Micrographs from 10% (v/v) 1 h
1536 1,6-hexanediol treatment of pDCP1:DCP1-GFP, pSFH8:mNeon-SFH8 or pFLOT1:FLOT1:GFP
1537 expressing lines (5 DAG cell surface and midsections, epidermal root cells regions 2-3). Note that
1538 in the case of DCP1 and SFH8 cytoplasmic puncta were converted to a diffused cytoplasmic
1539 signal. DCP1 decorates the LLPS compartment known as processing bodies and was used as a
1540 positive control for 1,6-hexanediol efficiency under our conditions. FLOT1 decorates
1541 microdomains at the PM (Jarsch et al., 2014). The insets are from the PM surface (TIRFM),
1542 showing that 1,6-hexanediol dissolved most of the SFH8 clusters. Scale bars, 5 µm.
1543 **J.** *In vitro* LLPS assays for SFH8 variants. Representative confocal micrographs of *in vitro*
1544 recombinant GST, GST-SFH8, GST-SFH8$^{ΔIDR}$, GST-SFH8$^{R84A}$ proteins stained with Alexa638 in
1545 the presence or absence of the PEG3000 crowding agent in LLPS conditions visualized in fluidic
1546 chambers (see **STAR METHODS**). Note that in the presence of PEG, SFH8 and SFH8$^{R84A}$ switch
1547 to agglomerate-like states, while GST-SFH8$^{ΔIDR}$ induced filamentous transition to GST-SFH8.
1548 Scale bars, 0.2 µm. Images are from a single representative experiment replicated three times.
1549 Bottom: representative confocal high-speed micrographs showing droplet and aggregate signal
1550 recovery, and quantification of FRAP signal recovery (normalized integrated density) as a fraction
1551 of time of GST-SFH8$^{R84A}$ droplets and aggregates. Scale bars, 0.2 µm. The red faded band
1552 parallel to the Y-axis indicates laser iterations time. Data are mean ± SD of five or more
1553 independent experiments with one replicate each (n=5-8). Right: GST-SFH8 $^{R84A}$ droplet fusion in
1554 the same experiment.
1555 **K.** SFH8 can phase separate on model membranes. Representative high-speed super-resolution
1556 (120 nm) images from a SUPER template experiment showing that GST-SFH8 labeled with
1557 Alexa638 (0.1 µM of GST-SFH8 in the assay) can form liquid-like droplets on membranes.
1558 Furthermore, GST-SFH8 showed an increased propensity to undergo LLPS in the presence of
1559 SUPER templates (see arrowhead denoting droplet; some droplets were released in the bulk
1560 phase as they do not attach on SUPER templates). Scale bar, 0.8 µm. Images are from a single
1561 representative experiment replicated three times.

3

1562  **L.** SFH8 conversion to high molecular weight assemblies. Native gel electrophoresis of SFH8$^{\Delta IDR}$
1563  and full-length SFH8. Western blots with α-SFH8 showed the rapid conversion of recombinant
1564  GST-SFH8$^{\Delta IDR}$ to agglomerates (1-2 h); very few agglomeration propensities were detected for
1565  GST-SFH8. Note that in the presence of Kin7.3/ESP GST-SFH8 converted faster to high-
1566  molecular-weight assemblies (1 h). Right: detection of 6xhis-GFP-Kin7.3 using α-his, showing
1567  that in the presence of SFH8, Kin7.3 also formed agglomerates (not that evident in GST samples).
1568  Western blots are from a single representative experiment replicated twice.
1569  **M.** Nanoscale observation of filaments and clusters of SFH8. Negative staining-TEM of GST-
1570  SFH8$^{\Delta IDR}$ filaments and GST-SFH8. Note that in this setting filaments/clusters varied in size
1571  between several nm to 0.5 µm. Scale bars are indicated on the images. Images are from a single
1572  representative experiment replicated twice.
1573  **N.** The C-terminally tagged SFH8 shows a different diffusion rate than the N-terminally tagged
1574  (see also relevant figure **Figure 3G**). Representative confocal micrograph showing FRAP signal
1575  recovery (normalized integrated density) as a fraction of time of the N or C-terminally tagged
1576  SFH8 with mNeon on the PM (under the pSFH8), implying increased diffusion (due to cleavage,
1577  liquidity, and dwelling time of clusters; note also that the curve in **O** of mNeon-SFH8 did not follow
1578  single exponential curve suggesting more complex diffusion dynamics). The white rectangular
1579  denotes the region of interest that was bleached. Scale bars, 5 µm.
1580  **O.** The N-terminally tagged SFH8 diffuses from the PM. Quantification of FRAP signal recovery
1581  as a fraction of time from cells expressing pSFH8:mNeon-SFH8 or pSFH8:SFH8-mNeon lines (in
1582  *sfh8* background) on the PM (5-7 DAG, epidermal cells of region 3; upper graph), Percentages
1583  indicate immobile fractions for N- and C-terminally tagged SFH8 with mNeon or N-tagged SFH8.
1584  The red faded band parallel to the Y-axis indicates laser iterations time. Data are means ± SD of
1585  three independent experiments with one replicate each (n=3). Asterisks indicate statistical
1586  significance at $p < 0.0001$ (Wilcoxon).
1587

**Fusion defects in KISC/*sfh8* mutants**

A — Apical/basal, Magnified (WT, *sfh8*, *K135rsw4*); CW labels

B — Plasma membrane / Cell plate; Unfused vesicles/10 μm; <0.0001, <0.0001, 0.0022; WT, *sfh8*, K135rsw4

**In vivo dynamics of PIN2 with CHX**

C — AHA1 signal recovery (AUs); AHA1, CHX; AHA1 (-CHX); nd; WT, *sfh8*; bleach

D — PIN2 signal recovery (AUs); PIN2, CHX; WT, *sfh8*; bleach; Time (sec); pPIN2:PIN2-GFP (WT, *sfh8*, *K135*)

**Localization of PINs and apolar proteins in *sfh8/KISC* mutants**

E — WT, *sfh8*, *K135rsw4*; PIN1, PIN3, PIN4, PIN7

F — PIN1 detail; WT; endosomes (*sfh8*); p35S:GFP-AHA1 (WT, *sfh8*); p35S:PIP2a-GFP (WT, *sfh8*)

**SFH8 lack of interaction and colocalization with clathrin**

G — CLC2-GFP, TAP-GFP; *sfh8*, WT; h-SFH8, h-SFH8ΔIDR, Control; α-GFP; TAP-GFP, GFP-CLC2; α-SFH8; *(IgG); supernatants, inputs; α-SFH8; SFH8, SFH8ΔIDR

pRPS5a:HF-mScarlet-SFH8/ pCLC2:GFP-CLC2; GFP-CLC2; mScarlet-SFH8; Merge

**Endocytosis in not significantly affected in KISC/*sfh8* mutants**

H — mNeon-SFH8, TAMRA-PEP1, Merge; pSFH8:mNeon-SFH8; Relative TAMRA-PEP1 PM/cyt signal (AUs); 0.9814, 0.9976; PEP1 uptake; WT, *sfh8*, K135

Relative FM4-64 PM/cyt signal (AUs); FM464 uptake rate; WT, *sfh8*, *K135*, *rsw4*; Time (min)
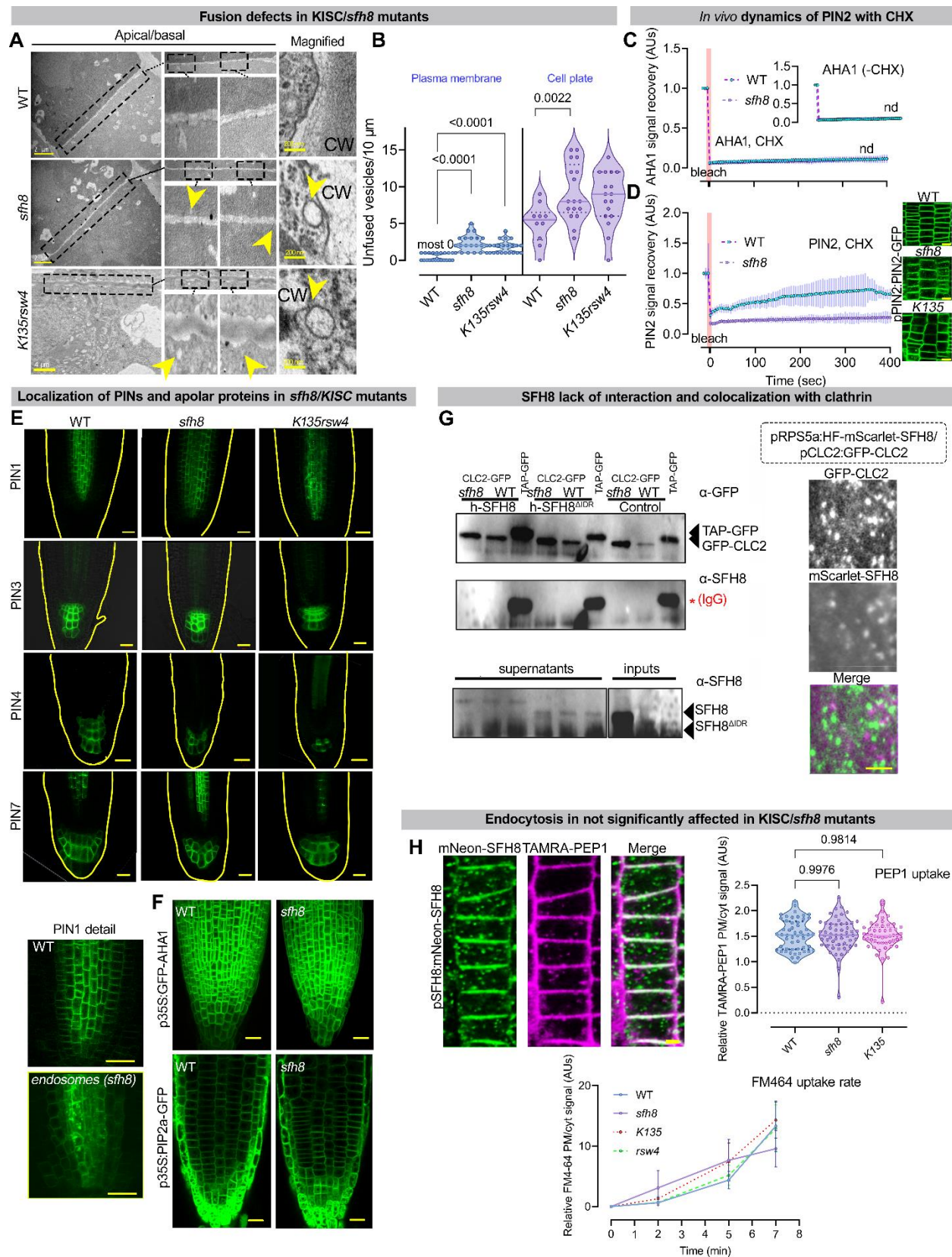
1588

5

**Figure S5. *SFH8* effects on fusion and endocytosis.**

**A.** SFH8-dependent fusion at the PM at a nanoscale resolution using TEM. TEM micrographs focusing on the PM (region 3) showing proper tethering but reduced vesicle fusion in *sfh8,* and the KISC mutant *K135rsw4* (24 h at the restrictive temperature 28°C; this double mutant phenocopies *rsw4* as shown in Moschou et al., 2016). Arrowheads denote vesicles that did not fuse with the PM and may imply that SFH8/KISC regulates fusion. CW, cell wall. Scale bars, as indicated on the images. Images are from a single representative experiment replicated two times (n=50, with various magnifications). Note that image inspection did not reveal perturbations in the ultrastructure of organelles in the mutants. We cannot rule out though subtle differences at the ultrastructure.

**B.** Quantification of fusion events from TEM images at the PM and the cell plate in WT, *sfh8*, and *K135rsw4* (four independent pooled experiments; n=19 counts in each experiment, Wilcoxon).

**C.** and **D**. SFH8 does not seem to be a general regulator of the secretory pathway; the non-polar AHA1 and the polar PIN2 recovery rate at the PM are not affected by *de novo* protein synthesis. Quantification of FRAP signal recovery (normalized integrated density) as a fraction of time from p35S:GFP-AHA1 (upper; inset graph without CHX) or pPIN2:GFP-PIN2 (lower) expressing lines. In the lower quantification, GFP-PIN2 retention in *sfh8* and *K135* endosomes is shown (30 min CHX treatment, right). Note that CHX did not lead to the dissolution of PIN2 endosomes. The red faded band parallel to the Y-axis indicates laser iterations time (five or more independent experiments with one replicate each; n=5-8). Images (right **D**) are representative of an experiment replicated two times.

**E.** SFH8 is affecting a subset of polarly localized PIN proteins and likely is not a general regulator of exocytosis or secretion. Representative confocal micrographs showing PIN1, PIN3, PIN4, and PIN7 delivery at polar domains in WT, *sfh8*, and *rsw4* (left) expressing pPIN1:PIN1-GFP, pPIN3:PIN3-GFP, pPIN4:PIN4-GFP, and pPIN7:PIN7-GFP, 5 DAG. PIN1 levels were also reduced in the mutants, while endosomes could also be observed. Note that slight level perturbations were also observed for PIN3, 4, and 7 in the *sfh8* and *K135rsw4* (24 h at the restrictive temperature 28°C; 5 DAG), but due to somewhat different patterning of the columella cells in these mutants these are hard to follow-up (see also discussion on patterning in Moschou et al., 2013). On the other hand, no endosomes were observed for these proteins in the mutant backgrounds. Bottom: localization details for PIN1; note that in some cases PIN1-GFP showed endosomes accumulating in the *sfh8* (mostly) and *K135rsw4*, suggesting that PIN1 delivery was also compromised albeit to a lesser extent (as also discussed in Moschou et al., 2013 for the *rsw4* mutant). Scale bars, 20 μm. Images are representative of an experiment replicated multiple times.

**F.** Representative confocal micrographs of AHA1-GFP in WT and *sfh8* on the PM of epidermal root rip cells (5 DAG, region 3) expressing p35S:GFP-AHA1, or p35S:PIP2a-GFP. Scale bars, 20 μm. Images are representative of an experiment replicated multiple times.

**G.** Western blots showing lack of binding between immunopurified clathrin complexes containing CLC2-GFP from lines expressing pCLC2:CLC2-GFP (seedlings of 7 DAG), with recombinant GST-SFH8 or GST-SFH8$^{\Delta IDR}$. As a control, a TAP-tagged GFP was used (producing a signal also due to secondaries that could efficiently bind the immunoglobulin of the TAP-tag; *IgG). Western blots are representative of an experiment replicated three times. Right: representative dual-channel TIRFM micrographs showing the lack of colocalization between mScarlet-SFH8 (magenta) and CLC2-GFP (green; mock) from pSFH8:SFH8-mNeon/pCLC2:CLC2-GFP expressing lines. Scale bar, 0.2 μm. Images are representative of an experiment replicated multiple times, irrespective of the root region examined.

**H.** Lack of colocalization between SFH8-mNeon and TAMRA-PEP1 (left; stains TGN and PM clusters), and quantification of the rate graphs showing TAMRA-PEP1 and FM4-64 uptake in WT, *sfh8*, and *K135* (violin plot and rate plot, respectively; three independent experiments; n=9, Wilcoxon-other tests produced similar results; experimental setting in **STAR METHODS**). Scale bars, 2 μm.
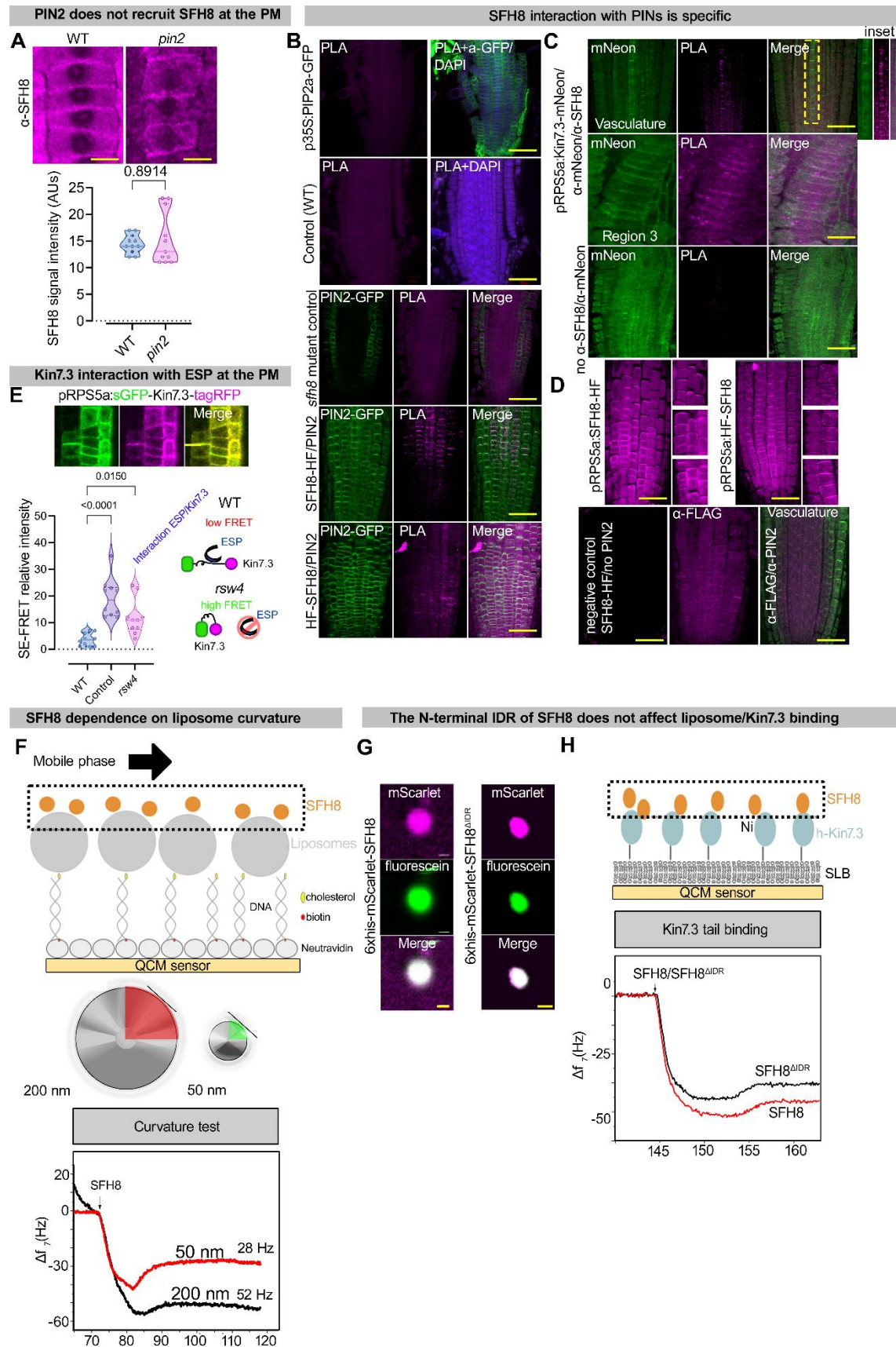
**A** — PIN2 does not recruit SFH8 at the PM

**B, C, D** — SFH8 interaction with PINs is specific

**E** — Kin7.3 interaction with ESP at the PM

**F** — SFH8 dependence on liposome curvature

**G, H** — The N-terminal IDR of SFH8 does not affect liposome/Kin7.3 binding

1640

**Figure S6. SFH8/PIN2 interactions and assays control for PLA; liposome fusion assay controls.**

**A.** PIN2 is not recruiting SFH8 at the PM. Representative confocal micrographs showing α-SFH8 signal in WT, and *pin2* mutant background (5 DAG, region 3 cortex cells), and quantification of α-SFH8 signal intensity in WT, and *pin2* mutant (lower; three independent experiments with signal calculations from cortex cells from regions 3-4 with three roots each; n=9, Wilcoxon). Scale bars, 5 µm.

**B.** Control experiments showing the specificity of the PLA approach (PIN2/SFH8 assay). SFH8 did not interact with PIP2a, while SFH8-HF (α-FLAG) interacted extensively with PIN2 (α-GFP) at region 3 onwards at the PM. Note the significantly reduced PLA-positive signal in HF-SFH8/PIN2 PLA experiment (bottom panel; PLA signal was observed at the cell plate as well). The *sfh8* mutant was used as a negative control for the PLA approach (specificity of α-SFH8 in a PLA setting; sometimes a nuclear non-specific signal was observed in negative controls). Scale bars, 50 µm. Images are representative of experiments replicated five times.

**C.** SFH8/Kin7.3 interact significantly with each other at regions 3-4. PLA of α-mNeon/SFH8 and inset (right) showing the increased interaction strength towards region 4 (for example in the vasculature; upper images). The "no -α-SFH8" corresponds to a negative control (bottom) in which only α-mNeon was used and thus did not produce a positive PLA signal. Scale bars, 50 µm (for "region 3" panel, 10 µm). Images are representative of an experiment replicated five times.

**D.** FLAG epitope stainings confirm SFH8 localizations. α-FLAG signal in HF-SFH8 or SFH8-HF expressing lines in the *sfh8* mutant (5 DAG; **Figure S2F** for complementation). Insets denote the localization at the corresponding region. Images are representative of an experiment replicated twice. Scale bars, 50 µm.

**E.** Kin7.3/ESP likely interact mainly at the PM. SE-FRET experiments at the PM show that N- and C-termini of Kin7.3 fold over in the absence of ESP (*rsw4*; see also Moschou et al., 2016 for a similar situation upon MT binding), suggesting also that ESP/Kin7.3 interact at the PM. Scale bar (micrograph), 5 µm. "control": p35S:sGFP-tagRFP expressing lines (yielding high FRET). Data are means±SD of three independent experiments with three roots each (n=9, Wilcoxon).

**F.** Control experiments show that SFH8/SFH8$^{\Delta IDR}$ do not differ in their affinity for LUVs. As liposome co-flotation assays take significant incubation time and thus can be biased towards the increased molecular weight and sedimentation propensity of SFH8$^{\Delta IDR}$ due to its filamentous conversion and reduced hydrodynamic radius leading to erroneous affinity determination, we designed a semi-quantitative *in vitro* assay based on Quartz Crystal Microbalance with Dissipation monitoring (QCM-D). We used the QCM device as a sensitive mass sensor monitoring the frequency response (Δf) of the acoustic wave during binding events on the surface of a model membrane (Mateos-Gil et al., 2016). The device surface was first covered with neutravidin (layer 1) which was used to bind specifically a 5'-biotinylated DNA (layer 2). This DNA was also modified at the 3'-end with a cholesterol moiety, further employed to anchor a liposome (layer 3). We prepared 50 nm diameter liposomes with two different lipid compositions: DOPC:PI(4,5)P2 (99:1, n/n) and DOPS:PI(4,5)P2 (99:1, n/n). Finally, proteins (e.g. GST-SFH8) were infused (layer 4) on top of layer 3. Bottom graph: SFH8 binding on membranes is independent of curvature in QCM-D setting. The size of liposomes did not significantly affect SFH8 binding, excluding the possibility that SFH8 required curvature (convex or concave) or flat surfaces for binding. Binding of SFH8 on 50/200 nm on QCM-D coupled liposomes with PS:PI(4,5)P$_2$ (99:1). Note that the small difference in Δf observed could be due to the larger surface of 200 nm liposomes, incorporating more protein. The schematic diagram shows the differences in curvature between liposomes with a diameter of 200 and 50 nm. Note the increased surface accessible to the tangent, which represents the interface between liposomes and proteins. Data are representative of an experiment replicated two times.

**G.** Confirmation of results in **F** using imaging. Representative confocal images showing that the hexahistidine tagged recombinant mScarlet-SFH8/mScarlet-SFH8$^{\Delta IDR}$ (proteins purified from *E.*

8

1692     *coli*) showed binding in the solution of PC:PI(4,5)P$_2$ containing SUV liposomes (99:1; liposomes
1693     stained with fluorescein in their lumen) under the fusion assay conditions. Scale bars, 400 nm.
1694     Images are representative of an experiment replicated two times.
1695     **H.** Determination of Kin7.3 binding on GST-SFH8 and GST-SFH8$^{\Delta IDR}$. Again, due to the
1696     filamentous conversion of GST-SFH8$^{\Delta IDR}$ as described above (see **F**), we designed a real-time
1697     binding assay with a supported lipid bilayer approach for Kin7.3 tail affinity determination: GST-
1698     SFH8 and GST-SFH8$^{\Delta IDR}$ protein binding on QCM-D coupled liposomes. Lower: real-time curves
1699     showing dynamic binding through the frequency response of QCM-D obtained upon infusion of
1700     full-length SFH8 (upper panel) or GST-SFH8$^{\Delta IDR}$ (bottom panel) proteins on supported lipid
1701     bilayers carrying hexahistidine-tagged Kin7.3 tail immobilized on the supported lipid bilayer via
1702     DGS-NTA(Ni) lipid anchor. Only slight, insignificant differences were observed in the binding
1703     between the two protein variants. As of note, SFH8/SFH8$^{\Delta IDR}$ differ in molecular mass and thus
1704     SFH8 should give a slightly higher response in Δf as shown. Data are representative of an
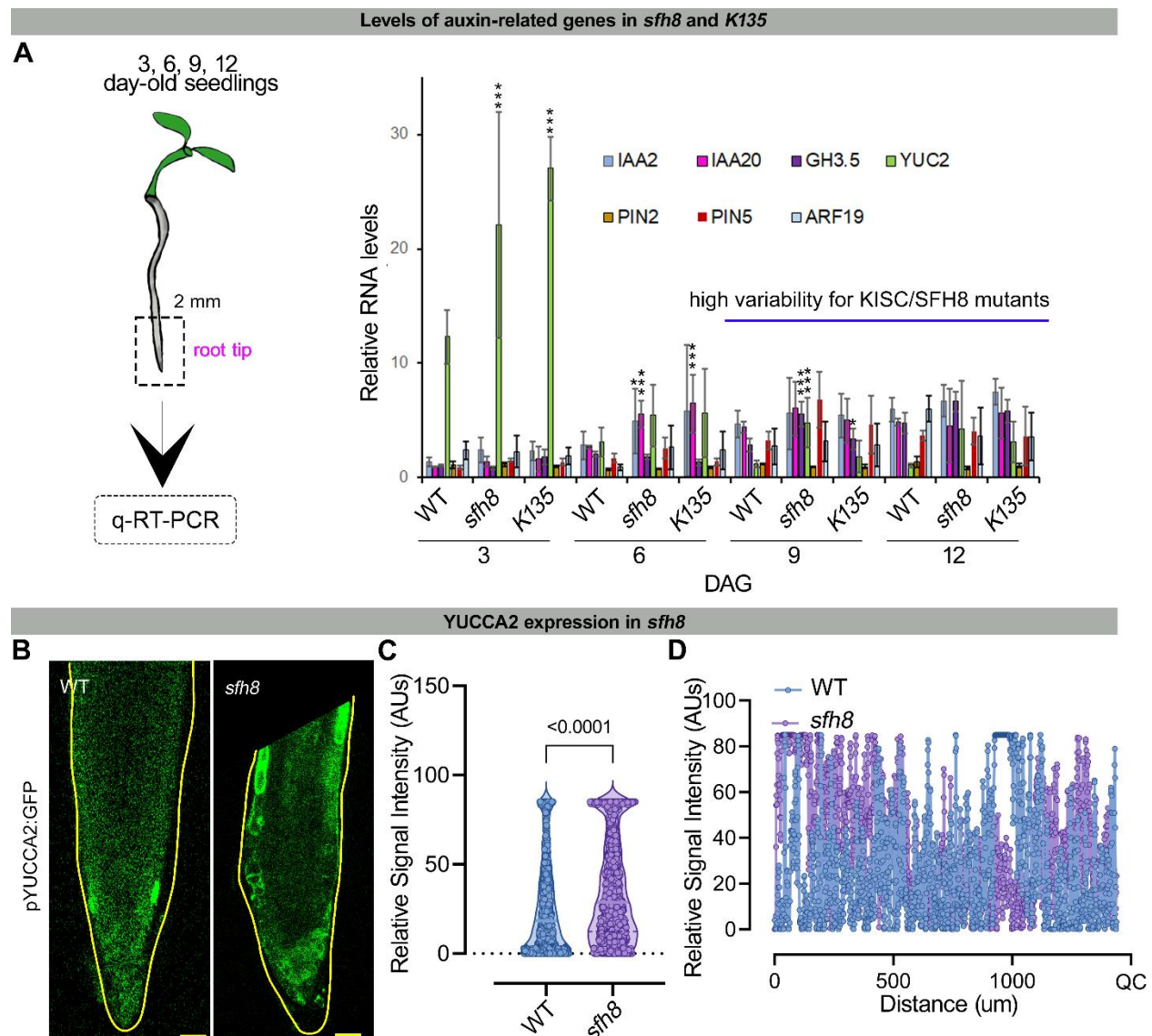1705     experiment replicated twice.
1706

**Figure S7. *SFH8* affects auxin signaling robustness.**
**A.** Real time-quantitative-PCR (q-RT-PCR) setting for evaluation of changes in auxin-signaling genes (left). Two-millimeter root meristems were cut and processed for RNA extraction. Right: relative expression of the indicated genes normalized against *Actin-7 and PP2A* (mean±SD from three independent experiments with two technical replicates; 2-tailed *t*-test to test robustness). Note the high variability of gene expression in the mutants (expanded SD). Asterisks: significance at p<0.05 (*) or p<0.0001 (***); *t*-test.
**B.** Confirmation of reduced robustness of expression in *sfh8* of the auxin biosynthetic gene *yucca 2*. Representative confocal micrographs showing pYUCCA2:GFP expression (5 DAG root meristem cells). Images are representative of experiments replicated five times. Scale bars, 20 µm.
**C.** Quantification of pYUCCA2-GFP signal distribution (signal integrated density), in WT and *sfh8* (three independent experiments with three roots each; n=1,492 points across the root; 2-tailed *t*-test).
**D.** Plot profile showing relative signal intensity along the root in WT and *sfh8*. QC, quiescent center (single representative experiment, replicated three times). Note the aberrant intensity peaks of pYUCCA2-GFP in *sfh8*.

10

**Supplemental Information**

***Localization of Kin7.3 interacting proteins in stable or transient expression***
We expressed PP2C, Spc25, and POR in stable Arabidopsis Col-0 lines or *N. benthamiana*. The localization of these proteins is shown (**Figure 1**). Furthermore, we identified homozygous mutants of these proteins, showing a lethal phenotype for Spc25 and POR mutants confirming previous data (Shin et al., 2018; Steinborn et al., 2002).

The phosphatase PP2C (AP2C1), an *Arabidopsis* Ser/Thr phosphatase of type 2C, is a stress signal regulator that inactivates the stress-responsive MAPKs MPK4 and MPK6 (Bequette et al., 2018; Schweighofer et al., 2007). Mutant *ap2c1* plants produce significantly higher amounts of jasmonate upon wounding and are more resistant to phytophagous mites (*Tetranychus urticae*). Plants with increased AP2C1 levels display lower wound activation of MAPKs, reduced ethylene production, and compromised innate immunity against the necrotrophic pathogen *Botrytis cinerea*. Phosphorylation by a MAPK module regulates Kin7 superfamily members Hinkel and Tetraspore, which impinge on cell plate formation (Takahashi et al., 2010).

The Spc25 is part of the centromere assembly complex. Kin7.3 is a centromeric protein-E homolog and thus this interaction as well might be biologically relevant especially during cell division. Spc25, is a component of the NDC80 complex, in mouse oocytes, an outer kinetochore complex comprising four subunits (ndc80/Hec1, nuf2, spc24, and spc25)(Xiong, 2011). The NDC80 constitutes one of the core MT-binding sites within the kinetochore. One hypothesis would be that KISC during cell division is involved in MT stabilization on the centromeres. Among the components of the outer kinetochore complex, the four proteins in the NDC80 complex, including NDC80 [nuclear division cycle 80, also known as Hec1 (highly expressed in cancer1) in humans], NUF2 (nuclear filament-containing protein 2), SPC24 (spindle pole body component 24) and SPC25, play critical roles in connecting spindle fibers to chromosomes. In vertebrates, the C-terminal ends of the NUF2-NDC80 heterodimer associate with the N-terminal coiled-coil domains of the SPC24-SPC25 heterodimer (Suzuki et al., 2016). Globular dimeric heads, containing the RWD (RING finger, WD repeat, DEAD-like helicases) domain of the SPC24-SPC25 dimer, bind to the inner kinetochore components, the KNL1-Mis12 complex. Therefore, the NDC80 complex serves as a central 'hub' connecting the kinetochore complexes, which provides the 'bridges' between the inner kinetochore complexes and the MTs of the spindle.

The PORCINO protein is a tubulin folding cofactor and its absence results in embryo lethality (Steinborn et al., 2002). The importance of Kin7.3 interaction with PORCINO (POR) remains to be established. The TFC C ortholog, PORCINO belongs to the four *PILZ* group genes encoding orthologs of mammalian tubulin-folding cofactors (TFCs) C, D, and E, and associated small G-protein Arl2 that mediate the formation of α/β-tubulin heterodimers *in vitro*. PORCINO was detected in cytosolic protein complexes and did not colocalize with MTs. Consistently, with previous reports, the *por* mutant was embryo lethal and the POR localized in the cytoplasm.
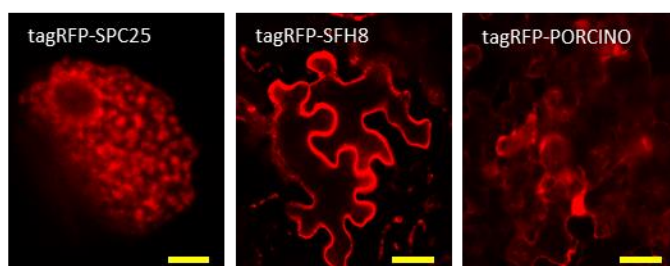


**Figure 1. Localization of Kin7.3 interactors and putative interactions of Kin7.3.**

(A)     Localization of SPC25, SFH8, and PORCINO tagged N-terminally with tagRPF in *N. benthamiana* transient system. Micrographs are representative of an experiment replicated three times results. Scale bars, 20 μm.

### *Cleavage of Cohesin Subunit SYN4 by Separase*

Sister-chromatid cohesion depends on cohesin, a 4-subunit protein complex that links the sisters as they are synthesized in the S phase. In anaphase when the protease separase cleaves the Scc1/ Mcd1 subunit of cohesin (or its Rec8 counterpart in meiotic cells), thereby allowing the sisters to be pulled apart by the mitotic spindle. The *Arabidopsis* genome encodes four kleisin subunits: the meiosis-specific ones SYN1 and SYN3, involved in gene expression of meiotic genes, but also expressed in somatic cells, and SYN2 and SYN4, which have been suggested to participate in mitotic cell division (Minina et al., 2017). As we have shown previously, plants expressing tagged SYN proteins, except the mitotic cohesin SYN4, were highly susceptible to even mild environmental changes and showed decreased fertility (Minina et al., 2017).

### *Principle of R2D2 Probe*

R2D2 shows a diminishing green but not red fluorescence when auxin levels are high, as the conserved domain II (DII) marker (pRPS5A-driven DII fused to n3×Venus) is rapidly degraded in response to auxin. On the contrary, the pRPS5A-driven mutated DII-ntdTomato (red fluorescence) is not responding to auxin, thereby allowing the ratiometric fluorescence quantification of auxin response levels through the R2D2 (Liao et al., 2015).